POLSKA AKADEMIA NAUK

INSTYTUT BUDOWNICTWA WODNEGO

Mgr inż. Duje Veić

EFFECT OF THE BREAKING WAVE SHAPE ON THE TEMPORAL AND SPATIAL PRESSURE DISTRIBUTION AROUND A MONOPILE SUPPORT STRUCTURE

Praca doktorska

Promotor:

Dr hab. inż. Wojciech Sulisz, prof. nadzw. IBW PAN

Gdańsk 2018

Table of contents

List of figures

List of figures

List of figures

List of figures

List of tables

1 Introduction

The prediction of wave loads on maritime structures is of fundamental importance for coastal and offshore engineering. For slender cylindrical structure the breaking wave impact load might be the dominant component of hydrodynamic load. Although many studies have been conducted on the interaction between breaking wave and a vertical cylindrical structure, much uncertainty remains. A better understanding of the phenomena may lead to an improved design methodology and eventually to optimization of numerous coastal and offshore structures.

In general, the prediction of wave loads on maritime structures should include nonlinear wave load component that may exceed many times a corresponding first-order quantity (Sulisz 1993, 2013). For slander vertical cylindrical structures, especially such structures located in relatively shallow waters, wave impact load due to breaking waves constitute the dominant component of a total load and it must be included in a design analysis.

The monopile structures are generally the most cost efficient supporting structures for the offshore wind turbines, considering water depths in the range of 15m to 45m. In recent times one observes an increasing trend to design bigger and heavier wind turbines, even larger than 10MW. The bigger wind turbines require larger monopile support structures. Larger monopile support structures are exposed to significantly higher hydrodynamic loads, as the inertia component of the hydrodynamic force is proportional to the square of the structure diameter. For the new generation of the monopile support structures, the extreme hydrodynamic loads from breaking waves can be critical for the structure and may define a design limit state.

The problem is that the hydrodynamics of the breaking wave interaction with a monopile foundation is a complex 3-D phenomenon characterized by very short duration and extremely high pressures. This complex phenomenon is usually simplified by conservative 2-D approaches. However, in order to increase the knowledge on breaking wave impact, a study on the 3-D pressure distribution during the wave impact is essential.

1.1 Experimental analysis

The extreme wave impact on structures is of interest of many studies, e.g. Sulisz et al. (2005 to 2009). The laboratory studies of interaction between breaking waves and vertical cylindrical structures are very challenging as uncertainties in measurements and interpretation of experimental data are high.

The scatter of the value of measured peak pressure is significant, even when experimental conditions are repeated such as in the study of Chan et al. (1995). The peak pressure generally ranges between 1-50ρc_b^2, where c_b is the wave phase speed. The interaction of breaking waves with a structure is characterized by the presence of dispersed air bubbles and trapped air pockets between the overturning wave jet and the structure. The high variability of the peak pressures for cases with almost identical incident wave conditions is usually associated with a random occurrence of entrapped air bubbles, trapped air pocket, as well as random kinematics of the breaking wave front (Zhou et al., 1991).

One of the reasons for the high scatter in pressure measurements may also be due to measurement techniques. In order to correctly describe the impact pressure rising time and the impact pressure maxima, the pressure sampling rate should be very high. In the study of van Nuffel et al. (2011), the slamming drop test was performed on cylinder hitting the calm water. The measured impact pressures were processed with the different data sampling rates in the range of 25kHz to 1MHz. It was observed that application of the lower sampling rate leads to lover pressure values. By resampling the data measured with 100Mhz to 25kHz, the peak impact pressure reduction was 24%. In the experimental studies of Zhou et al. (1991) and Chan et al. (1995) the pressure sampling rate was 20kHz.

In contrary to the discrepancies in the peak values of the impact pressures, other characteristics of the pressure signal such as the impact pressure time scales, an oscillatory behaviour of pressure signal in decaying phase, as well as a spatial and temporal pressure distribution around the cylindrical structure are similar between conducted experiments. Moreover, the results of the integration of the impact pressure around the structure is far less variable than the highly variable peak pressure. However, the measurements from pressure transducers are usually obtained only every 10-15 degree around the cylinder span (Hildebrandt & Schlurmann, 2012), which is not sufficient to correctly derive the total impact force and conduct a detailed analysis of the breaking wave impact on a cylindrical structure.

In order to measure the total hydrodynamic force on the structure, the system of force transducers is usually installed at the top and the bottom of the cylinder. The hydrodynamic force is measured by strain gauges mounted on a spring of known elasticity (force transducers). Therefore, the measured data provide information of the structural response not actual hydrodynamic force. If the response of the structure is affected by its own imminent Eigen-motions, the difference between the measurements and actual hydrodynamic force might be significant. Various methods are suggested and applied to obtain actual hydrodynamic force from measurements. For the instance Tanimoto et al. (1986) used the low-pas filter, Wienke & Oumeraci (2005) suggested the deconvolution-convolution technique and Arntsen et al. (2011) applied the Duhamel integral.

The global response of the monopile support structure of offshore wind turbines is in general an order of magnitude slower than the duration of the breaking wave impact that is a momentary process. The impact forces from breaking waves may be more important for the analysis of structure elements than for the global structural response. Hence, it is very important to analyse the distribution of the impact loads on the structure. In order to analyse the impact load distribution, the laboratory model can be constructed from cylindrical elements, where each element presents separate measurement system for measuring strip forces on the cylinder. However, because of relatively large height of the individual cylindrical parts, only few points in the zone of the wave impact area can be considered, which is not sufficient for complete understanding of the impact load distribution from breaking waves. This type of laboratory measurements can be found in the study of Arntsen et al. (2011) and Tanimoto et al. (1986).

In the analysis of the breaking wave interaction with the structures, the effect of the air compressibility may play an important role. The effect of the compressibility of an air pocket is far more pronounced for the case of the breaking wave impact on the vertical wall than for the case of the breaking wave impact on the vertical cylindrical structures. The reason for this is that an air pocket generated between the overturning wave jet and the vertical cylindrical structure is only partially closed, and the compressibility effects are often neglected in analysis. Numerous experimental and theoretical analysis on the effect of air compressibility have been conducted for cases of breaking wave impact on a wall e.g. Chan & Melville (1988), Bullock et al. (2001;2007), Peregrine et al. (2003,2005,2008), Bredmose et al. (2009,2015), Abrahamsen & Faltinsen (2011) and others. The results of aforementioned studies generally show that presence of the trapped air induces damping effects which reduce the impact pressures and impact force. However, results from some studies show that air trapped between the overturning wave jet and the structure can also lead to increased impact forces (Wood et al., 2000).

Because of the effect of the air compressibility, the data from laboratory analysis must be carefully interpreted, as simplified Froude law could lead to significant errors (Bredmose et al., 2015). The results of experiments also depend on a fluid used in an analysis. This is because the effect of air compressibility is different for the fresh water and the seawater, as the size of entrapped air bubbles in saltwater are much smaller than those in freshwater (Scott, 1975).

1.2 Numerical analysis

The application of numerical model enables us to evaluate impact pressures on the structure with high spatial and temporal resolution. Therefore, the results from numerical model can help to improve the understanding of the impact of breaking waves on a structure. In the last two decades, numerous numerical studies have been conducted on the attack of breaking waves on a vertical cylinder. The typical numerical models are based on the solution of the Navier-Stokes (NS) equations for a two-phase incompressible flow by applying the finite volume method. The effects of air compressibility for the case of the braking wave impact on the vertical cylinders are generally neglected. The main assumptions are: (i) initially trapped air between the wave front and the structure can “escape” around the structure, (ii) if the trapped air pocket exist, it would induce cushioning effect and the computed wave loads from incompressible model are on the “safe side”, (iii) influence of the entrapped air bubbles are neglected. The representation of the air-water interface is most widely approximated by the Volume Of Fluid (VOF) method introduced by Hirt & Nichols (1981). In the recent study of Alagan Chella et al. (2015) and Kamath et al. (2016) the air-water interface is approximated with the Level Set Method (LSM).

The numerical model based on solution of the Navier-Stokes equations can represent the breaking wave characteristic with sufficient accuracy, as it is shown in the study of Alagan Chella et al. (2015) where the numerical results are validated with experimental data of Ting & Kirby (1996). Alagan Chella et al. (2015) conducted comprehensive numerical investigation consisted of 39 cases of undisturbed propagation of spilling and plunging wave breakers.

The numerical solution of the breaking solitary wave impact on a cylinder is successfully validated with the laboratory PIV measurements by Mo et al. (2013). The potential of the numerical models for calculation of the violent wave loads on a monopile structure is presented in study of Bredmose & Jacobsen (2010, 2011). However, their numerical results were not compared with experimental data. Xiao & Huang (2015) conducted analysis on breaking solitary wave loads on a pile installed at different positions along an inclined bottom. The computed breaking wave forces from their study are consistent with the numerical results of Mo et al. (2013). The results from the study of Xiao & Huang (2015) show that the reduction of wave loads can be achieved by a proper selection of the location of a pile on a sloping beach.

Choi et al. (2015) investigated the effect of the vibration of a structure on hydrodynamic loads. They validated their numerical model with the filtered and the Empirical Mode Decomposition data from the study of Irschik et al. (2002), which are also used for the validation of the numerical model of Kamath et al. (2016). Kamath et al. (2016) investigated different stages of the plunging breaking wave impact on a vertical cylinder. A similar approach was applied in laboratory experiments by Wienke et al. (2001). Both studies show that the location of the cylinder with respect to the wave breaking point has a significant effect on breaking wave forces. The highest force occurs when the overturning wave jet hits the cylinder just below the wave crest level, and the lowest force is obtained when the wave breaks behind the cylinder.

While the most numerical studies include analysis of wave impact force, the pressure and load distribution on the structure during the wave impact are rarely discussed. In recent study of Ghadirian et al. (2016), discussion on the impact pressure distribution is mainly related to the validation of the numerical model. More detailed discussion on the impact pressure distribution during the wave impact provide Hildebrandt & Schlurmann (2012). They investigated temporal impact pressure distribution on the tripod foundation due to phase-focused breaking wave attack. The model is validated with measured wave elevations and impact pressures obtained from the large scale model tests (1:12). By integrating the computed impact pressures around the structure, the temporal characteristics of the vertical load distribution are estimated. The maximum obtained slamming coefficient is C_s=1.1π, which is considerably lower than the slamming coefficients assessed by applying a simplified approach by Wienke (2001), C_s=2π.

The effect of the breaking wave shape on the characteristics of the impact pressures and the vertical load distribution has not been investigated so far. Therefore, the main objective of this study is to investigate the effect of the breaking wave shape on the impact wave loads on a monopile structure.

1.3 Thesis scope and objectives

In this study the problem of the impact of breaking waves on a monopile structure is investigated. The study focuses on the numerical modeling of the breaking wave impact on the monopile structure for the different steepness and shape of breaking wave front. The investigation focuses on the plunging breaking wave with breaking location slightly before the structure, so that the overturning wave jet hits the monopile just below the wave crest level. This is usually identified as the most violent breaking wave stage. The derived numerical model for the aforementioned analysis is based on incompressible NS-VOF equations. This study also addresses the problem of the effect of air compressibility on the interaction between a breaking wave and the monopile structure. The present study shows comparison between the results of the applied incompressible numerical model and compressible numerical model derived for model and prototype scales.

The main objective of this thesis is to investigate the effect of the breaking wave shape on the load distribution arising from the breaking wave impact on a monopile structure. The simplified estimation of the breaking wave loading on the monopile structure which is applied in engineering practice is based on approximation of the rectangular vertical impact load distribution. The parameters of the rectangular load distribution are not considered as a function of the shape of the breaking wave profile. The goal of the study is to show that the parameters of the rectangular shape distribution applied in engineering practice are complex function of the breaking wave shape and cannot be uniquely defined beforehand.

The pressure distribution on the monopile structure during the breaking wave impact is analysed with very high temporal resolution. Therefore, the mechanism of the breaking wave impact is examined with more details than it is usually conducted in existed numerical studies. The majority of the existed numerical models are based on the Volume of Fluid model for description of the air-water interface. According to the authors knowledge, the influence of the thickness of the air-water interface on the characteristics of the impact pressure and impact force has not been investigated so far. This study includes aforementioned analysis as well.

Furthermore, this study presents the results from experimental analysis of wave loading on the monopile structure installed in relatively shallow water. The conducted experiments simulate 50-year storm condition which is expected to occur in the German Bight. Laboratory experiments were conducted for two scenarios, where for each scenario more than 5000 waves were generated. For one experimental scenario the monopile structure was installed on the flat seabed and for the second scenario on the sand-bar with the slope m=1:21. The derived results from numerical model are compared with experimental data. The validation of the derived numerical model focuses on measurements for which the maximum hydrodynamic force on the structure is recorded.

2 Theoretical models

This chapter provides the basic information about the characteristics of the breaking waves and characteristics of the hydrodynamic loading for different stages of the breaking wave interaction with the structure, as presented in Veic & Sulisz, (2018). The chapter includes comparison between the impact forces obtained by applying the derived numerical model and results of simplified approaches applied in engineering practice, as presented in Veic et al. (2019). The derived numerical model is based on solution of the incompressible NS equations, where the air-water interface is approximated by the VOF method. The influence of the thickness of the air-water interface on the computed impact pressures and impact load is analysed. The numerical analysis applied in this chapter focuses on interaction between the breaking wave and the monopile structure for different characteristic of the breaking wave shape. Furthermore, this chapter addresses the question of the effect of the air compressibility which can be trapped between the overturning wave jet and the monopile structure.

2.1 The breaking wave characteristic

Many studies have been conducted in an attempt to understand the fundamental physics of breaking waves, but due to complexity of the problem, uniform conclusions are still not achieved. The discussion about the determination of the geometric properties of the breaking waves, wave-breaking onset, and the estimation of the breaking wave energy dissipation is discussed in comprehensive literature review of Perlin et al. (2013). This section presents the breaking wave characteristics generally which are accepted in engineering practice.

There are three general criterions for the determination of the onset of the breaking waves: the geometric, kinematic and the dynamic criterion. As it is defined in Banner & Phillips (1974): "*A breaking wave can be defined as one in which certain fluid elements at the free surface (near the wave crest) are moving forward at* *a speed greater than the propagation speed of the wave profile as a hole.*" This presents the kinematic criterion for the wave breaking. The dynamic breaking wave criterion is defined when the vertical particle acceleration exceeds the half of the gravitational acceleration. The geometric wave characteristic presents the most common criterion for determination of the breaking wave onset.

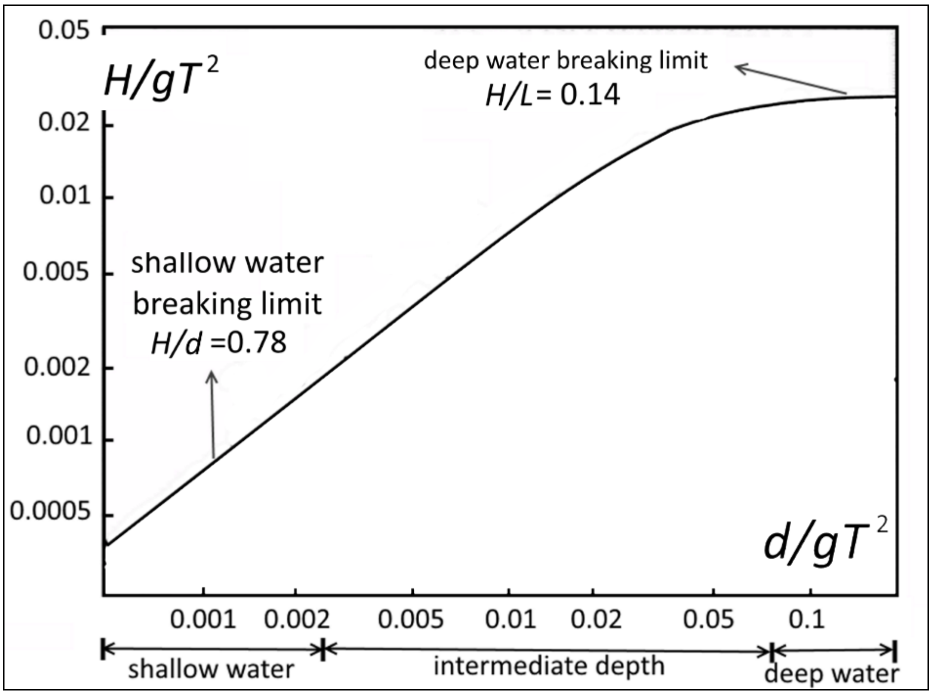

Figure 2.1 The breaking wave criterion applied in DNV (2014)

According to the regulation standard DNV (2014), the geometric criterion for the maximum wave height in intermediate water depths is (Figure 2.1):

$$H_b = 0{,}124L \tanh \frac{2\pi d}{L} \tag{2.1}$$

where L is wave length and d is water depth. For the case of deep waters ($d > 0.5\ L$), breaking wave limit is:

$$H_b = 0.142L \tag{2.2}$$

while for the case of shallow waters ($d < 0.05\ L$), breaking wave limit is:

$$H_b = 0.78d \tag{2.3}$$

The breaking waves can be classified as: surging, spilling, plunging, and collapsing breakers (Figure 2.2). The surging breakers are low waves which are relatively unbroken. The spilling breakers gradually spills forward down from the wave front face. The plunging breakers are characterized by the overturning front face and the formation of the overturning water jet that plunges into the trough ahead of it and causes the large splash. The collapsing breakers are blend between surging and plunging breakers, where the lower portion of the front face gets vertical and collapses.

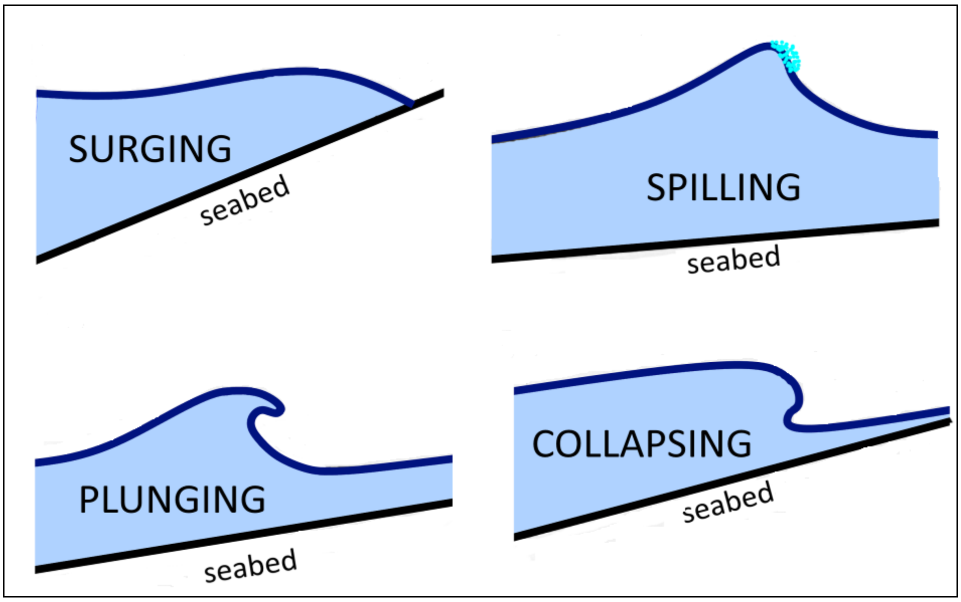

Figure 2.2 The breaking wave types

Different mechanisms of the generation of breaking waves exist, such as shoaling, dispersive focusing, wind forcing, and wave-current interaction. Battjes (1974) presented a classification of the wave breaking types for the monochromatic waves which breaks over a sloped seabed. He introduced a surf similarity parameter, which is the ratio of the seabed slope m, and the offshore wave steepness H_0/L_0 (where H_0 and L_0 are wave height and wave length in deep waters, respectively).

$$\xi = \frac{m}{\sqrt{H_0/L_0}} \tag{2.4}$$

Transition between the different types of breaking waves as a function of the surface similarity parameter is presented in Figure 2.3 (DNV,2014).

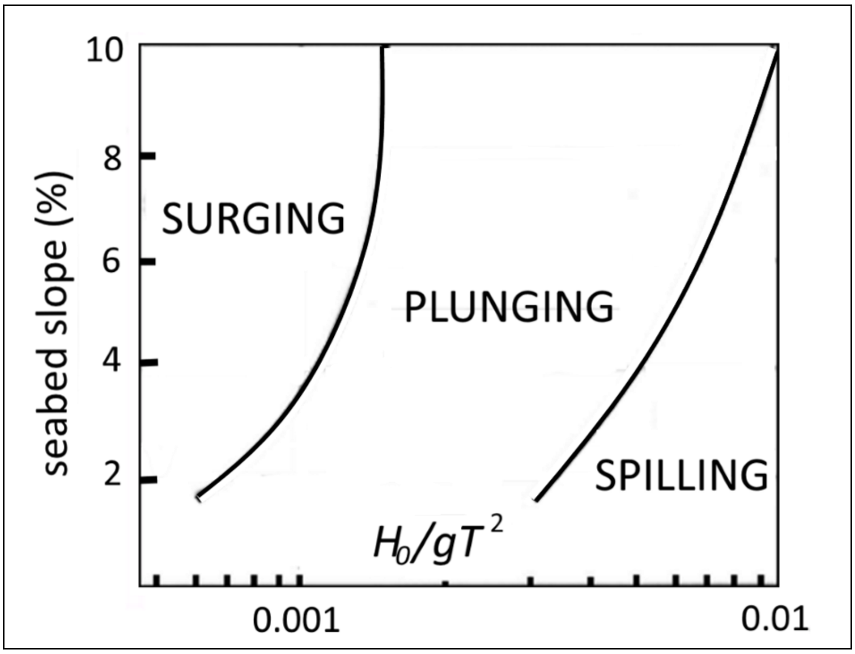

Figure 2.3 Classification of the breaking wave types according Battjes (1974)

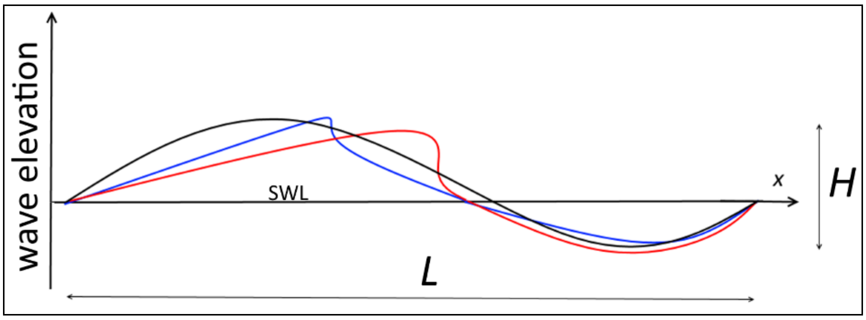

Figure 2.4 The asymmetric profile of the breaking wave

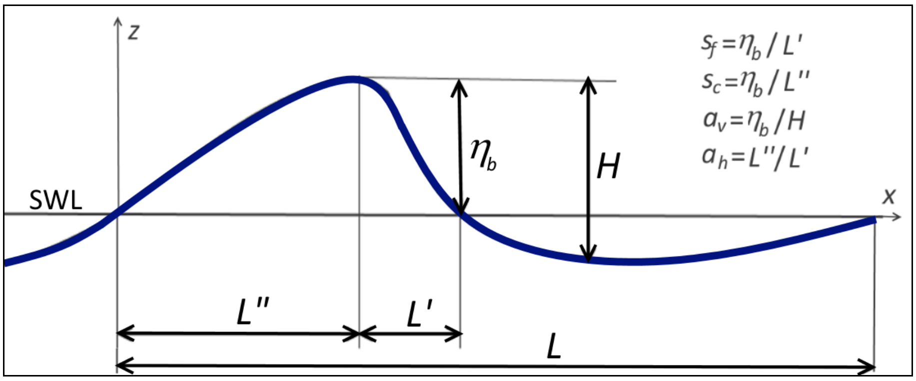

Figure 2.5 The asymmetric parameters of the breaking wave profile

Table 2.1 The asymmetric breaking wave parameters, Bonmarin (1989)

Breaker type	Min.	Max.	Mean
s_f- front crest steepness			
Typical plunging	0.31	0.85	0.61
Plunging	0.29	0.77	0.47
Spilling	0.24	0.68	0.41
Typical spilling	0.31	0.51	0.38
s_c- rear crest steepness			
Typical plunging	0.24	0.33	0.29
Plunging	0.20	0.42	0.30
Spilling	0.19	0.42	0.31
Typical spilling	0.26	0.48	0.33
a_v- vert. asym. factor			
Typical plunging	0.65	0.93	0.77
Plunging	0.62	0.93	0.76
Spilling	0.59	0.91	0.75
Typical spilling	0.60	0.80	0.69
a_h- horiz. asym. factor			
Typical plunging	0.97	3.09	2.14
Plunging	0.78	2.52	1.61
Spilling	0.78	2.37	1.38
Typical spilling	0.81	1.72	1.20

As wave approaches the breaking onset, the wave front becomes very steep and the wave profile is very asymmetric (Figure 2.4). The geometric parameters H, T and L are insufficient for description of the asymmetric wave profile. For more accurate presentation of the asymmetric wave characteristics Kjeldsen & Myrhaug (1979) introduced additional geometric wave parameters (Figure 2.5). Referring to their study, the parameters included in this study are addressed as (i) crest front steepness, $s_f = \eta_b / L'$, (ii) crest rear steepness, $s_r = \eta_b / L''$, (iii) vertical asymmetry factor, $a_v = \eta_b / H'$, (iv) horizontal asymmetry factor, $a_h = L''/L'$. Bonmarin (1989) studied characteristics of the phase focused breaking waves in deep water, and suggested ranges of asymmetric parameters for different types of breaking waves (Table 2.1).

The impact loading from breaking waves on vertical cylinders is very sensitive to the stage of the wave breaking in respect to the structure position. Five different stages of the plunging breaking wave interaction with the structure are generally identified (Wienke et al.,2001), as presented in Figure 2.6. Stage (i) presents scenario where wave breaks at the rear side of the structure. For this stage of the breaking wave interaction with the structure, the structure is not excited by the impact loading. Stage (ii) presents scenario where wave brakes at the front line of the structure. In this scenario the breaking wave interaction with the structure is significantly influenced with the wave run-up on the structure. Because of the influence of the wave run-up, the impact loading on the structure is significantly damped. Stage (iii) presents scenario where wave breaks immediately in front of the structure and the overturning wave jet hits the structure at the wave crest level. Stage (iv) is similar to the stage (iii), but in this scenario the overturning wave jet hits the structure just below the wave crest level. Stage (v) presents scenario where wave breaks far before the front line of the structure. In this scenario the overturning wave jet hits the structure far below the wave crest level and the impact loading is characterized by two characteristic peaks. The first peak is related to the impact of the wave tongue on the structure, while the second peak is related to the impact of the wave front on the structure. The maximum impact loading on the structure is generally identified for the stage (iv), which is the stage of the breaking wave impact analysed in this study.

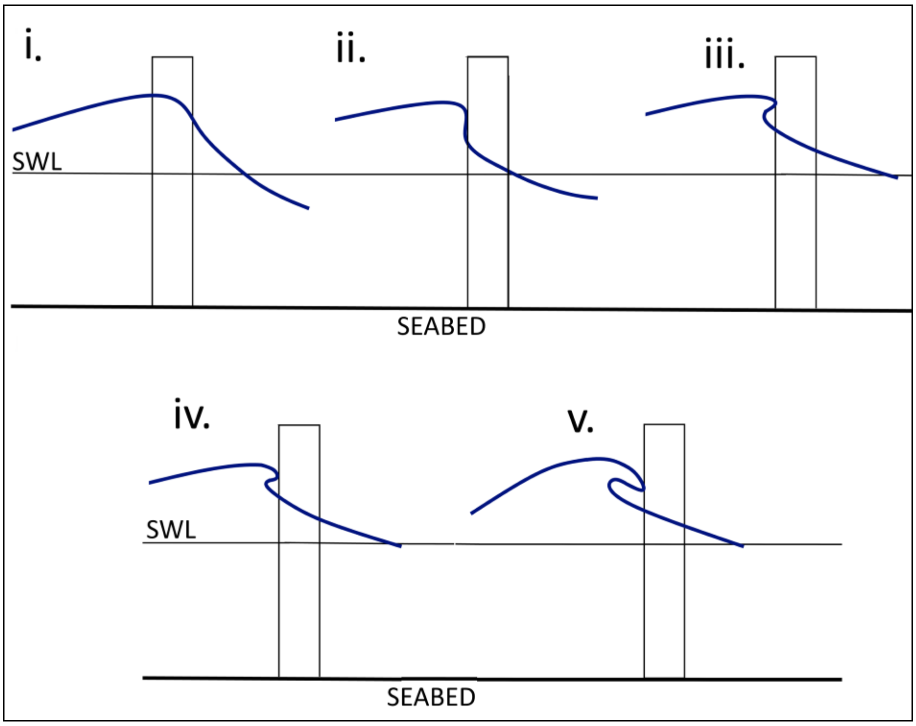

Figure 2.6 Stages of the plunging breaking wave impact

2.2 Analytical approach

Offshore structures are design according to the recommended design standards. For slender cylindrical structures (D<0.2L), such as jacket and monopiles, hydrodynamic load is usually estimated according to the well-known Morison's equation (Morison et al., 1950). The hydrodynamic inline force for the case of non-breaking waves is calculated as (DNV, 2014) :

$$
\begin{aligned}
F_M &= F_m + F_d \\
&= \int_{-d}^{\eta(t)} C_m \rho \pi \frac{D^2}{4} \dot{u} \qquad \int_{-d}^{\eta(t)} {}_d \rho \frac{D}{2} |u| u dz
\end{aligned}
\tag{2.5}
$$

where the first term in equation presents an inertia and second term a drag force. Empirical coefficients C_m and C_d denote the drag and inertia coefficients, respectively, and they are generally estimated as a function of Keulegan-Carpenter (KC) number, Reynolds number (Re) and surface roughness (DNV, 2014). The inertia and the drag force are function of the wave particle acceleration ($\dot{u}$) and the wave particle velocity (u), respectively. The acceleration is in most cases accurately approximated by the linear Eulerian derivative $\partial u/\partial t$, however for the case of highly non-linear waves the Lagrangian acceleration is more appropriate.

$$\dot{u} \quad \frac{\mathrm{d}u}{\mathrm{d}t} \quad \frac{\partial u}{\partial t} + u\frac{\partial u}{\partial x} + v\frac{\partial u}{\partial y} + w\frac{\partial u}{\partial z} \tag{2.6}$$

For the cylinder where the axial dimension is not slender, Rainey (1989) presented extension of the Morison's equation which includes additional inertia term $u\partial w/\partial z$.

$$F_R = \int_{-d}^{\eta(t)} \rho \pi R^2 \frac{\partial w}{\partial z} u dz \tag{2.7}$$

Application of the Morison's equation is considered as a good engineering approximation of the hydrodynamic loading on the monopile structure excited by the weakly non-linear waves. For the case of highly non-linear waves, higher frequency wave components might coincidence with the natural frequency of the structure and induce amplified structural response. This effect is recognized as a ringing phenomenon, and has been subject of many studies. For more information about the ringing effects reader is addressed to the comprehensive study of Paulsen (2013a). He showed that the detailed wave loading in the region of the free-surface as well as higher harmonic of nonlinear wave loading are beyond the scope of both the Morison's equation and the existed perturbation theories (Faltinsen et al., 1995; Malenica & Molin, 1995).

When waves are likely to break on the structure or in its vicinity, wave loads from breaking waves must be considered in design of the structure. As impact forces from breaking waves are completely out of the scope of the Morison's equation, additional force component is introduced.

$$F = F_M + F_i \tag{2.8}$$

The recommendation for calculation of plunging breaking wave impact force according to the DNV (2010, 2014) standard is:

$$F_i = \frac{1}{2}\rho C_s A u^2 \tag{2.9}$$

Where A is the area on the structure which is assumed exposed to the slamming force, and C_s is the slamming coefficient. For the smooth cylindrical surface the slamming coefficient is in the range $3<C_s<2\pi$. The impact velocity u should be taken as 1.2 c_b of the most probable highest breaking wave in n-years. The most probable largest breaking wave height may be taken as H_b=1.4H_s in n-years. The area exposed to the wave impact corresponds to the height of 0.25H_b and the azimuth angle 45deg. Under these hypotheses, the impact force formulation can be rearranged as:

$$F_i = \frac{1}{2}\rho C_s (\frac{45}{360} \cdot D\pi \frac{H_b}{4})(1.2c_b^2) \tag{2.10}$$

As recommended in IEC (2005) standard, the impact force from breaking waves on slender cylindrical structures may be calculated according to simplified approach proposed by Wienke (2001). Wienke model is based on an analytical solution presented in study of Wagner (1932) which describes the impact of infinitely long cylinder on the calm water with the constant speed. This model is based on a potential flow theory, where the flow is assumed to be incompressible, inviscid and irrotational. Furthermore, the surface tension of the fluid and forces due to gravity are neglected and the cylinder is assumed to be rigid. The pressure is calculated according to the Bernoulli equation:

$$p = -\rho \frac{\partial \Phi}{\partial t} - \frac{\rho}{2}\left[(\frac{\partial \Phi}{\partial x})^2 + (\frac{\partial \Phi}{\partial y})^2 \right] + p(t) \tag{2.11}$$

where Φ presents the potential flow around the cylinder. The conformal mapping technique is applied to describe the flow around the cylinder with the flow around the flat plate (Newman & Landweber, 1978):

$$\Phi = -V\sqrt{m(t)^2 - x^2} \qquad ; \quad for|x| < m \tag{2.12}$$

where V is velocity of the impact, *m(t)* presents the half of the plate width, and x is the exact location on the flat plate, so that $x = m$ defines the edge of the flat plate, as it is illustrated in Figure 2.7.

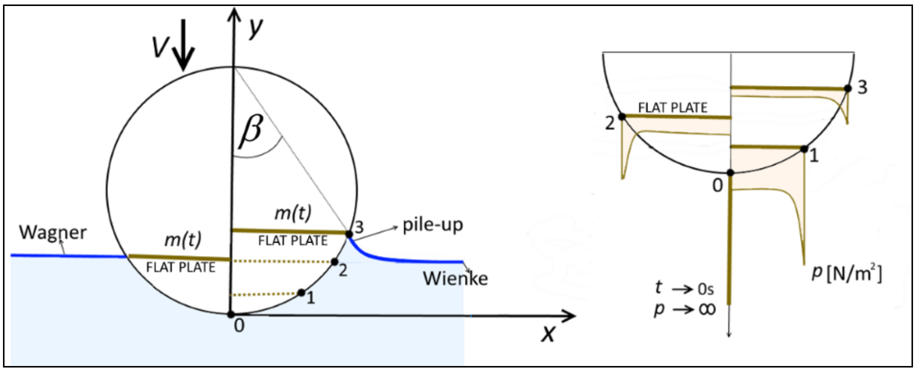

Figure 2.7 Wienke 2D simplified model

Wagner's model considers only the time derivative in Bernoulli equation, while Wienke's model includes non-linear terms as well. Wienke solution of the Bernoulli equation is:

$$p(x) = \frac{1}{2}\rho V^2 \left(\frac{2}{V\sqrt{1-(\frac{x}{m(t)})^2}} \frac{dm(t)}{dt} - \frac{1}{1-(\frac{x}{m(t)})^2} \right) \tag{2.13}$$

It could be seen that $p \to \infty$ for $x \to m$. The schematic view of the pressure distribution on the flat-plate for different moments of cylinder immersion is presented in Figure 2.7. During the impact, water is pushed away by the cylinder, and the free-surface is deformed in the zone around the edge of the contour. This is described as a pile-up effect which causes accelerated immersion of the cylinder, higher wetted area and shorter duration of the impact. Taking into account the pile-up effect, Wienke defined temporal variation of the flat-plate as:

$$
\begin{aligned}
0 \le x \le R/\sqrt{2} \quad &\rightarrow \quad m = 2R\sqrt{\frac{V}{R}t} \\
R/\sqrt{2} \le x \le R \quad &\rightarrow \quad m = R\sqrt[4]{\frac{8}{3}\frac{V}{R}t}
\end{aligned}
\tag{2.14}
$$

Considering the breaking wave impact on the structure, constant velocity V denotes the water particle velocity u at the time of the impact. Assuming that breaking wave occurs when water particle velocities exceed the wave celerity, Wienke proposed application of the $u=c_b$ for the calculation of the breaking wave impact force. By integration of the pressure distribution along the flat plane, the line impact force f_i which acts in 2D plane can be calculated.

- *for* $0 \le t \le \frac{1}{8}\frac{R}{V}$;

$$f_i(t) = \rho R c_b^2 \underbrace{\left[2\pi - 2\sqrt{\frac{c_b}{R}t} \cdot a\tanh\sqrt{1 - \frac{1}{4}\frac{c_b}{R}t} \right]}_{C_S}$$

$$\tag{2.15}$$

- *for* $\frac{3}{32}\frac{R}{c_b} \le t' \le \frac{12}{32}\frac{R}{c_b}$, *where* $t' = t - \frac{1}{32}\frac{R}{c_b}$

$$f_i(t) = \rho R c_b^2 \underbrace{\left[\pi\sqrt{\frac{1}{6}\frac{R}{c_b t'}} - \sqrt[4]{\frac{8}{3}\frac{c_b}{R}t'} \cdot a\tanh\sqrt{1 - \frac{c_b}{R}t'\sqrt{6\frac{c_b}{R}t'}} \right]}_{C_S}$$

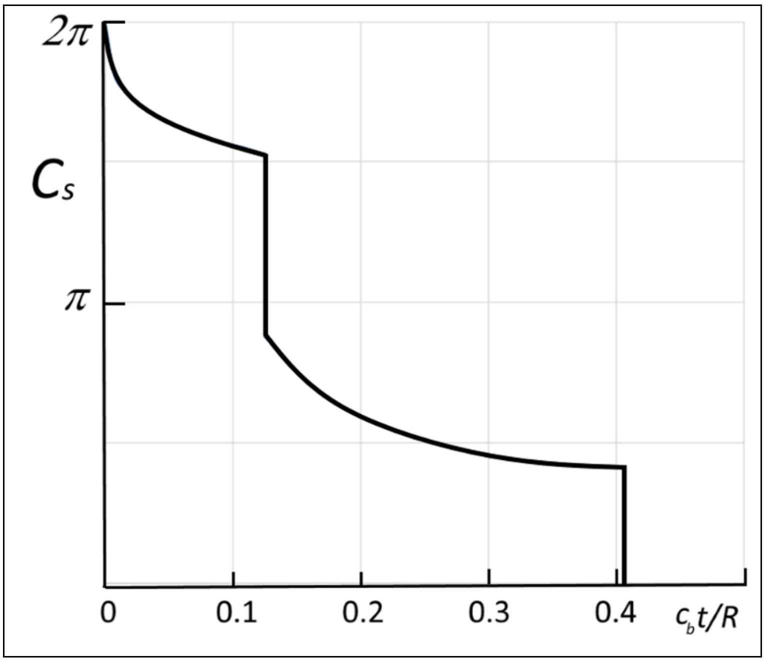

Figure 2.8 Slamming coefficient solution, Wienke (2001)

The solution for the slamming coefficient $C_s(t)$ is presented in Figure 2.8. The maximum slamming coefficient is $C_s(t=0)=2\pi$, which is two times larger than theoretical estimation of von Karman (1929) who neglect the pile-up effect. To obtain the total impact force from breaking wave on a vertical cylinder, Wienke suggested rectangular distribution of the line impact forces (Figure 2.9). The total impact force is calculated as:

$$F_i(t) = \rho c_b^2 R C_s \lambda \eta_b \tag{2.16}$$

where the curling factor λ defines the vertical area of the impact with respect to the wave crest height η_b.

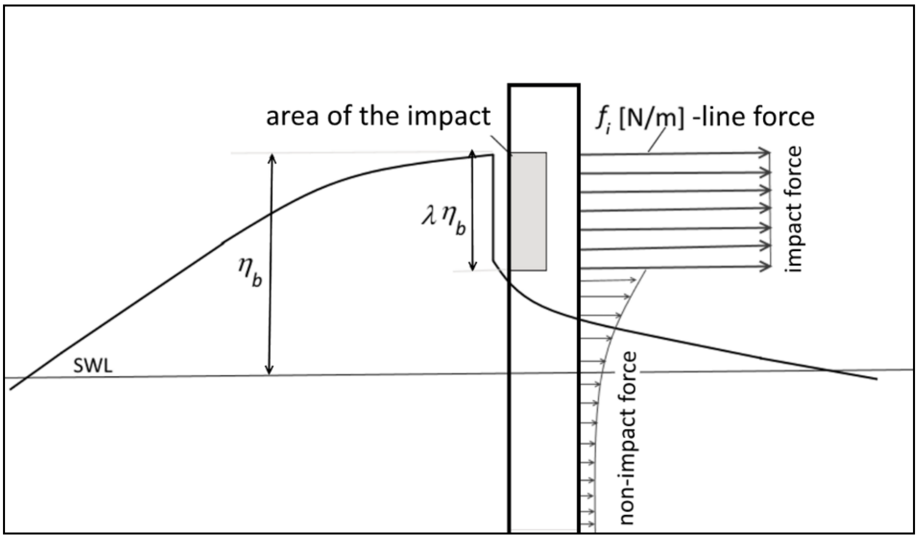

Figure 2.9 Rectangular distribution of the impact load

In the study of Wienke & Oumeraci (2005) the curling factor is estimated semi-empirically according to the experimentally measured impact force and the maximum theoretical value of the slamming coefficient C_s=2π.

$$\lambda = \frac{F_{i\max}(measured)}{\rho c_b^2 R C_s \eta_b} \tag{2.17}$$

For the case of plunging breaking wave impact on the vertical pile Wienke & Oumeraci (2005) assessed λ=0.4-0.6. The duration of the impact force suggested by Wienke is:

$$T_{Fi} = T_{fi} = \frac{13}{32}\frac{R}{c_b} \tag{2.18}$$

2.3 Numerical model

In order to correctly describe the mechanism of a breaking wave, the wave kinematics must be accurately described significantly before the wave breaking location. In the case of breaking waves in shallow or intermediate waters, the numerical domain should be long enough to capture the influence of bathymetry from the moment the wave starts to be influenced by the seabed. A propagating wave with wave length $L \approx 250$m feels the influence of the seabed already at depths $d<125$m. Assuming a monopile structure installed at a 10% sloped seabed in a depth $d=30$m, where the toe of the slope is $d_{toe}=125$m, the wave starts to be influenced by the seabed almost 950m before the location of the structure (or 95 monopile diameters). The area where the breaking wave hits the structure is almost two orders of magnitude smaller than the required size of the numerical domain. Such a long numerical domain with significant difference in characteristic length scales is computationally expensive. In numerical studies by Kamath et al. (2016) on the breaking wave impact on a cylindrical structure, the numerical domain consists of 15 million computational cells with a grid size $dx=0.07D$. Such a large numerical domain is solved using a supercomputer with a large number of processors (applied supercomputer "Vilje" consists of 1404 nodes with two 8 core processors on each node, resulting in a total of 22464 cores)

In order to reduce the computational cost, the solution is to decompose the problem in to an inner and an outer region. A numerical model used in this study is based on the decomposition technique suggested by Paulsen et al. (2014), where the wave propagation in the outer region is solved by applying a fully nonlinear potential flow model, OceanWave3D, while the process of wave breaking and the breaking wave impact on a structure is studied by using the Navier-Stokes (NS) equations and the open-source CFD toolbox OpenFoam® (Figure 2.10).

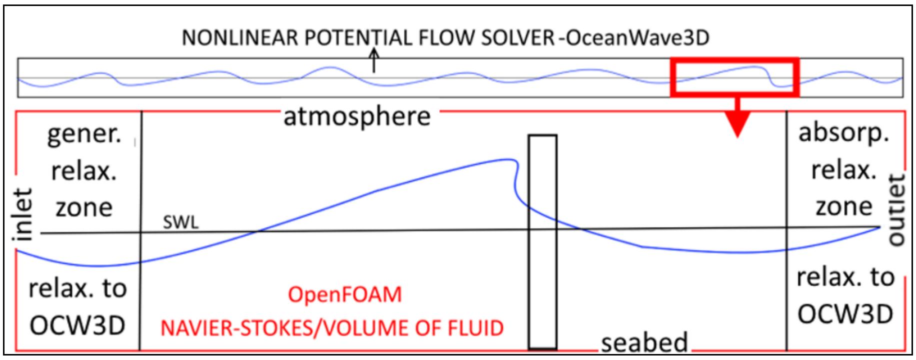

Figure 2.10 Sketch of the decomposed numerical domain

In the laboratory study presented in chapter 3, the monopile structure is installed at distance ≈16 wave lengths from the wave maker position. With the proposed numerical technique a much smaller numerical domain is sufficient for reproducing the laboratory breaking wave. In the decomposed numerical domain the monopile structure is located ≈1 wave length away from the inlet boundary surface. In order to correctly simulate the laboratory breaking wave, application of the non-decomposed numerical domain will require simulation of wave propagation for a duration of ≈30s. With the application of the decomposed numerical domain, the simulation of the wave propagation for a duration of ≈1s is sufficient. This technique considerably reduces the computation time.

The breaking wave interaction with the monopile structure and the effect of the breaking wave shape on the impact load distribution are analysed by solving the incompressible NS equations. The air-water interface is solved by applying the Volume of Fluid (VOF) method. The incompressible NS-VOF set of equations are discretized using a finite volume approximation on unstructured grids. The conservation of mass is governed by the incompressible continuity equation:

$$\nabla \cdot \mathbf{u} = 0 \tag{2.19}$$

where $\mathbf{u} = (u, v, w)$ and u, v and w are the velocity components in the Cartesian coordinate system. The incompressible Navier-Stokes equation is:

$$\frac{\partial \rho \mathbf{u}}{\partial t} + \nabla(\rho \mathbf{u})\mathbf{u} = -\nabla p^* - (\mathbf{g} \cdot \mathbf{x})\nabla \rho + \nabla \cdot (\mu \nabla \mathbf{u}) \tag{2.20}$$

where, ρ is the density, $p*$ is the pressure in excess of the hydrostatic pressure, $\mathbf{g}$ is the acceleration due to gravity, $\mathbf{x}$ is the Cartesian coordinate vector, μ is the dynamic molecular viscosity. The free surface separating the air and water phase is captured using a volume of fluid surface capturing scheme, which solves the following equation for the water volume fraction α:

$$\frac{\partial \alpha}{\partial t} + \nabla \cdot \mathbf{u}\alpha + \nabla \cdot \mathbf{u}_r \alpha(1-\alpha) = 0 \tag{2.21}$$

In which $\mathbf{u}_r$ is a relative velocity, which helps to retain a sharp water-air interface (Berberović et al., 2009). The marker function α is 1 when the computational cell is filled with water and 0 when it is empty. In the free surface zone the marker function will have a value in the interval $\alpha \epsilon [0;1]$ indicating the volume fraction of water and air, respectively. The fluid density and viscosity are assumed continuous and differentiable in the entire domain and the following linear properties are adopted:

$$\begin{aligned} \rho &= \alpha \rho_w + (1-\alpha)\rho_a \\ \mu &= \alpha \mu_w + (1-\alpha)\mu_a \end{aligned} \tag{2.22}$$

The time step is controlled by adaptive time stepping procedure based on the Courant-Friedrichs-Lewy criterion. For all the computations, the maximum Courant number is kept below 0.2. To generate fully nonlinear boundary conditions at the inlet and outlet boundary of the NS-VOF domain, the potential flow solver OceanWave3D developed by (Engsig-Karup et al. (2009) is applied. The model solves the three-dimensional Laplace problem in Cartesian coordinates while satisfying the dynamic and kinematic boundary conditions. For an inviscid and incompressible fluid, a velocity potential ϕ exists which relates to the Cartesian velocities by $(u,v;w) = (\nabla_H \phi; \partial z \phi)$, where $\nabla_H = (\partial_x, \partial_y)$ is the horizontal gradient and ∂z indicate differentiation with respect to the vertical coordinate z. The temporal evolution of the free surface, η, and the velocity potential at the free surface $\tilde{\varsigma}$ is governed by the kinematic and dynamic free surface condition respectively. When expressed in terms of the free surface variables $\tilde{\varsigma}$ and $\tilde{\imath}$ the two surface conditions take the following form

$$\partial_t \eta = -\nabla_H \eta \cdot \nabla_H \tilde{\varsigma} \quad \ldots \cdot \nabla_H \eta) \tag{2.23}$$

$$\partial_t \tilde{\varsigma} \quad \ldots \frac{1}{2} \ldots \cdot \nabla_H \eta)) \tag{2.24}$$

The two differential equations (eq. (2.23) and eq. (2.24)) are evolved in time using a classic fourth-order five-step Runge-Kutta method. In order to determine the velocity potential at the free surface ($\tilde{\varsigma}$), the velocity potential has to be known in the entire fluid volume. This is done by solving the Laplace equation satisfying the kinematic bottom condition;

$$\phi = \tilde{\varsigma}, \quad \ldots \tag{2.25}$$

$$\nabla_H^2 \phi + \partial_{zz} \phi = 0, \quad -h \le z \le \eta \tag{2.26}$$

$$\partial_z \phi + \nabla_H h \cdot \nabla_H \phi = 0, \quad z = -h \tag{2.27}$$

Here $h = h\ (x,y)$ is the water depth with respect to still water level. The Laplace equation is solved in a σ-transformed domain using higher order finite differences for numerical efficiency and accuracy. For details about the accuracy and performance of the potential flow solver, see Engsig-Karup et al. (2009).

The one-way coupling between the OceanWave3D and the OpenFOAM solver is obtained with the waves2Foam utility developed by Jacobsen et al. (2012). The coupling zones correspond to the relaxation zones (Figure 2.11), where the target solution ψ_{target} is given by the potential flow solver. The velocity field and the water volume fraction in coupling zones are updated each time step according to:

$$\psi = \chi \psi_{target} + (1-\chi)\psi_{com} \; ; \quad \psi \in (u, v, w, \alpha) \tag{2.28}$$

where ψ_{com} is the numerically computed solution from equations (2.19), (2.20) and (2.21). The weighting factor $\chi(\xi)$ is defined as:

$$\chi(\xi) = 1 - \frac{\exp(\xi^{\beta}) - 1}{\exp(1) - 1} \tag{2.29}$$

where $\xi \in [0;1]$ is a local coordinate, which is zero at the outer edge of the coupling zone and one at the inner edge of the coupling zone (Figure 2.11). A shape factor of β=3.5 is used in this study. However, it may be noted that the efficiency of the coupling zone is only weakly dependent on β (Paulsen et al., 2014). A detailed discussion on the relaxation zones is given in Jacobsen et al. (2012).

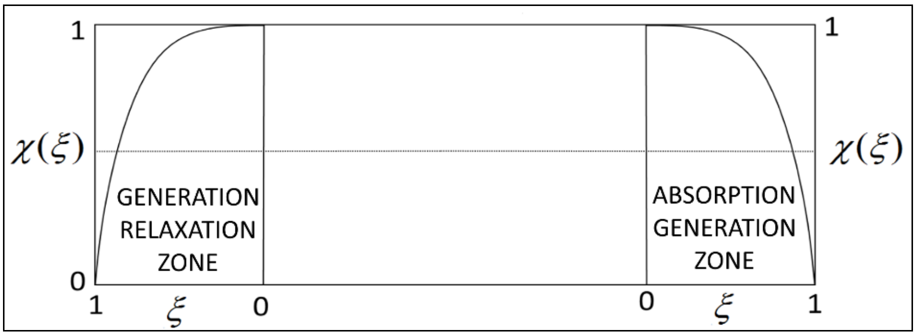

Figure 2.11 Relaxation technique for numerical coupling

In order to decrease the computation time, a symmetry plane is introduced and only half of the domain is considered. The width of the numerical domain is 5*D*. As already mentioned, the solution of the NS-VOF domain in the inlet and outlet zones are relaxed towards the known solution of the potential flow solver OceanWave3D. At the atmosphere boundary inlet/outlet boundary conditions are applied. At the seabed and the lateral boundary, the slip condition is applied. Moreover, the slip condition is applied on the monopile structure, so the viscous effects on wave loads are neglected. This is justified because in the area of the breaking wave impact on a structure, the viscous effect can be neglected due to impulsive loading, while the area below the breaking wave impact is characterized by an oscillating flow and the inertia forces dominate due to a low Keulegan-Carpenter number $KC<15$ (Sumer & Fredsøe, 2006).

The initial stage of the formation of the overturning wave jet is generally governed by the irrotational motion (Battjes, 1988). As this stage of the breaking wave impact is the main focus of the present study and the viscous effects on the wave loading are neglected, the presented numerical model is solved without inclusion of the turbulence models.

2.4 The thickness of the air-water interface in VOF model

To achieve numerical accuracy, the size of the computational grid in the zone of the air-water interface have to be adequately refined. The numerical simulation of the non-breaking wave propagation usually requires 15-20 computational cells per wave height. However, to capture the process of the wave crest breaking, additional computational grid refinement is necessary. Around 45 computational cells per wave height are used for the simulation of the undisturbed breaking wave in this study. However, in order to analyse the breaking wave interaction with the monopile structure, the computational grid has to be further refined in the region of the wave impact on the structure.

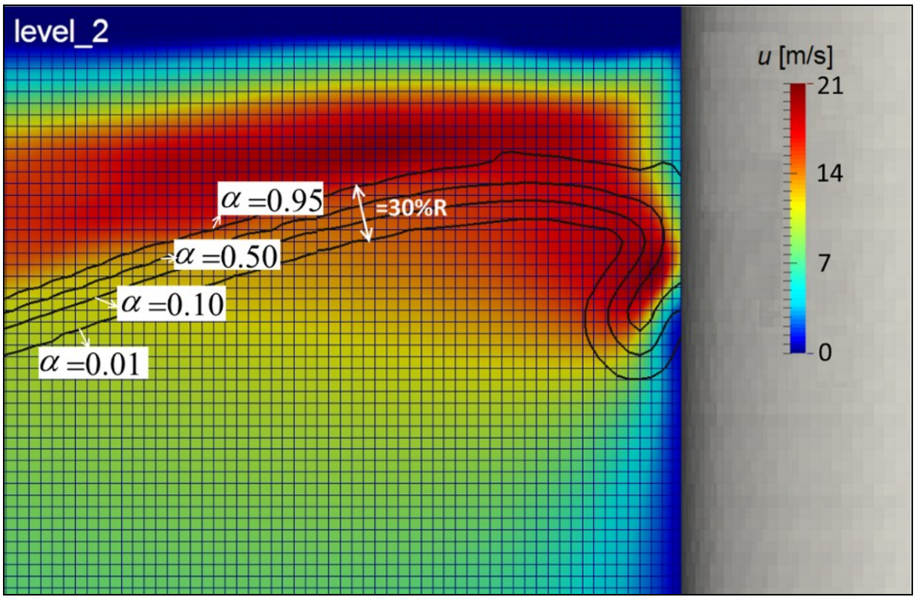

Figure 2.12 The free surface thickness and horizontal velocity field (u)

Because of the application of the VOF method, the initially sharp air-water interface gets smeared due to the numerical discretisation error, as illustrated in Figure 2.12 and Figure 2.13. Additionally, because of the coupling between the pressure gradient ∇p^* and the density gradient $\nabla \rho$ in the momentum equation, spurious air velocities are present in the air phase near the air-water interface (Vukcevic, 2016). This is illustrated in Figure 2.12, which shows horizontal velocity distribution prior to the wave impact on the structure and distribution of the wave profiles for different water fraction levels in computational cells, α = 0.01, 0.1, 0.5, 0.95. The sharpness of the air-water interface where $\alpha \epsilon [0;1]$ depends on the grid size. Figure 2.13 and Figure 2.14 present the computational grid refinement zones applied in this study. The computational grid level 5 refers to $dx=dy=dz=$ 0.5mm= 0.003D.

The density of the air-water mixture depends on the marker function α. For a thicker air-water interface, the rate of change from $\rho=\rho_a$ to $\rho=\rho_w$ is slower, which affects the pressure in the momentum equation. In order to analyse the effect of the thickness of the air-water interface on the computed impact pressure, a computational grid sensitivity analysis is conducted. All simulated cases relate to the same breaking wave case and the same initial solution, and the distance between the overturning wave jet and the structure is ≈0.2D (Figure 2.13).

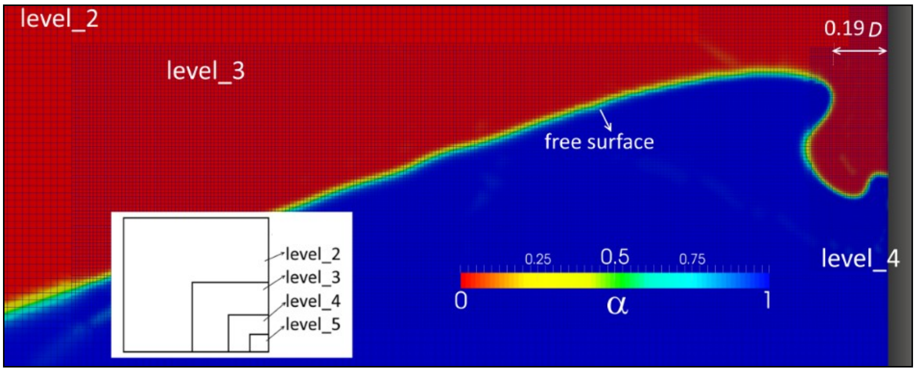

Figure 2.13 Computational grid refinement zones
; level_5: dx=dy=dz=0.5mm≈0.003D

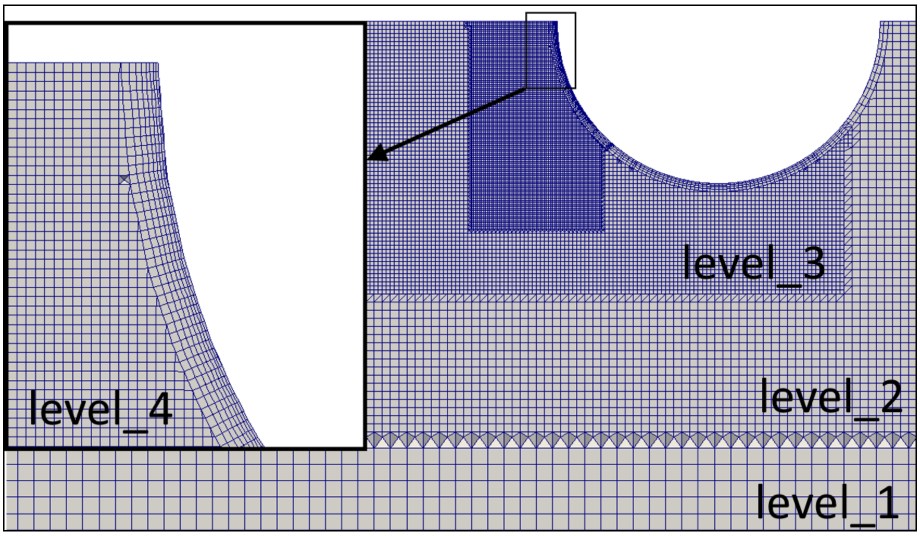

Figure 2.14 Computational grid refinement in the zone of the wave impact area

Figure 2.15 and Figure 2.16 show how the application of the different levels of the computational grid refinement influence the impact pressure in space and time, respectively. Figure 2.17 presents the computational grid sensitivity analysis on the computed impact force. The presented figures show that the computed impact pressures and the corresponding computed impact force are significantly affected by the application of the different levels of grid refinement in the region of wave impact.

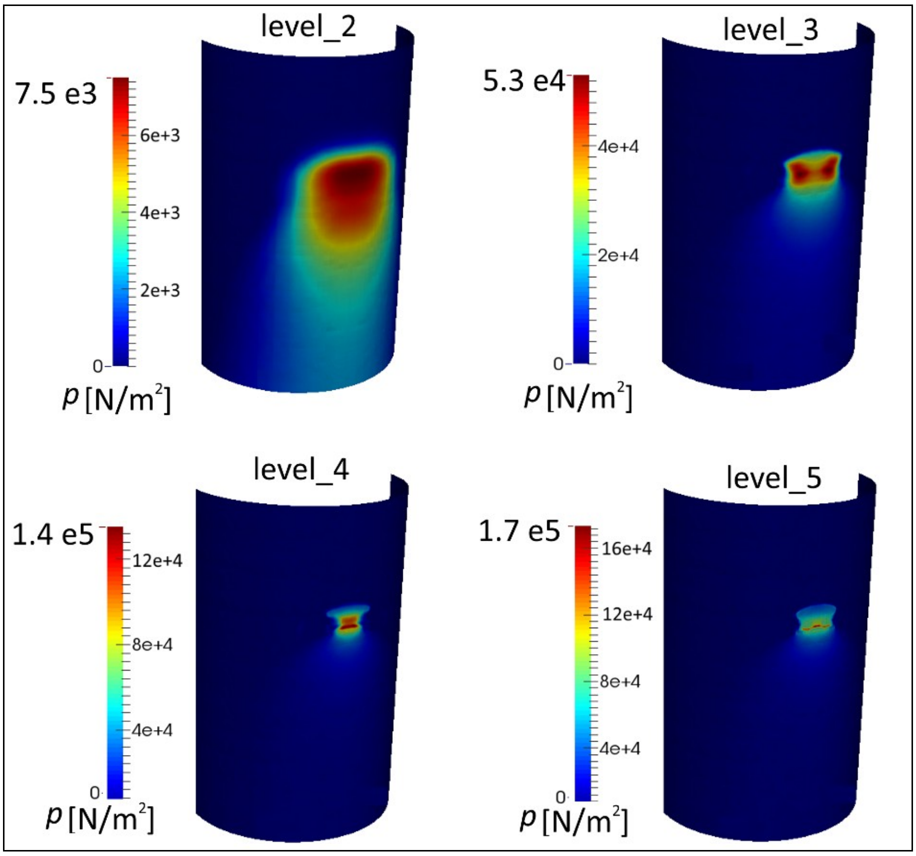

Figure 2.15 Pressure distribution for different levels of the computational grid refinement

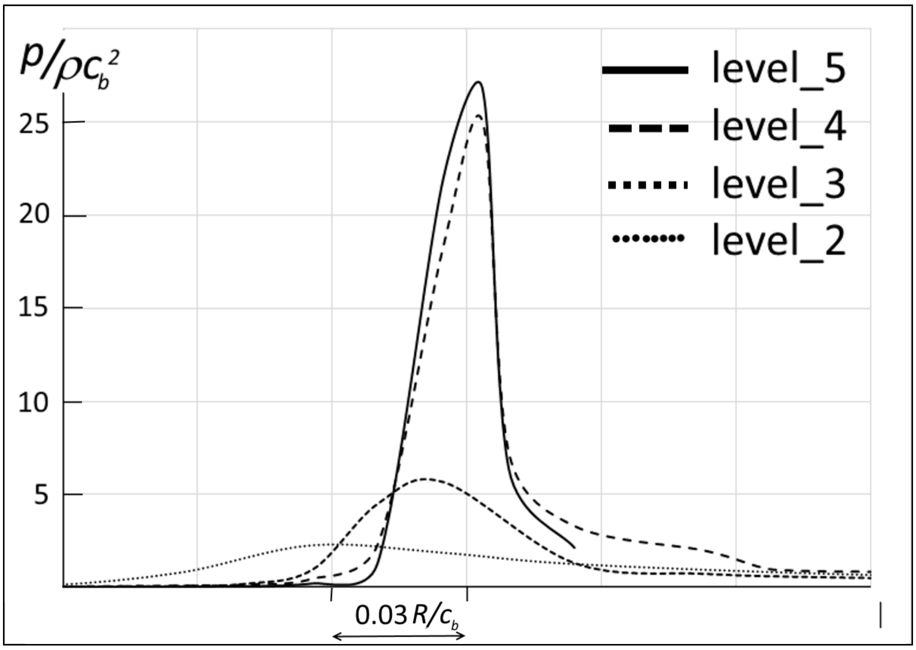

Figure 2.16 Maximum impact pressure for different levels of grid refinement

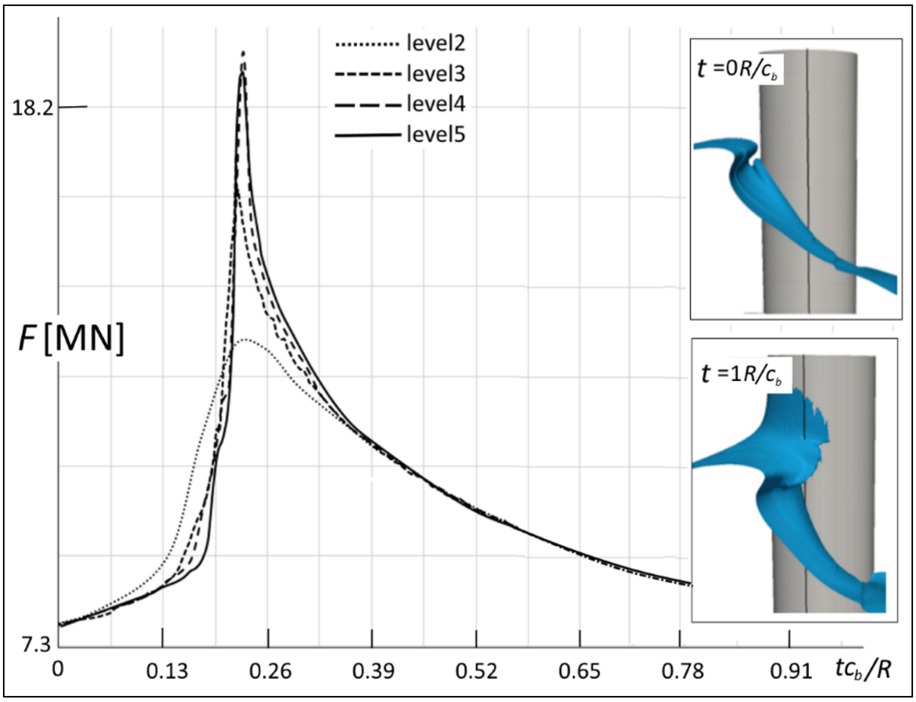

Figure 2.17 Impact force for different levels of grid refinement

The corresponding thickness of the water-air interface for the different levels of grid refinement is presented in Figure 2.18. Plotted results show that if the thickness of the air-water interface tends to zero, the solution of impact pressure stabilizes. The computed peak pressure is almost 10 times higher when the air-water interface thickness is ≈0.02R, compared to when the thickness of the air-water interface is equal to 0.3R. The effect of the thickness of the air-water interface on the magnitude of the impact force is less pronounced. The computed peak force for the air-water interface thickness 0.3R is only 1.5 times lower than that when for the thickness of air-water interface is equal 0.02R. The differences in the magnitude of the force for air-water interface thickness of 0.04R and 0.02R are very low, usually less than 5%. In order to provide adequate accuracy with an acceptable computational cost, all calculations in this thesis were conducted with an air-water interface thickness of 0.04R. This is achieved by applying the computational grid refinement level 4, which is defined by the size of the computational cells in the zone of the wave impact $dx=dy=dz\approx 0.006D$.

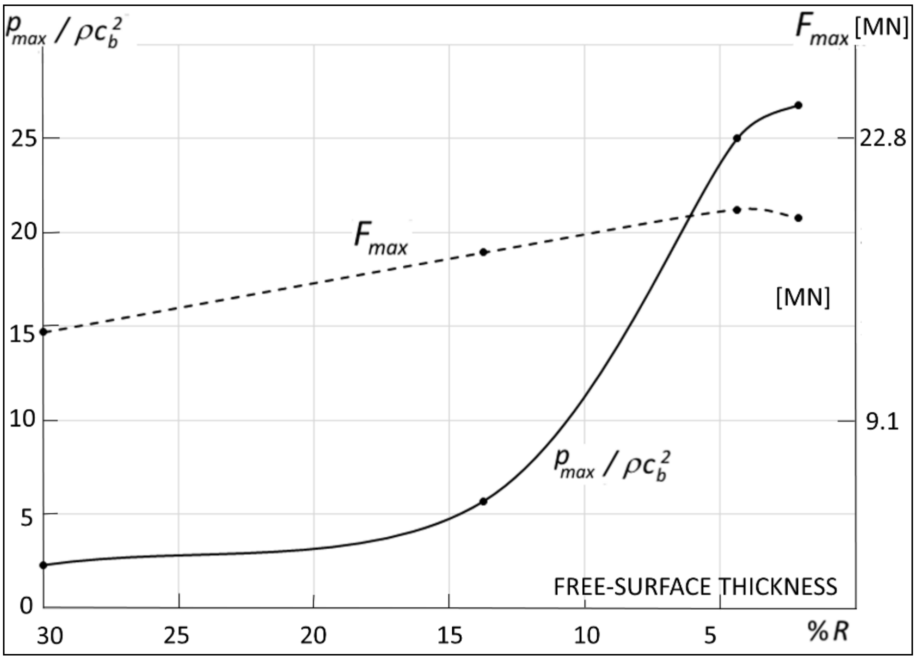

Figure 2.18 Effect the thickness of air-water interface on the impact pressure and the impact force

Because of the very fine computational grid resolution in the zone of the wave impact, the numerical simulation is very expensive, even for the decomposed numerical domain. Therefore, in order to further reduce the computational time, computations are divided into several stages. Figure 2.19 presents the computational procedure used in this study.

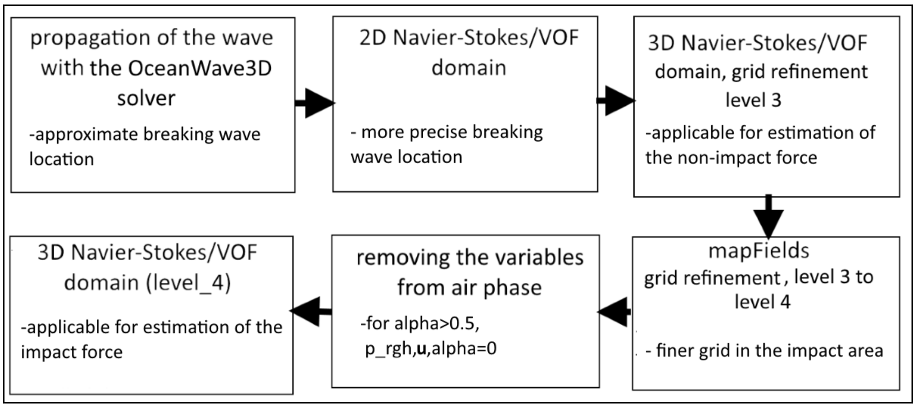

Figure 2.19 Applied computational procedure

This study includes the simulation of breaking waves characterized by wave front different steepness. The preliminary selection of the breaking wave cases and the estimation of the wave breaking location is obtained using the potential flow solver OceanWave3D. The solution of the potential flow solver is limited up to the wave breaking point. Numerical stability in the simulation is ensured by implementing an additional function to artificially reduce the energy of the waves whose vertical water particle acceleration exceeds a certain limit (Paulsen 2013) :

$$\frac{dw}{dt} < \varepsilon g \qquad ; \quad \varepsilon \in [0.4:1] \tag{2.30}$$

Activation of the aforementioned filter indicates the approximate location where the wave breaks. More precise location of the wave breaking is then estimated using the 2D coupling between the potential flow solver and NS-VOF solver. By knowing the wave breaking location, for the undisturbed wave, the position of the monopile structure with respect to the breaking wave stage can be evaluated. At first, the fully 3D simulation which includes wave interaction with the monopile structure is conducted applying the computational grid refinement level 3 (Figure 2.13). This numerical domain consists of around 3 million computational cells, and it is adequate for the estimation of the non-impact hydrodynamic loading on the monopile structure. However, the application of this domain leads to considerably underestimated impact pressures and impact force (Figure 2.16 and Figure 2.17). In order to compute the wave impact force on the monopile structure with sufficient accuracy, an additional numerical simulation is conducted, which includes finer refinement of the computational grid in the zone of the wave impact on the structure (level 4). The initial solution for this numerical simulation corresponds to the moment where the distance between the overturning wave jet and the structure is $\approx 0.2D$ (Figure 2.13). This initial solution is achieved by applying the *mapFields* function from OpenFOAM library, which allows mapping of the fields between the numerical domains with different sizes off computational grid. The application of the *mapField* function allows implementation of finer cells around the zone of the wave impact, while the cells which are not of interest can be coarsened. This procedure enables the desired level of the computational grid refinement in the zone of the wave impact, without significantly increasing the total number of the computational cells (around 3.5M in total). The average computational cost using this computational procedure is around 50h on parallel running with 20 x 2.4Ghz processors.

2.5 Numerical results - incompressible model

The vertical impact load distribution for the selected cases of breaking wave impact with different steepness of a wave front are presented. The selected cases involve plunging wave breaking with the breaking location slightly in front of the structure. In this way, the overturning wave jet hits the monopile just below the wave crest level. This is usually identified as the most violent breaking wave stage. The range of the length of the overturning wave jet analysed in this study is between l=0.19R-0.5R (Figure 2.20). The computations are conducted considering the monopile diameter D=7.2m. The depth at the monopile structure location is in the range d=d_b=17-31m.

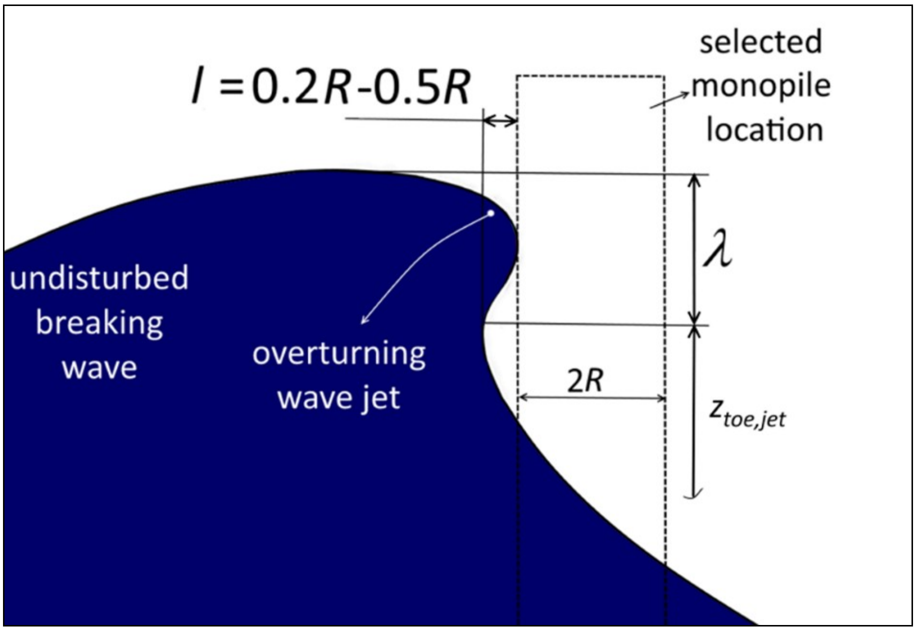

Figure 2.20 The breaking wave stage used in analysis

In order to obtain the desired breaking wave shapes, different wave generation techniques are applied including the propagation and transformation of irregular wave over a flat seabed (case 1) and over a sloped seabed m=1:20 (case 2), generation of a phase-focused breaking wave (case 3), and propagation of monochromatic waves over a sloped seabed m=1:10,1:20,1:50,1:100 (cases 4.1-4.4 and cases 5.1-5.3). Cases 1 and case 2 describe the irregular breaking wave generated by the OceanWave3D model which corresponds to the time series of the wavemaker used in laboratory experiments. In case 1, the wave breaks over the flat seabed at d_b=30m, while in case 2, the wave breaks over the sloping seabed (m=1:20) at d_b=22m (Figure 2.21).

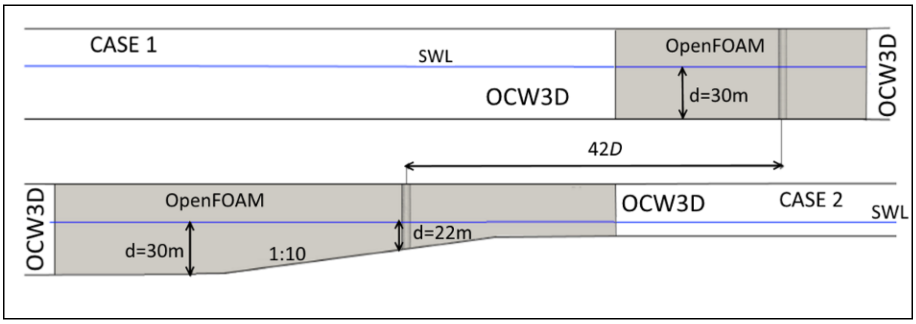

Figure 2.21 Bathymetry characteristics for case 1 and case 2

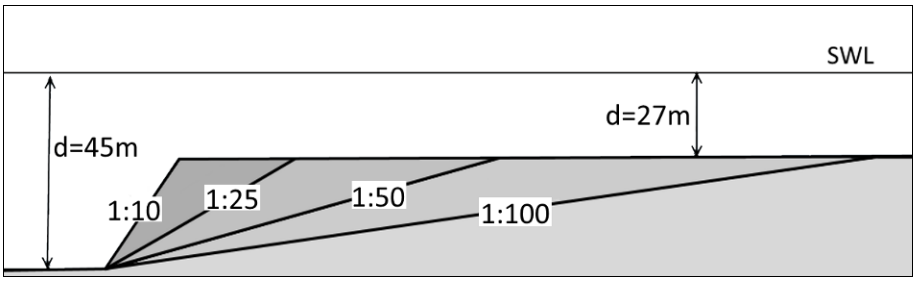

Figure 2.22 Bathymetry characteristics for cases 4.1-4.4 and cases 5.1-5.3

Case 3 describes a phase-focused breaking wave, which breaks over the flat seabed at d_b=30m. In the case of monochromatic waves, the depth at the toe of the sloping seabed is d_0=45m, while the depth at the tip of the sloping seabed is d_t=27m. (Figure 2.22). The offshore wave height corresponds to the maximum wave height obtained from experiments presented in chapter 3, H_0=H_{max}=18.5m. The chosen offshore wave period for the cases 4.1-4.4 is T_0=17s, while for the cases 5.1-5.3 is T_0=23.5s.

Table 2.2 Characteristics of the analyzed breaking waves

No.	Name	Method	*db* [m]	*ηb* [m]	*Hb* [m]	*Lb* [m]	*Tb* [s]	*Lb'* [m]	*H0* [m]	*T0* [m]	*L0* [m]
1	Case 1	Irreg. flat bottom	30.0	12.4	16.0	250	14.8	23	/	/	/
2	Case 2	Irreg. m=1/20	17.1	9.9	15.7	329	14.8	4	/	/	/
3	Case 3	Phase focused	30.0	8.1	11.0	111	7.4	5	/	/	/
4	Case 4.1	Reg. m=1/10	27.0	14.9	19.9	277	17.0	13	18.5	17.0	322
5	Case 4.2	Reg. m=1/25	28.6	16.1	21.0	302	17.0	20	18.5	17.0	322
6	Case 4.3	Reg. m=1/50	29.3	16.7	21.2	320	17.0	25	18.5	17.0	322
7	Case 4.4	Reg. m=1/100	31.3	17.0	22.0	329	17.0	34	18.5	17.0	322
8	Case 5.1	Reg. m=1/10	27.0	17.6	23.0	302	21.1	14	18.5	23.5	495
9	Case 5.2	Reg. m=1/25	27.0	18.9	23.4	329	21.1	19	18.5	23.5	495
10	Case 5.3	Reg. m=1/50	30.2	20.0	24.5	392	21.1	31	18.5	23.5	495

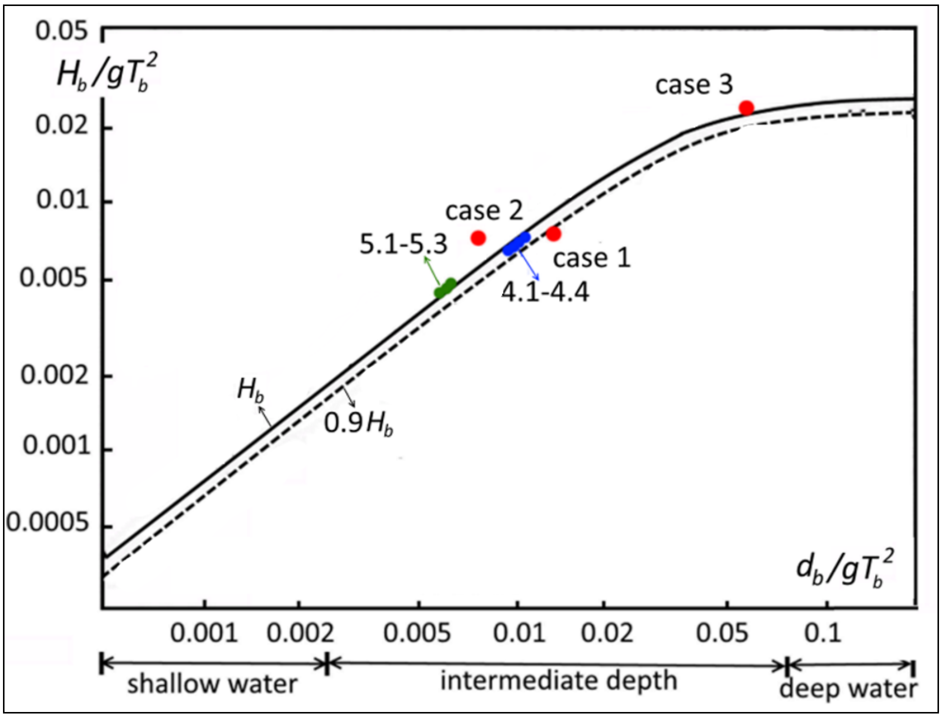

Figure 2.23 Parameters of breaking waves and breaking wave criterion applied in DNV(2014)

The main geometric characteristics of waves are presented in Table 2.**2**. Figure 2.23 shows the comparisons of the parameters of breaking waves used in the present study and breaking wave criterion applied in DNV (2014). Test case 3 refers to deep water waves, while the other cases refer to intermediate water depths.

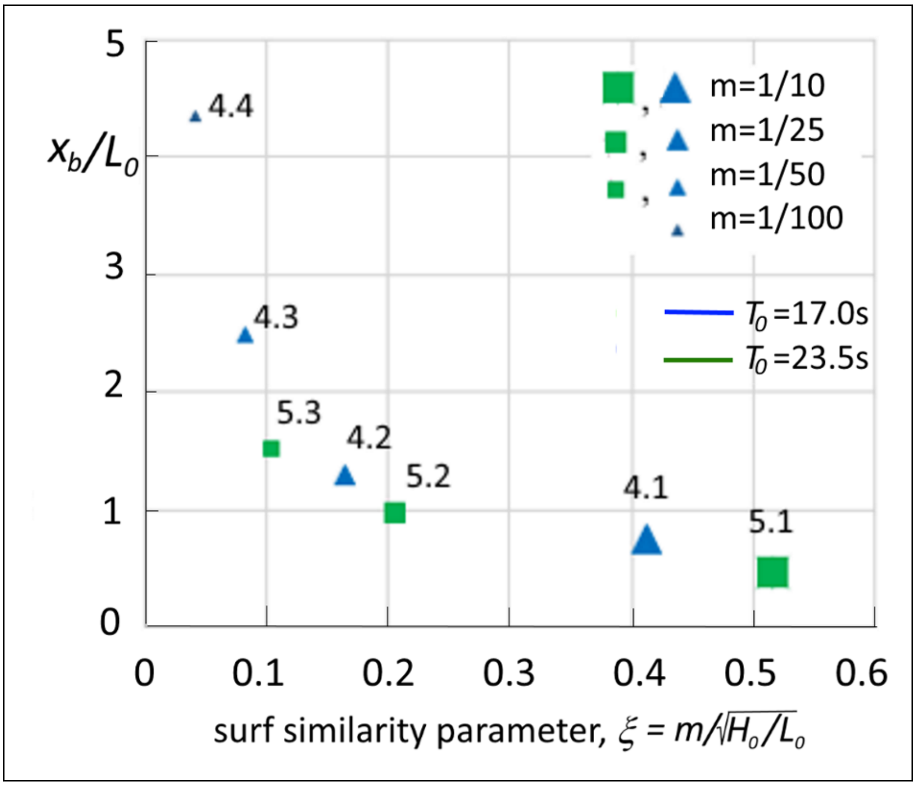

Figure 2.24 The range of the breaking wave location on the sloped seabed

Figure 2.24 shows the distance that monochromatic waves propagate from the toe of the sloped seabed to the location of wave breaking. On identical seabed slopes, the longer offshore waves propagate a shorter distance before breaking. For a less steep seabed slope, offshore waves propagate longer distance before breaking. As the steepness of the waves propagating over the slope increases, the height of the breaking wave crest decreases, while the steepness of the wave front increases (Figure 2.25). For higher of the seabed slope steepness, the breaking depth d_b is lower. In general, the breaker depth index (H_b/d_b) is higher for the higher of the seabed slope steepness (Alagan Chella, 2016), as presented in (Figure 2.26). The longer offshore waves propagating over identical seabed slopes are characterized with a higher breaker depth index. The breaker depth index is lowest in the case of the phase focused breaking wave, which represents a breaking wave in deep water.

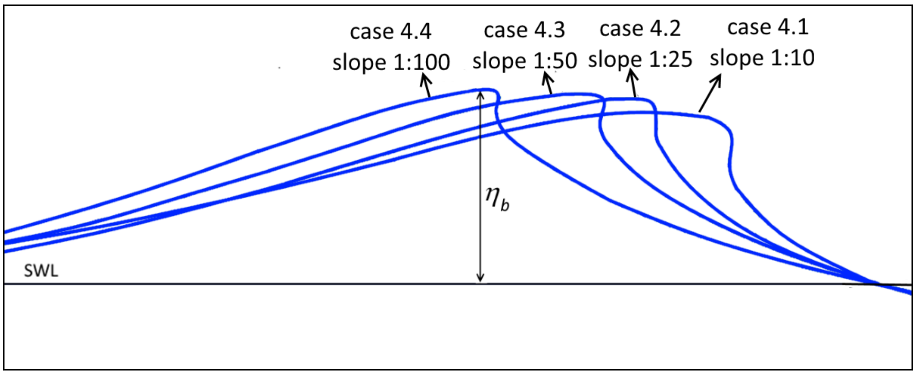

Figure 2.25 Breaking wave profile for different seabed slopes - case 4

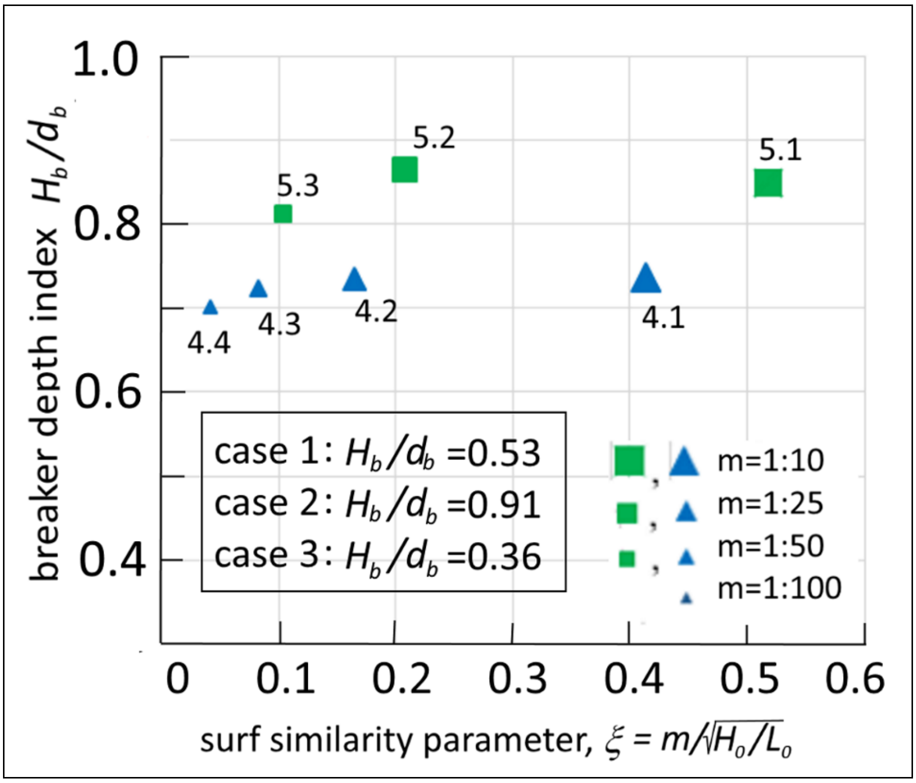

Figure 2.26 The range of the breaker depth index

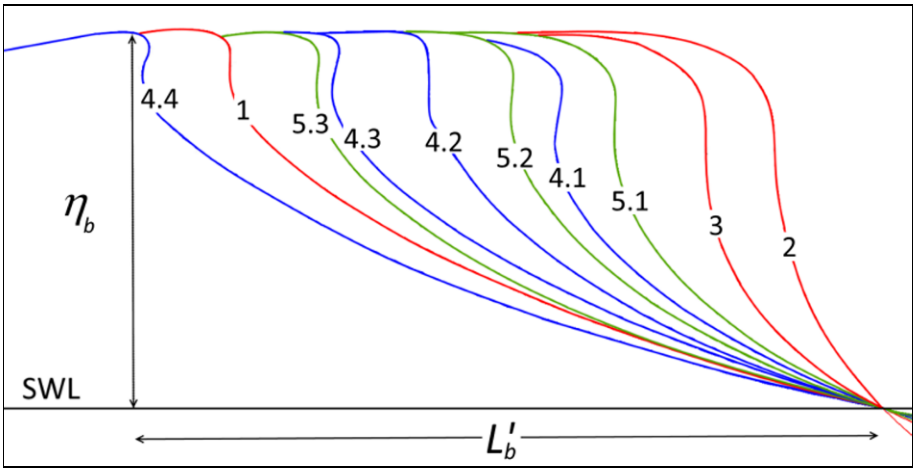

Figure 2.27 The shape of the wave fronts scaled to match identical wave crest height

The steepness of the breaking wave front is different in each analysed case. In order to show the differences between the profiles of the breaking wave front, all selected cases are scaled to match the identical crest height (Figure 2.27). The range of the wave crest front steepness parameter is presented in Figure 2.28. For the case of monochromatic waves, the parameter of the breaking wave crest front steepness is higher when wave breaks over the steeper seabed slopes. For identical slopes, the longer offshore waves have a higher breaking wave front steepness. The highest values of the crest front steepness parameter are calculated in the case of the phase-focused breaking wave and the irregular breaking wave over a sloping seabed. According the Bonmarin (1989) study, case 4.4 and case 1 relates to the weakly plunging breaker characteristics. The range of the horizontal asymmetry factor and the crest rear steepness parameter are presented in Figure 2.29 and Figure 2.30, respectively.

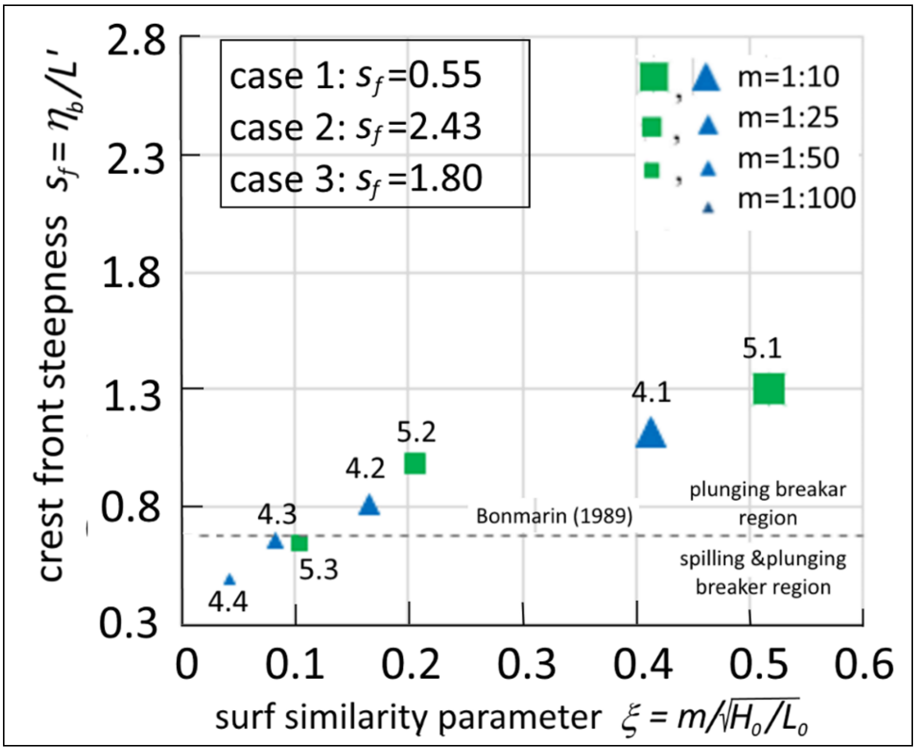

Figure 2.28 The range of the crest front steepness parameter

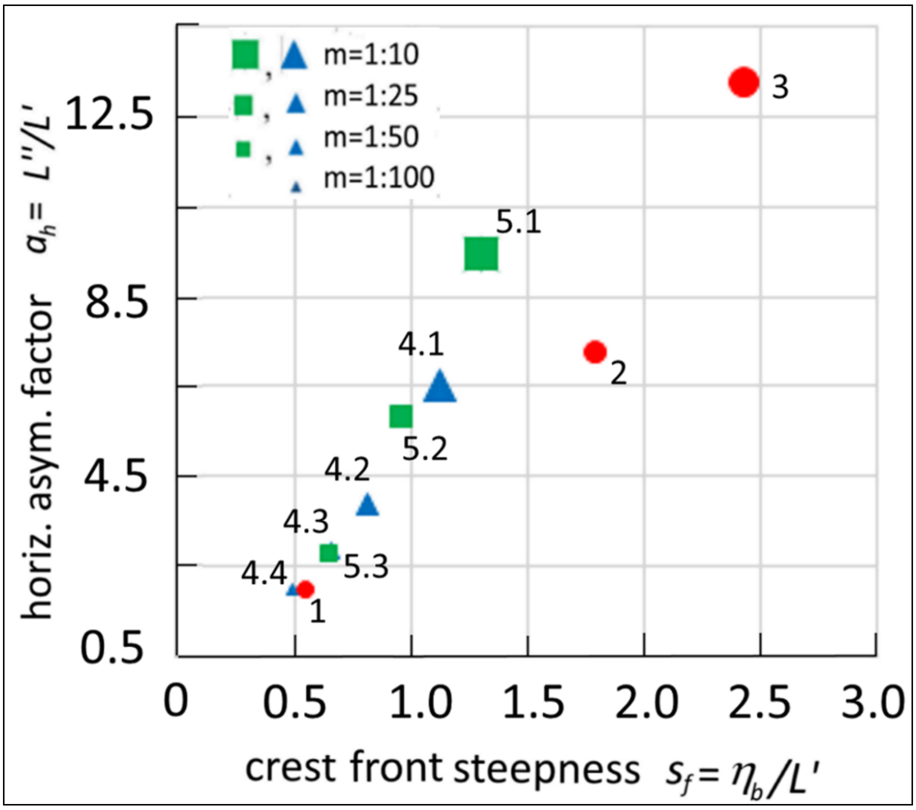

Figure 2.29 The range of the horizontal asymmetry factor

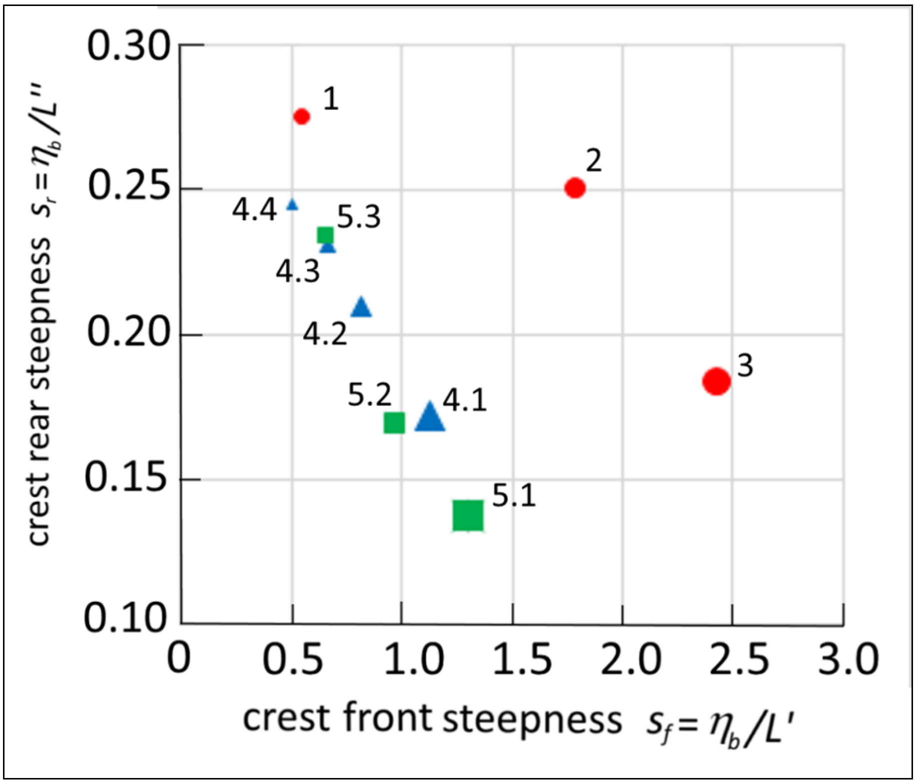

Figure 2.30 The range of the crest rear steepness parameter

The wave celerity in deep water is a function of the wave length, and the water particle velocity is proportional to the wave height. As the wave height increases the water particle velocity at the wave crest eventually exceeds the wave celerity and the wave breaks. Approaching shallow water, the wave height and the water particle velocity at the wave crest increase while the wave length and wave celerity decrease, leading to instability and wave breaking. When the water particle velocity exceeds the wave celerity, the tip of the wave crest propagates forward as an overturning jet. The horizontal water particle velocity in the overturning crest is higher than the wave celerity (Alagan Chella, 2016). As an example, Figure 2.31 and Figure 2.32 show velocity distribution under the monochromatic wave which propagates over the slope *m*=1:25 (case 4.2).

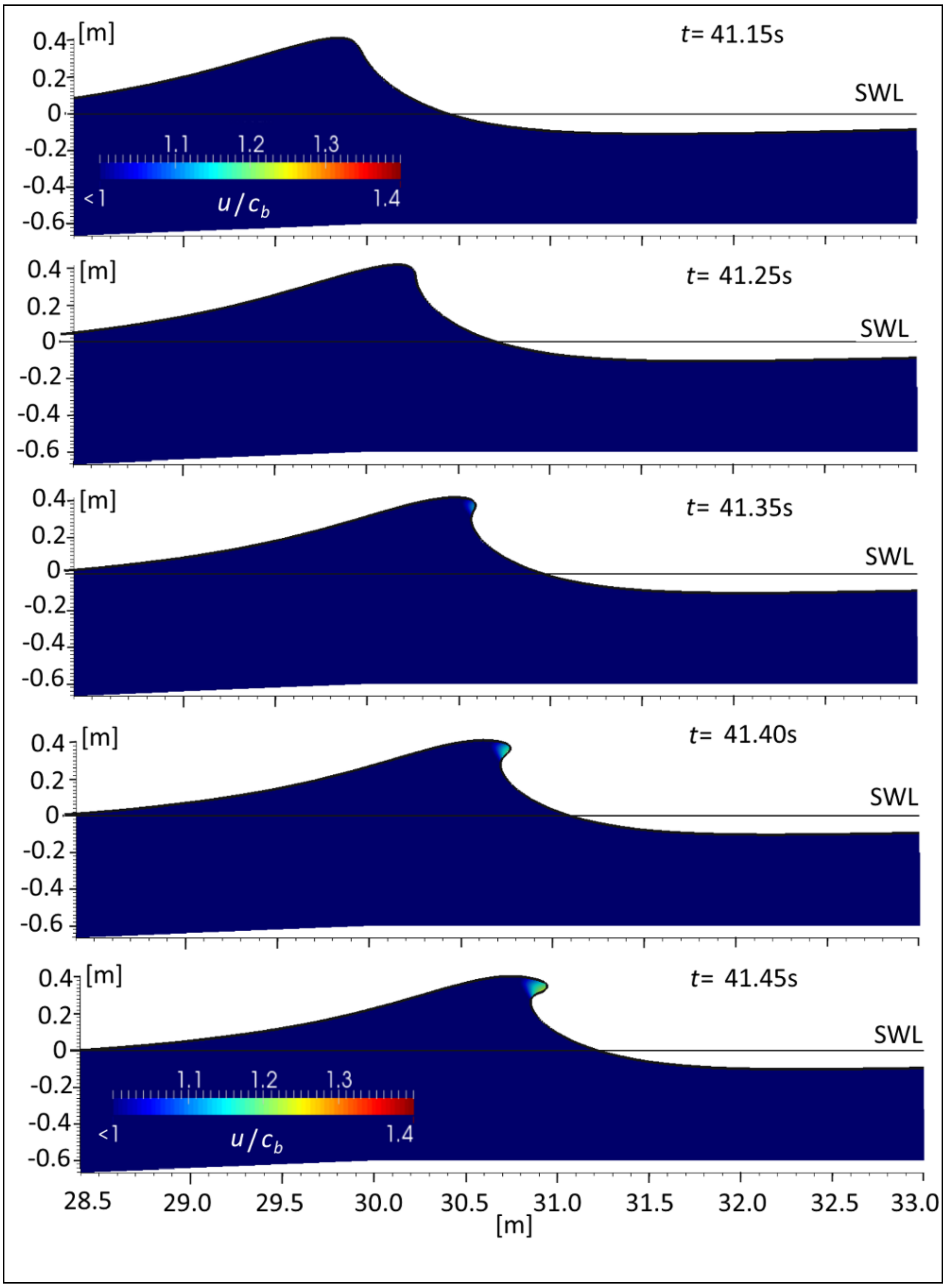

Figure 2.31 Velocity distribution under the breaking wave (case 4.2)

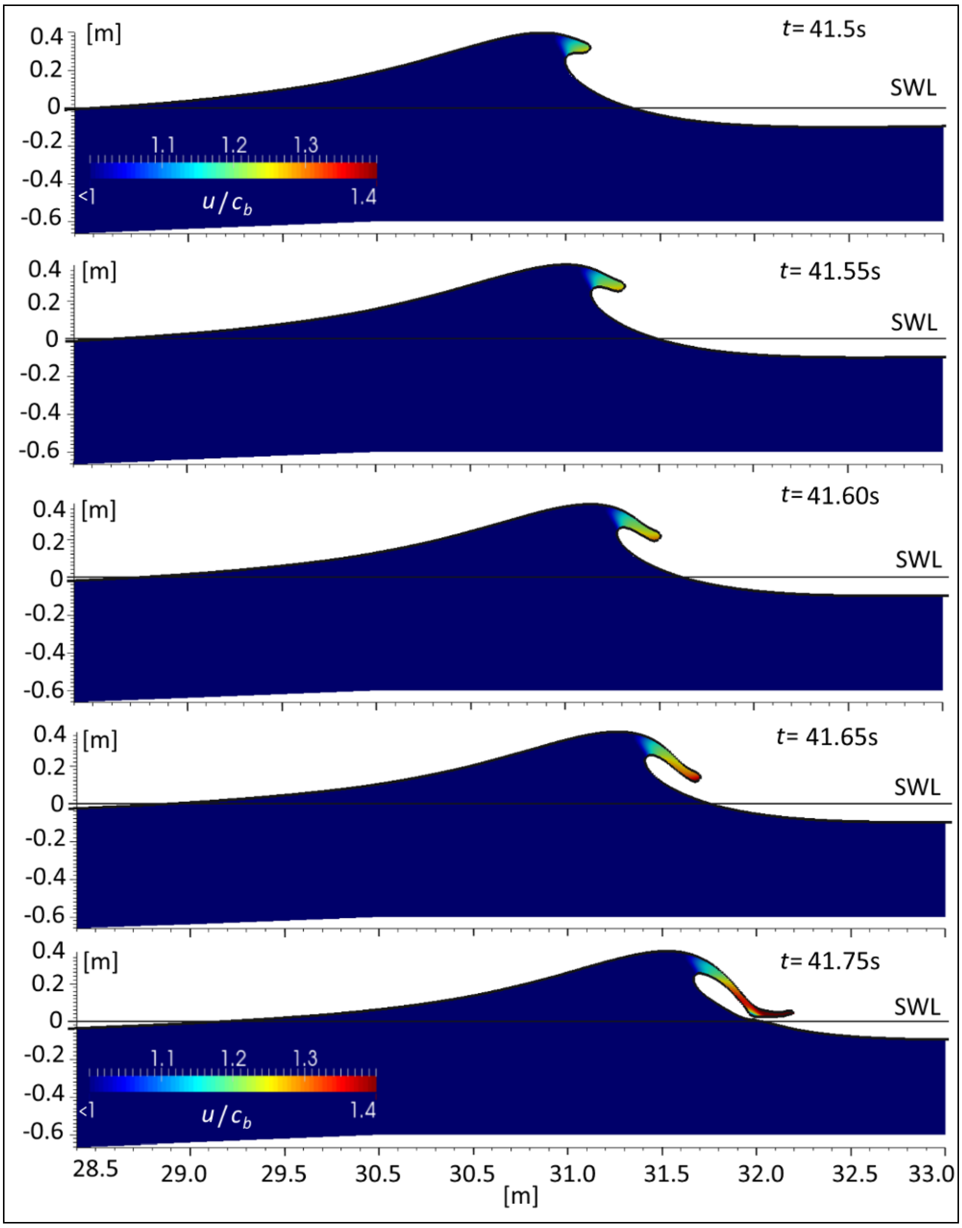

Figure 2.32 Velocity distribution under breaking wave (case 4.2)

For the purpose of this study, the breaking wave celerity, c_b, is defined as the horizontal water particle velocity at the toe of the overturning wave jet, while the curling factor, λ, is estimated as the distance from the toe of the overturning wave jet to the wave crest height (Figure 2.33). Table 2.3 shows values of the estimated breaking wave celerity, the curling factor, and the length of the overturning wave jet for all the selected cases.

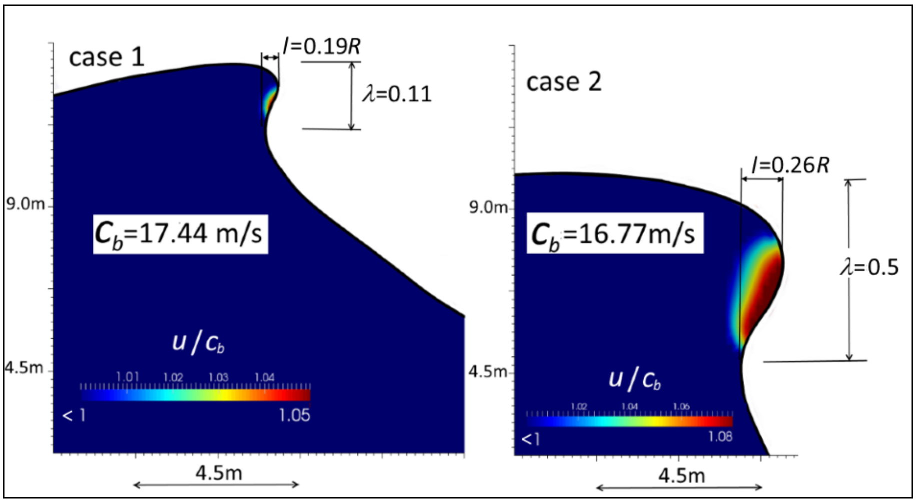

Figure 2.33 Evaluation of the l, c_b and λ

Table 2.3 Estimated values of the breaking wave parameters l, c_b and λ

No.	Name	Method	*cb* [m/s]	*l/R*	λ
1	Case 1	Irreg. flat	17.4	0.19	0.13
2	Case 2	Irreg. m=1/10	16.8	0.26	0.55
3	Case 3	Phase focused	14.4	0.20	0.45
4	Case 4.1	Reg. m=1/10	20.1	0.31	0.39
5	Case 4.2	Reg. m=1/25	20.5	0.25	0.19
6	Case 4.3	Reg. m=1/50	20.8	0.28	0.15
7	Case 4.4	Reg. m=1/100	21.2	0.19	0.11
8	Case 5.1	Reg. m=1/10	20.8	0.44	0.46
9	Case 5.2	Reg. m=1/25	22.1	0.25	0.27
10	Case 5.3	Reg. m=1/50	22.8	0.23	0.18

2.5.1 The non-impact force

The hydrodynamic loading from breaking waves can be decomposed into non-impact and impact parts of the total force. The non-impact part of the total force in this study is calculated by applying the Morison's equation and the Rainey's extension (section 2.2). For the estimation of the fluid velocity and acceleration, two approaches are used. In the first approach, the wave kinematics are estimated according to the stream function wave theory, which describes the non-linear symmetric waves up to the limit of H=0.9H_{b}. In the second approach, the breaking wave is simulated by applying 2D NS-VOF model. The wave velocity and the acceleration field from the numerical model are taken at a position before the wave reaches the breaking limit.

Figure 2.34 shows comparison between the numerically computed wave elevation and the wave elevation calculated according to the stream function wave theory. Highly asymmetric wave profiles, characterized by the very steep wave front are not adequately approximated by the stream function wave theory. For the breaking wave cases, which are characterized by the low steepness of the breaking wave front, the Morison's force is calculated by applying the stream function wave kinematics, and this provides relatively good approximation of the non-impact force (Figure 2.35). As the steepness of the breaking wave front increases, the Morison's force calculated by applying the stream function wave kinematics is not appropriate for approximation of the non-impact force. However, the Morison's force based on the wave kinematics from the NS-VOF model, approximates the computed non-impact force fairly well.

In order to obtain the material acceleration du/dt and the vertical velocity gradient dw/dz required for application of the Morison's equation, the OpenFOAM top level solver waveFoam is supported with additional code lines in UcreateFields.H and interFoam.C files. This additional code lines are presented in Appendix I.

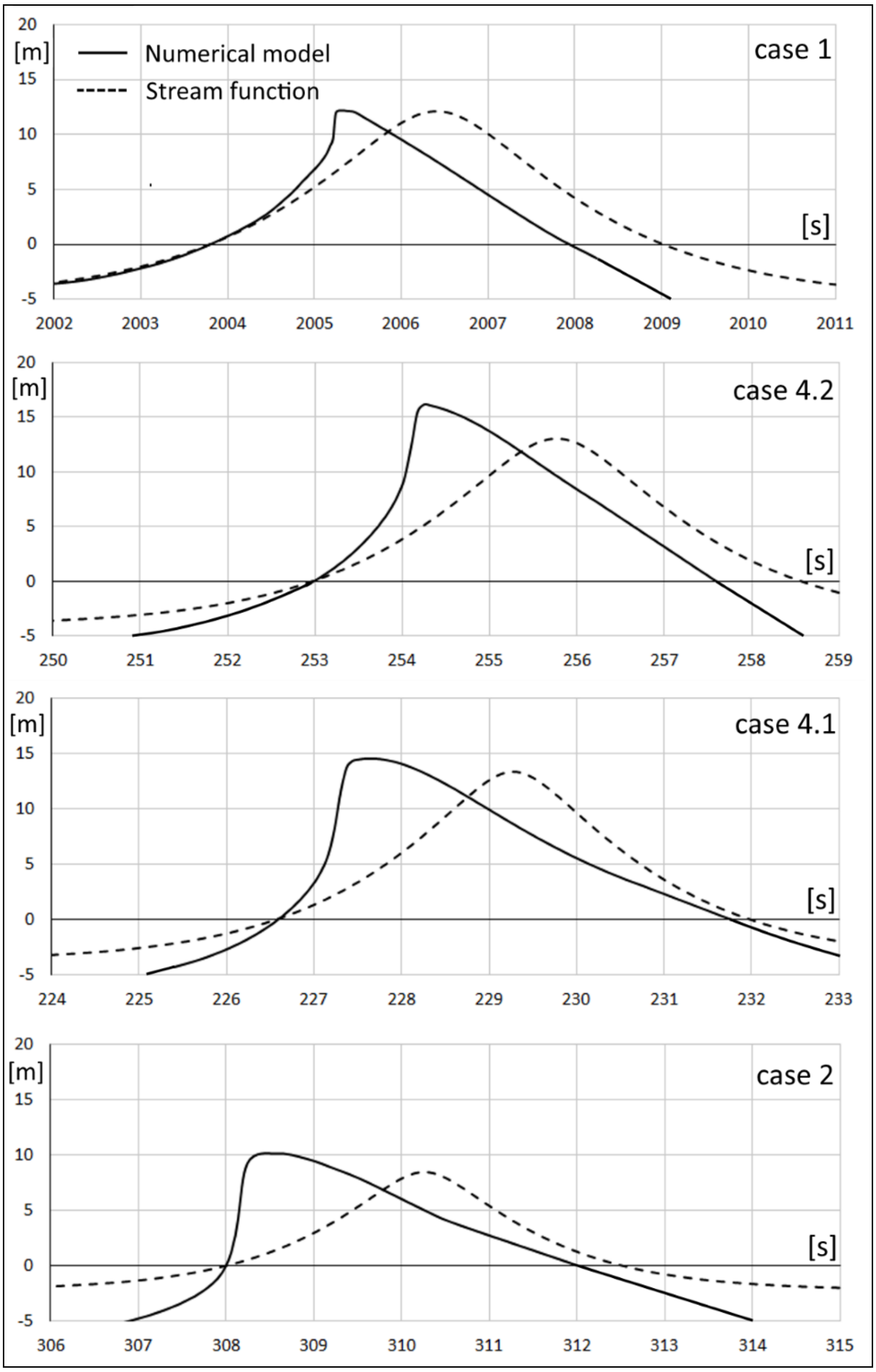

Figure 2.34 Comparison between the computed wave stream function wave elevation

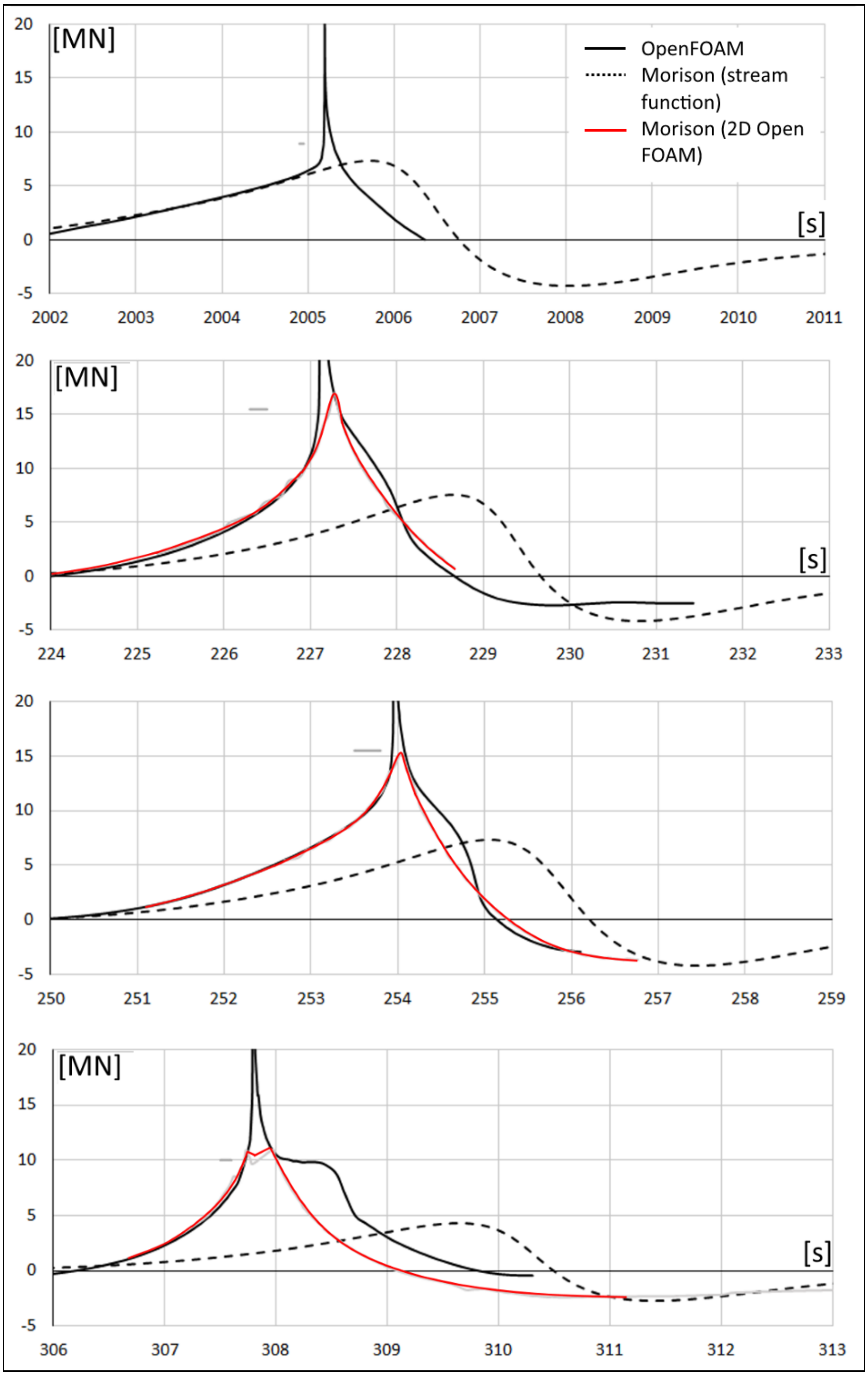

Figure 2.35 Comparison between the computed inline force and the Morison's force

2.5.2 The impact force

This section presents the comparison between the impact forces obtained by applying the derived model and the results of simplified approaches applied in engineering practice. Numerical results for case 4.4 show that the presence of the wave run-up considerably interfere with the interaction between the overturning wave jet and the monopile structure. Figure 2.36 shows that the impact force on the structure is damped and, consequently, reduced by the interaction between the overturning wave jet and the wave run-up jet. Because the results of case 4.4 are not adequate for a direct comparison with the results from the model, the case 4.4 is omitted in the diagrams.

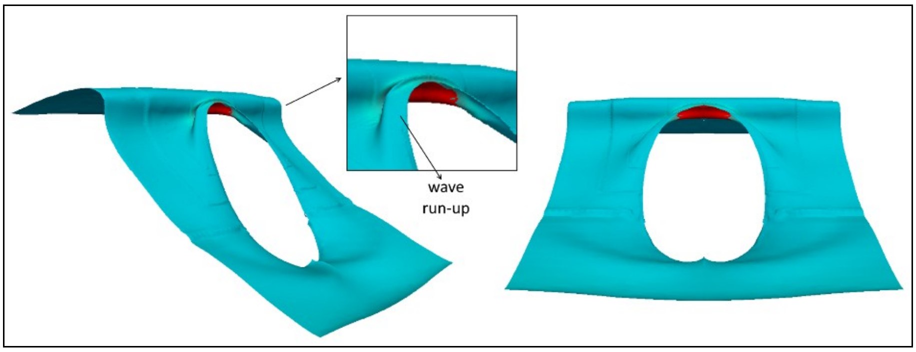

Figure 2.36 Interference between the wave run-up and overturning wave jet for case 4.4

It is estimated that the impact force on a monopile structure occurs when dynamic pressure on the surface of the structure exceeds $p>0.5\rho c_b^2$. Figure 2.37 presents plots of the impact forces F_i for all the selected cases. The force is normalized by $F_i(t)/\rho R c_b^2 \lambda \eta_b$ and is shown in terms of the slamming coefficient C_{sr} (t). The values of the peak slamming coefficient are quite scattered, ranging from C_{sr}=0.9π (case 2) to C_{sr} =2.1π (case 1). Figure 2.37 also shows the comparison between the computed slamming coefficient $C_{sr}(t)$ and a corresponding slamming coefficient obtained by applying a simplified approach (Wienke, 2001). The peak of the slamming coefficient in Figure 2.37 corresponds to t=0 s. The time t<0 s refers to the rising impact force phase which cannot be derived from a simplified approach suggested by Wienke (2001), while the time t>0 s refers to the decaying impact force phase. For the time interval $0<t<0.12R/c_b$ the computed force decays much faster than forces derived from a Wienke approximation. Figure 2.38 shows the value of the computed slamming coefficient C_{sr} as a function of the crest front steepness parameter s_f. The results show that the value of the slamming coefficient C_{sr} is inversely proportional to the steepness of the breaking wave front s_f.

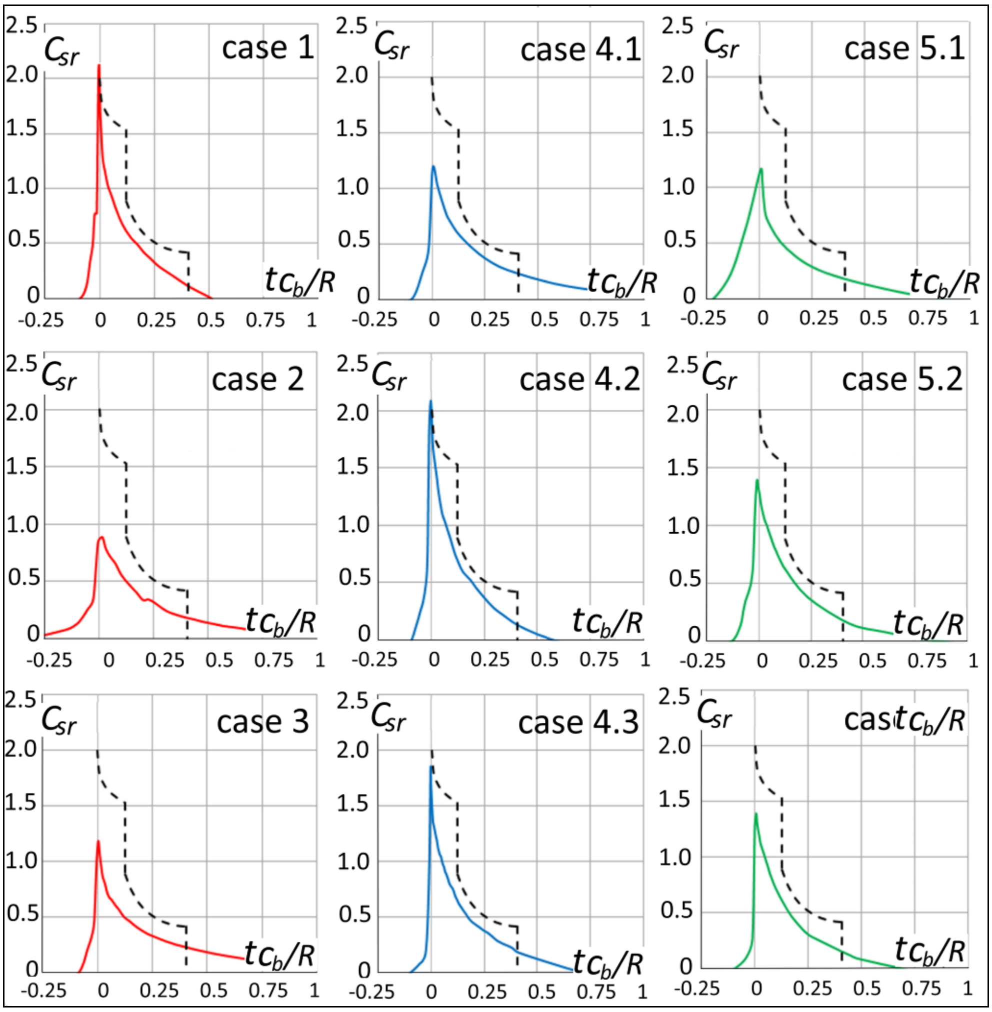

Figure 2.37 Slamming coefficients derived from the present model and corresponding results obtained by applying Wienke (2001) approximation ---

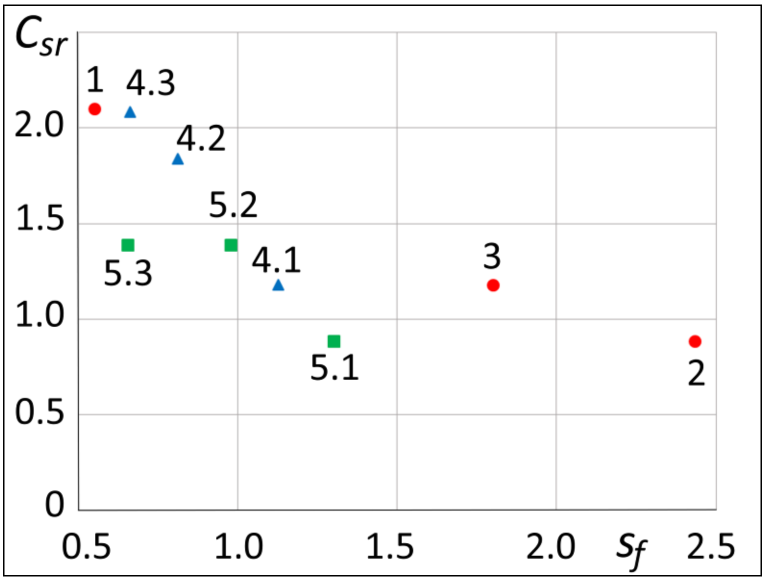

Figure 2.38 Dependency between the slamming coefficient C_{sr} and the crest front steepness parameter s_f

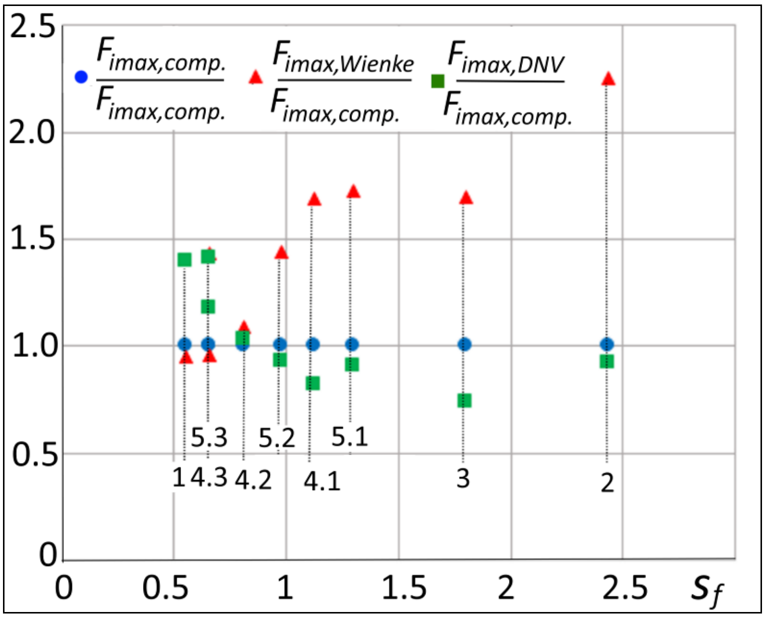

Figure 2.39 Computed impact forces and corresponding results obtained by applying simplified approaches Wienke (2001) ▲ and DNV (2010, 2014) ■

Figure 2.39 shows the computed peak impact forces and the corresponding results obtained by applying simplified approaches. The slamming coefficient is considered to be $C_{sr}=2\pi$ for both simplified approaches. For breaking waves characterized with crest front steepness parameter $s_f<0.8$, the impact forces calculated according to DNV (2014) standard are higher than results of the applied numerical model, while the impact forces calculated according to Wienke's simplified approach are similar to the results of the applied numerical model. For breaking waves characterized with the crest front steepness parameter $s_f>0.8$, the impact forces calculated according to DNV (2014) standard are lower than results of the applied numerical model, while the impact forces calculated according to Wienke simplified approach are significantly higher than the results of the applied numerical model.

The presented results show that the application of the simplified approaches for the calculation of the impact forces on the cylindrical structures, which are based on rectangular load distribution, provide unreliable results. This is because the impact load distribution strongly depends on the breaking wave shape and it is difficult to uniquely approximate such a complex load distribution by a rectangle. In order to increase the knowledge on breaking wave impact, a study on the 3-D pressure distribution during wave impact is essential.

2.5.3 Temporal and spatial impact pressure distribution

The pressure data is collected for every 10th time-step during the numerical computation, which relates to the pressure sampling rate in range of 10kHz-25kHz. The highest magnitude of the computed impact pressures is in the range $p_{max}\approx 13\text{-}28\rho c_b^2$, while the rising time of the pressures is $t_{pi}\approx 0.025R/c_b$. These values are very similar to the laboratory measurements conducted by Zhou et al. (1991) and Chan et al. (1995), presented in Appendix II. Figure 2.40 shows the pressure distribution on the monopile structure for the moment of the highest impact pressure on the structure. Results show that the location of the highest impact pressure on the structure occurs in the region below the overturning wave jet. Figure 2.41 presents the shape of the breaking wave profile for the case 4.1 and the pressure distribution at the front line of the monopile structure at the moment of the highest impact pressure. It is observed that the peak of the impact pressure occurs in the region where the overturning wave jet meets the wave run-up on the structure. It is also observed that the impact pressures rapidly decay from the peak value. These observations are equivalent for all analysed cases.

Figure 2.42 shows the pressure distribution on the monopile structure for different moments during the wave impact (case 4.1). The cross-section A-A relates to the vertical location of the highest impact pressure. The temporal impact pressure distribution around the structure at the vertical cross-section A-A is presented in Figure 2.43 and Figure 2.44.

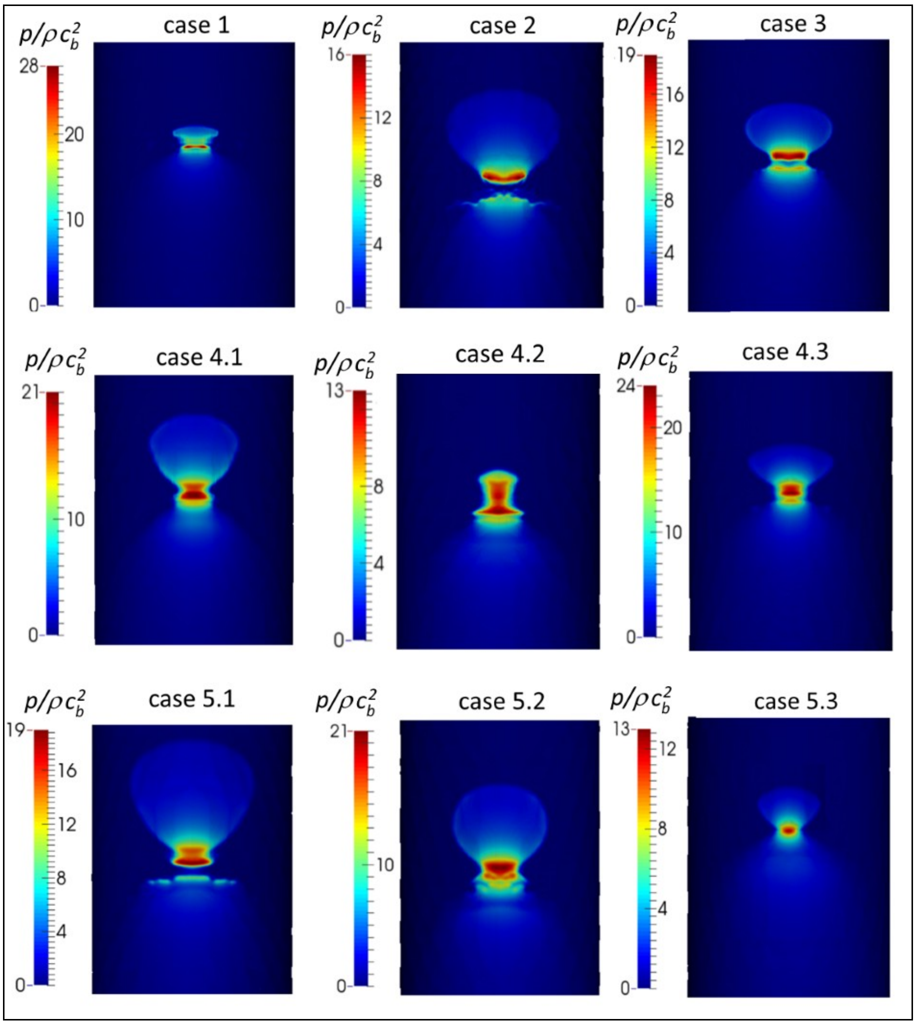

Figure 2.40 Distribution of the highest impact pressure - front view

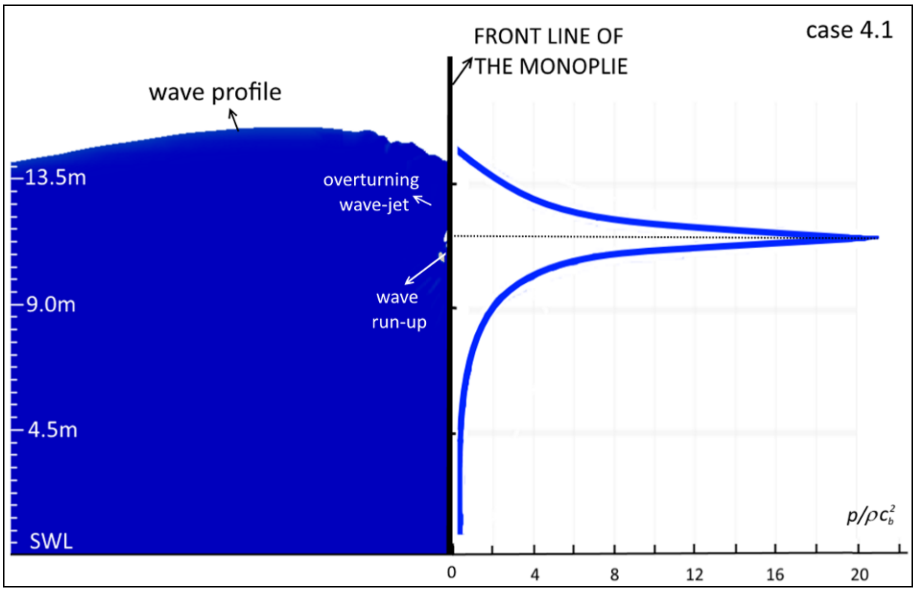

Figure 2.41 Wave profile and vertical distribution of the highest impact pressure - case 4.1

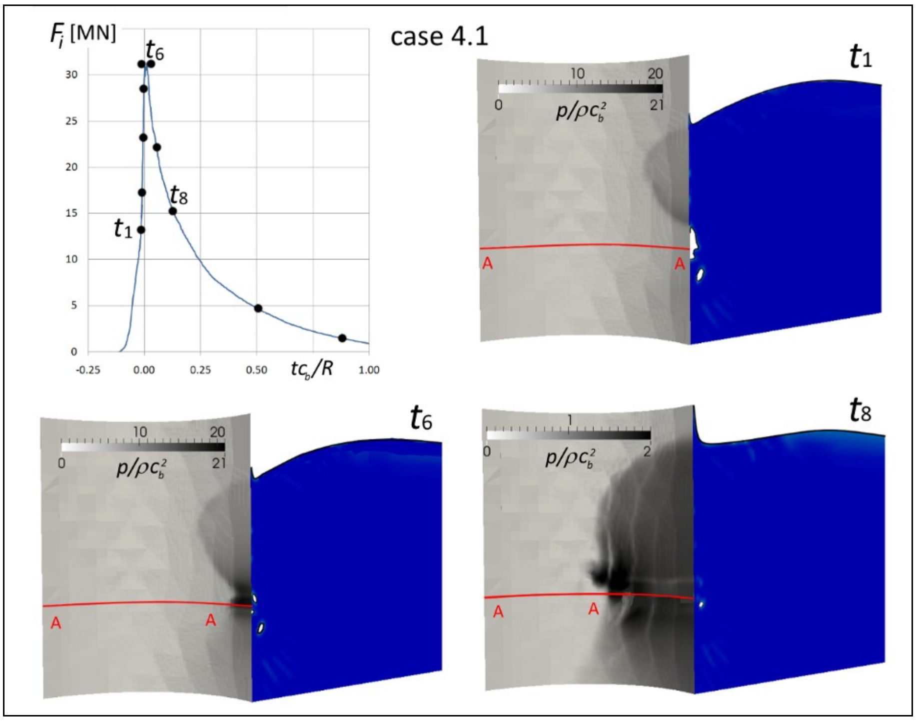

Figure 2.42 Wave profile, impact force and the impact pressure distribution for different moments of the wave impact - case 4.1

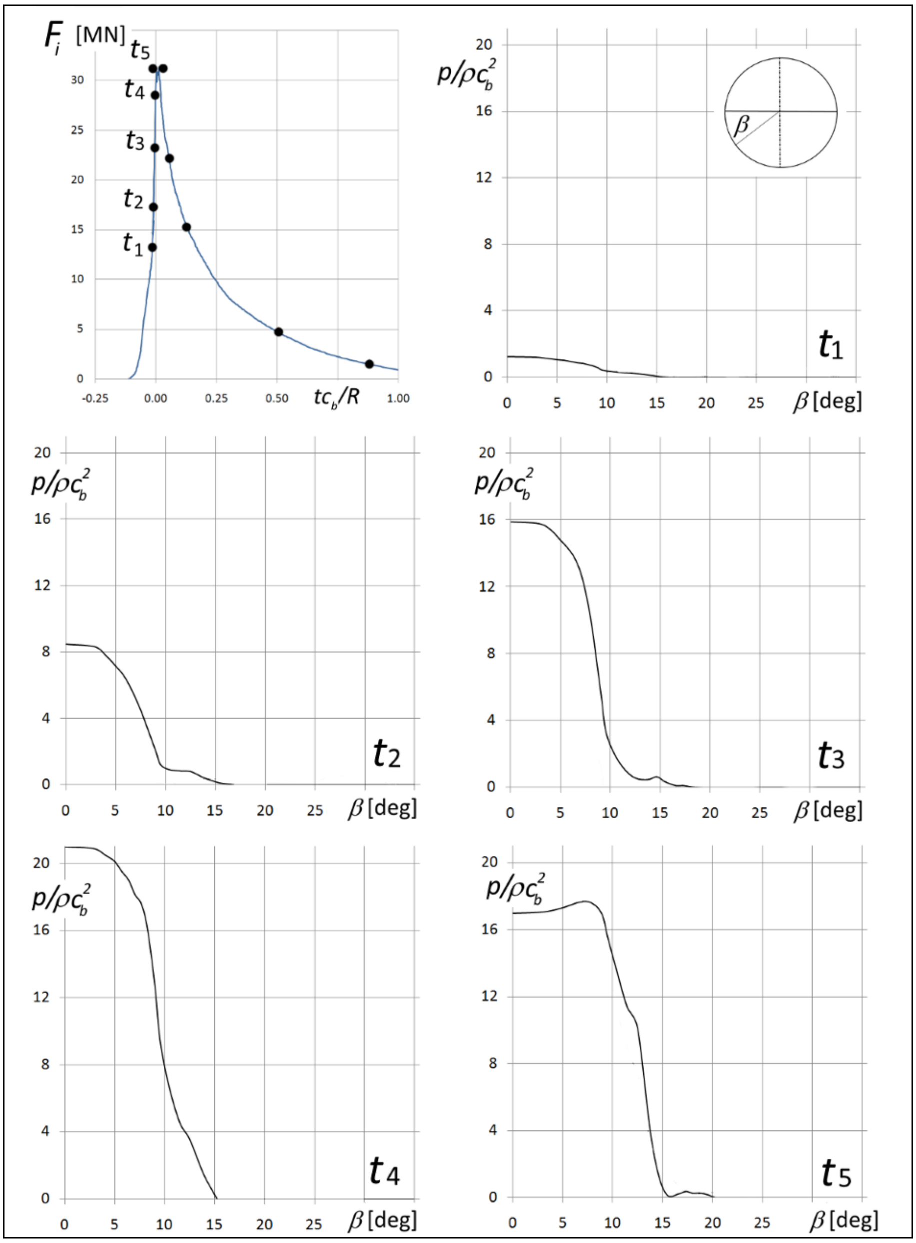

Figure 2.43 Pressure distribution around the span of the monopile at the cross-section A-A, case 4.1

The beginning of the wave impact on the structure at the vertical section A-A corresponds to time t_1. The wave impact loading on the structure before time t_1 relates to the interaction between the overturning wave jet and the structure. The maximum impact pressure, $p_{max} \approx 21\rho c_b^2$, occurs at the moment t_4. The time lag between the t_1 and t_4 represents the rising phase of the impact pressure, t_{pi}=0.015R/c_b.

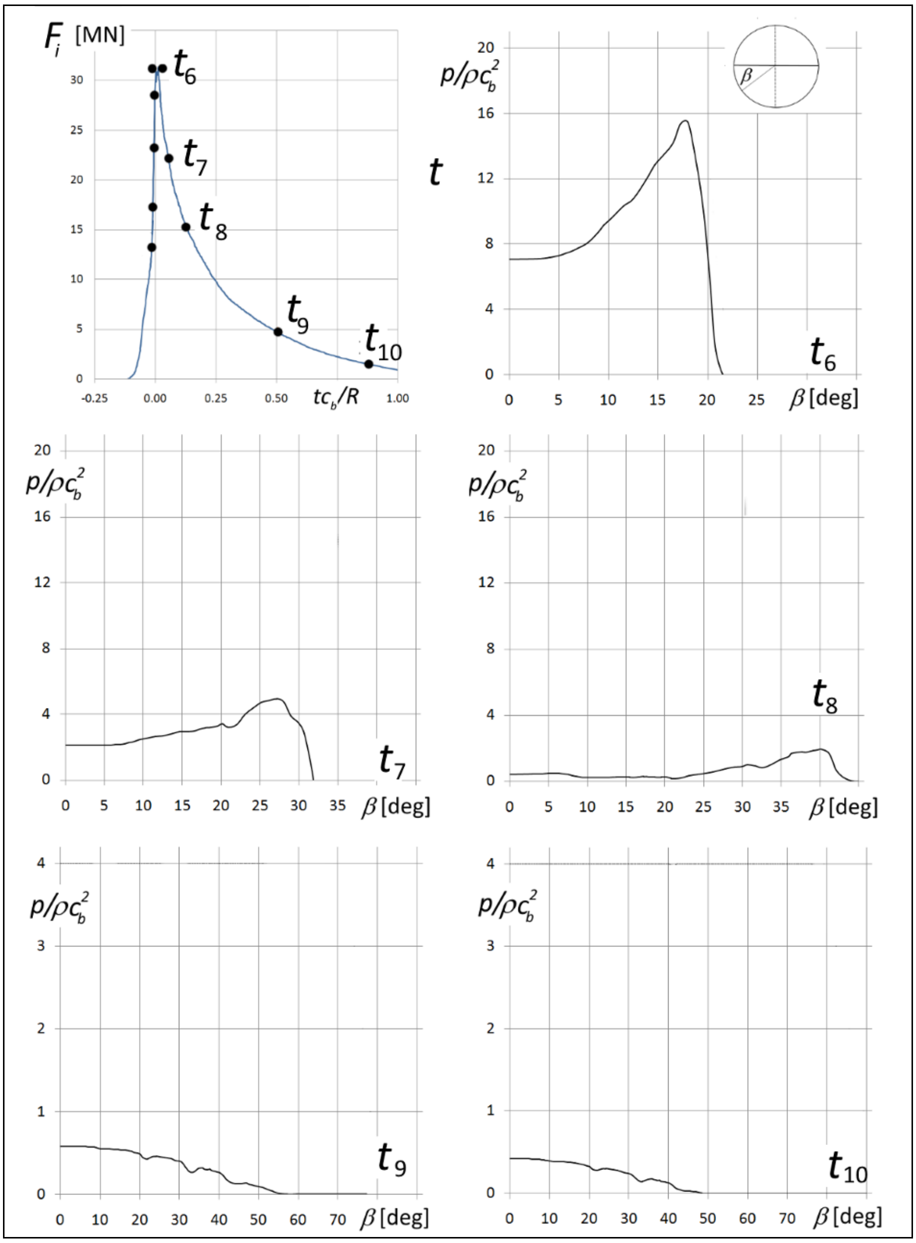

Figure 2.44 Pressure distribution around the span of the monopile at cross-section A-A, case 4.1

During the impact pressure rising phase, the breaking wave propagates up to the monopile azimuth angle $\beta \approx 15^{\circ}$. The maximum wave impact loading on the structure corresponds to the moment t_6, which relates to the higher impact area on the structure. At this moment, the breaking wave propagates up to the monopile azimuth angle $\beta \approx 20^{\circ}$. At the moment t_6, the impact pressure at the front line of the structure is in the decay stage, $p \approx 7\rho c_b^2$, while the peak impact pressure which occurs at the azimuth angle $\beta \approx 18^{\circ}$ is $p \approx 16 \rho c_b^2$. When the wave propagates up to $\beta \approx 30^{\circ}$, the impact pressure at the front line of the monopile is $p \approx 2 \rho c_b^2$. Between the moment t_9 and t_{10}, the impact pressures around the structure fall below the value $p \approx 0.5 \rho c_b^2$. This moment can be characterized as the end of the breaking wave impact on the structure.

Figure 2.45 and Figure 2.46 present fully 3D impact pressure distribution on the monopile support structure for different moments of the wave impact, for case 1 and case 2, respectively. The snapshots marked with a) refers to the initial stage of the wave impact. The initial stage of impact for case 1 is the result of the interaction between the breaking wave tongue and the wave run-up on the structure. The observed peak pressure is in the range of $2 \rho c_b^2$. The initial stage of impact for case 2 is the result of the interaction between the breaking wave tongue and the structure. The observed peak pressure is in the range of $5 \rho c_b^2$.

The snapshots marked with c) and b) present the beginning of the interaction between the breaking wave tongue and the structure, for case 1 and case 2, respectively. The observed peak pressure for this stage of the wave impact is in the range of $5 \rho c_b^2$. The presented snapshots d) corresponds to the moment of the highest impact force. Presented snapshots clearly show that the region of highest impact pressures on the structure occurs below the overturning wave jet, in area where the overturning wave jet meets the wave run-up.

As breaking wave propagates, the wave interacts with the structure at higher azimuth angles and the area of the impact is larger, as seen in snapshots e) and f). The peak pressure is located at the azimuth angle which corresponds to the location of the propagating overturning wave jet. For the same moment of the wave impact, the pressures at the lower azimuth angles of the monopile structure are in decay stage.

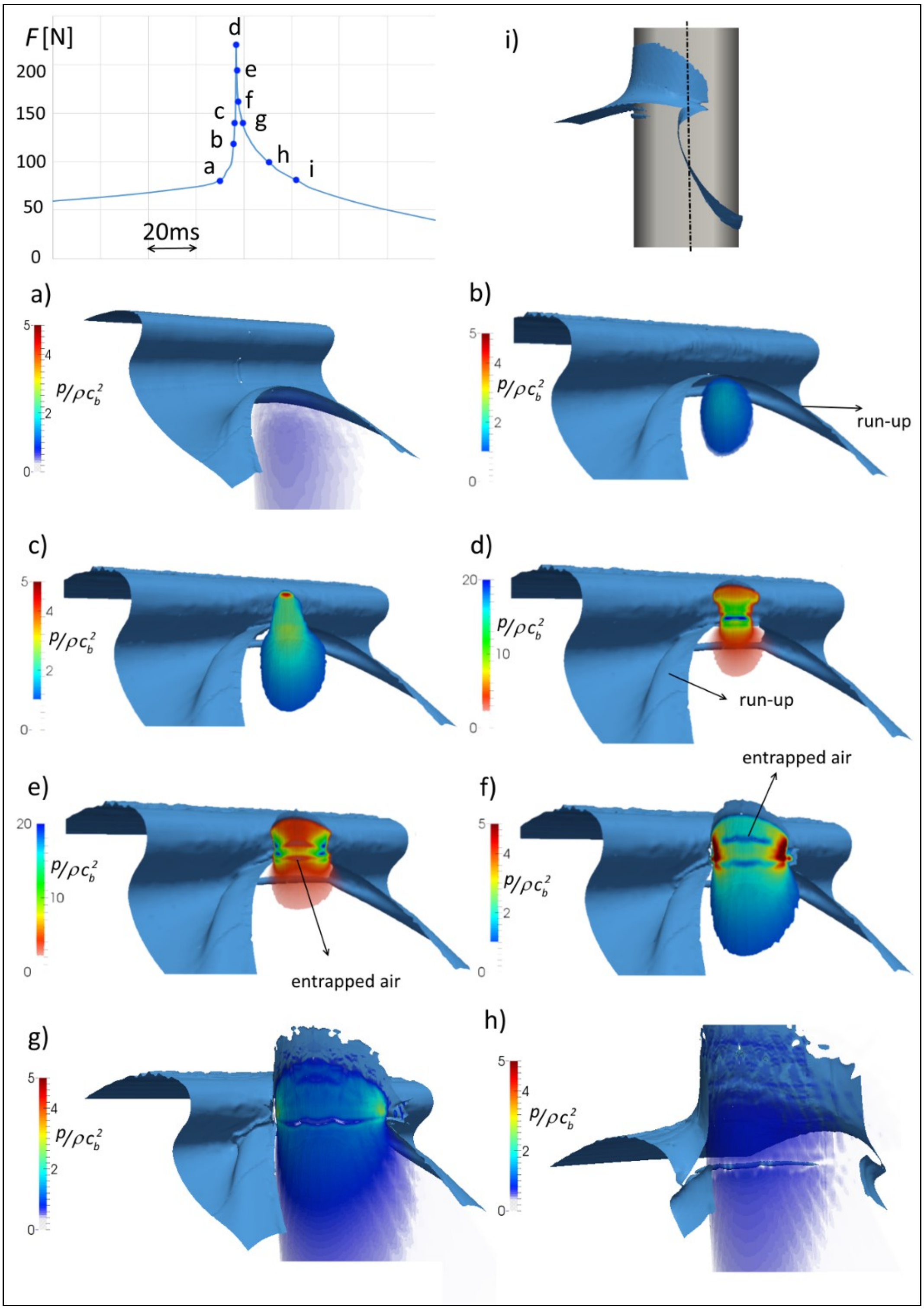

Figure 2.45 Temporal impact pressure distribution for the case 1

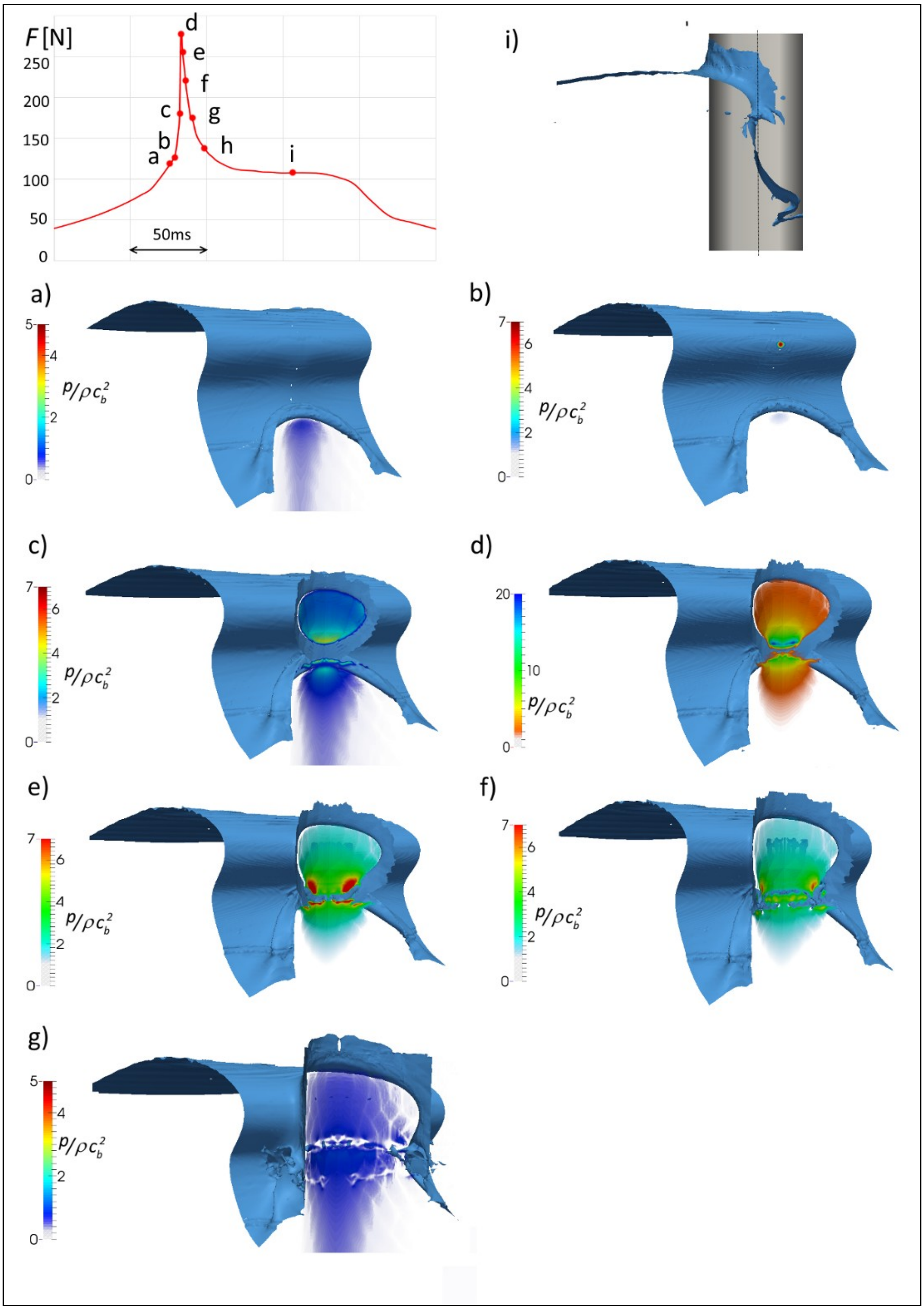

Figure 2.46 Temporal impact pressure distribution for the case 2

In order to better understand the characteristics of the impact pressure distribution on the monopile structure, the velocity distribution below the overturning wave jet during the wave impact is investigated. Figure 2.47 shows velocity distribution under the overturning wave crest for case 3, which relates to the moment before the overturning jet hits the structure. The breaking wave celerity is c_b≈14.4 m/s. The vertical velocity of the wave run-up on the structure at the moment before the overturning wave jet hits the structure is w_{run_up}≈25 m/s.

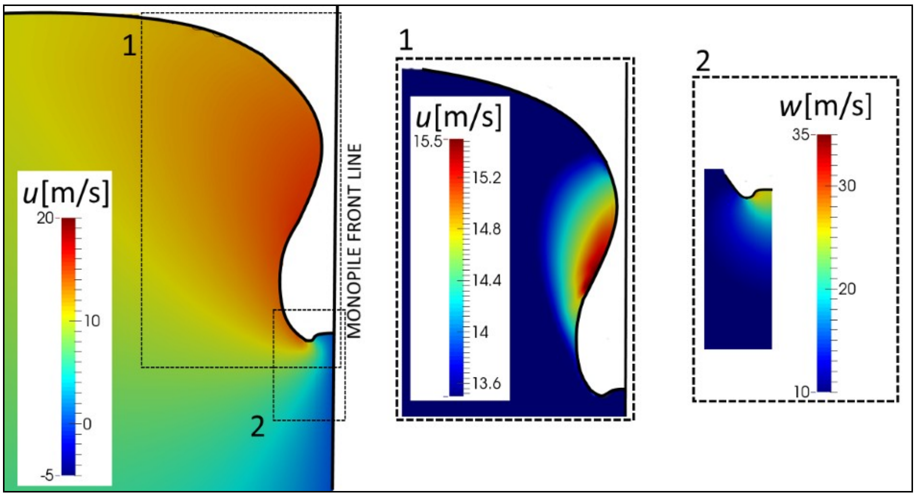

Figure 2.47 Velocity distribution under the overturning wave crest - case 3

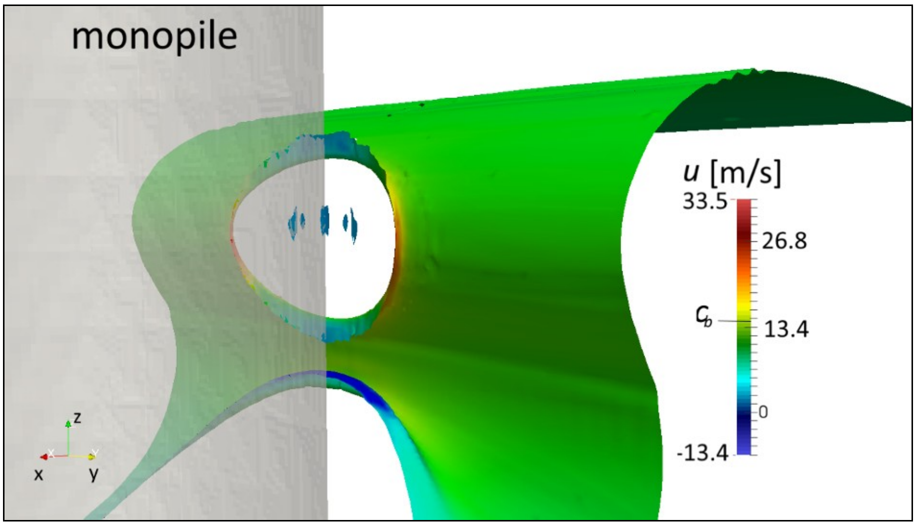

Figure 2.48 Wave splash on the monopile structure - case 3

When the overturning breaking wave jet hits the structure, the energy in the wave impact is dissipated by the generation of wave jets in all directions. This phenomenon is usually described as the breaking wave splash (Figure 2.48). Figure 2.49 presents the moment of the breaking wave impact on the structure which occurs $0.011R/c_b$ after the beginning of the overturning wave jet interaction with the structure. Figure presents the horizontal velocity distribution under the overturning wave jet, and impact pressure distribution on the monopile structure. In the area where the overturning wave jet hits the structure, the horizontal water particle velocities decrease instantly, which results in a high impact pressure on the structure. The peak impact pressure on the structure during this stage of the wave impact is $p_{max} \approx 6\rho c_b^2$.

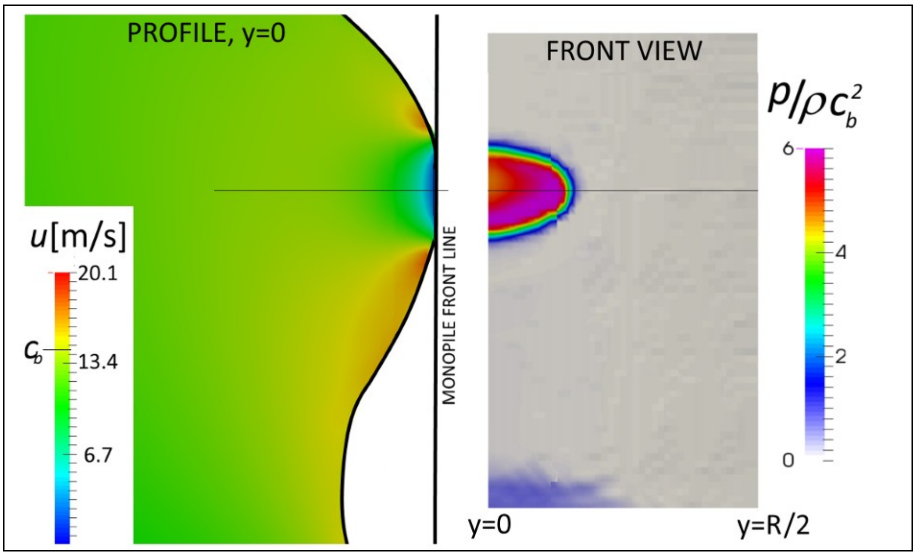

Figure 2.49 Velocity and pressure distribution, t=+$0.011R/c_b$ - case 3

After the overturning wave jet hits the structure, the mass of the water which is pushed away from the structure accelerates. This results in increased velocities in the region below and above the area of the overturning wave jet interaction with the structure, as seen from Figure 2.49 and Figure 2.50 (rectangular area marked with A). Furthermore, the speed of the generated water jets is higher than the breaking wave celerity. As seen from Figure 2.50, the speed of water jet in the horizontal area at the cross-section $z=z1$ (see Figure 2.52) is $2.1c_b$.

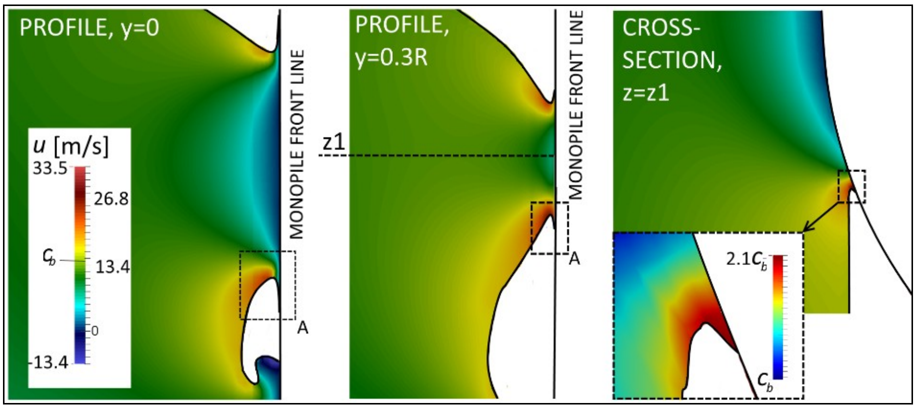

Figure 2.50 Velocity distribution, t=+0.051R/c_b - case 3

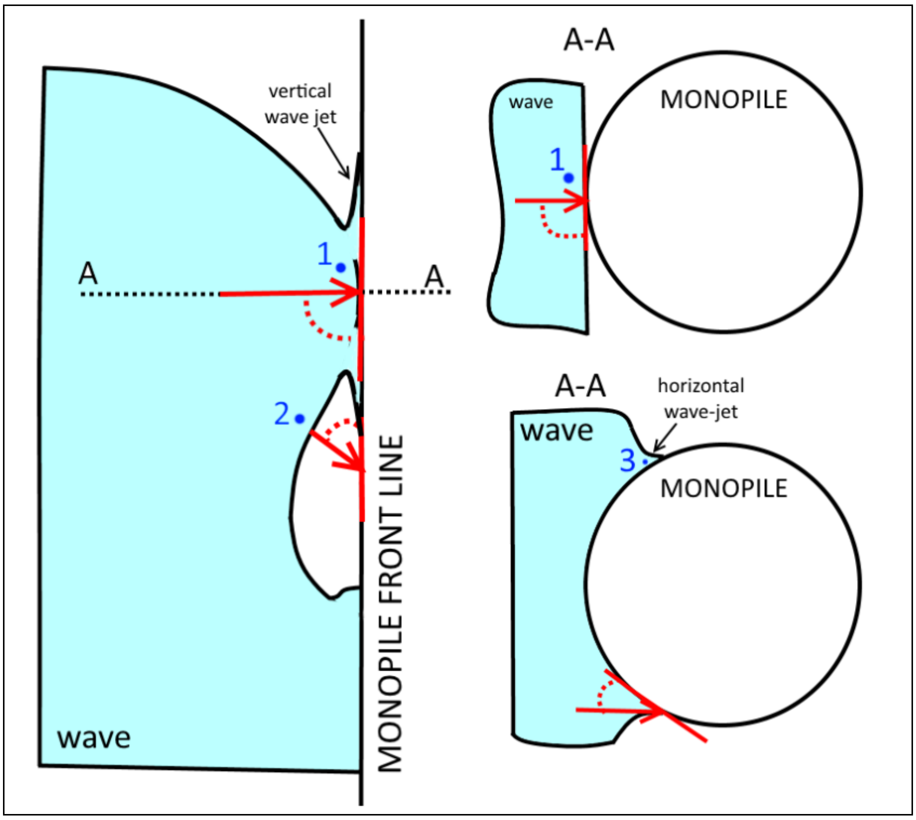

Figure 2.51 Sketch of the overturning wave jet-monopile structure interaction

Figure 2.50 presents the breaking wave interaction with the structure which occurs 0.051R/c_b after the beginning of the overturning wave jet interaction with the structure. The complexity of the breaking wave interaction with the monopile structure at this stage of wave impact is presented in Figure 2.51. At the beginning of the wave impact, the overturning wave jet hits the structure almost perpendicularly (position 1). As the overturning wave jet propagates, the interaction between the wave and the structure happens at lower angles of attack (positions 2&3). If the speed of the fluid is constant, the pressure at position 1 would be higher than at the position 2 and 3. However, the velocity distribution under the overturning wave crest during the wave impact is variable. As seen in from Figure 2.47, the horizontal water particle velocities below the tip of the overturning wave jet are higher than at the tip of the overturning wave jet. Figure 2.50 shows that the horizontal water particle velocities below the area where the overturning wave jet interacts with the structure are increased. Moreover, the speed of the generated water-jets, which effects the wave impact on the structure, are higher than the breaking wave celerity. The vertically oriented water-jets block the clear impact of the overturning wave jet on the structure and cause the damping effects. The horizontally oriented water-jets increase the impact area and the impact pressure on the structure.

Therefore, the temporal distribution of breaking wave impact pressures on a monopile structure is a complex phenomenon which depends on the angle of the attack between the wave and the structure, velocity distribution under the wave crest, and the orientation of the generated water-jets. The impact pressure distribution at the moment which occurs $0.051R/c_b$ after the beginning of the overturning wave jet interaction with the structure is presented in Figure 2.52. The figure shows the pressure distribution in the area of the interaction between the overturning wave jet and the structure, and the pressure distribution in the area of the interaction between the region below the overturning wave jet and the wave run-up on the structure.

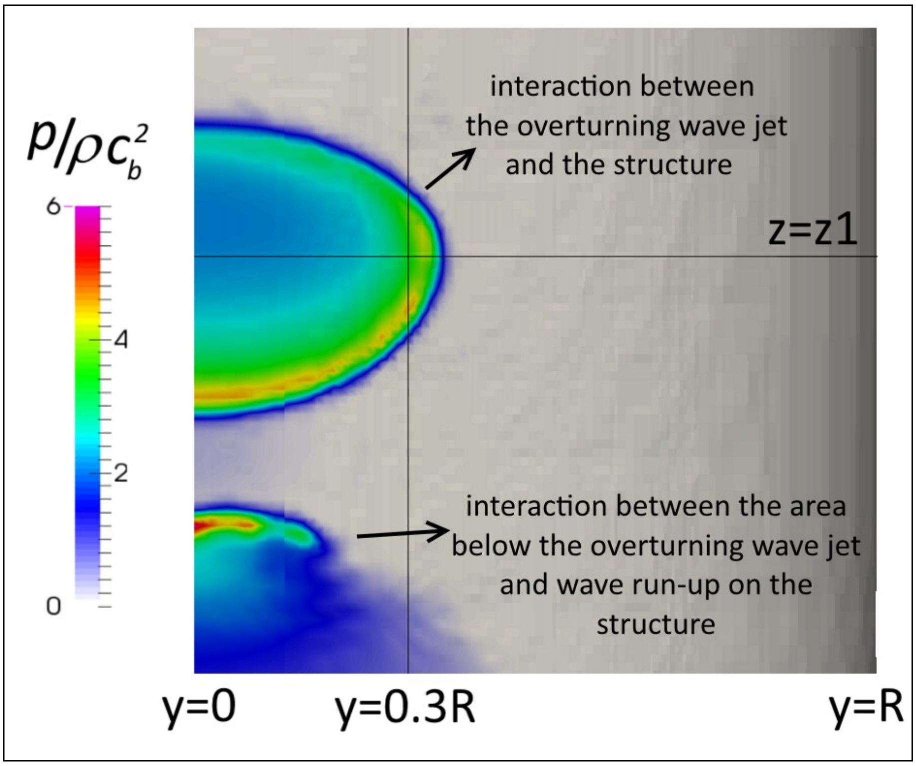

Figure 2.52 Pressure distribution, t=+0.051R/c_b - case 3

Numerical results show that the highest impact pressures occur in the region below the overturning wave jet. This region is characterized by the interaction between the overturning wave jet, generated water-jet which is orientated vertically downwards, and wave run-up which propagates upwards on the structure. The induced impact energy in this region is dissipated through high speed water jets in the horizontal plane. Figure 2.53 shows the pressure distribution and the velocity at the breaking wave free surface at the moment which occurs 0.080R/c_b after the beginning of the overturning wave jet interaction with the structure. The peak pressure which occurs at the azimuth angle $\beta \approx 10^{\circ}$ is induced by the horizontal wave-jet characterized with a speed which is almost 4 times higher than the breaking wave celerity.

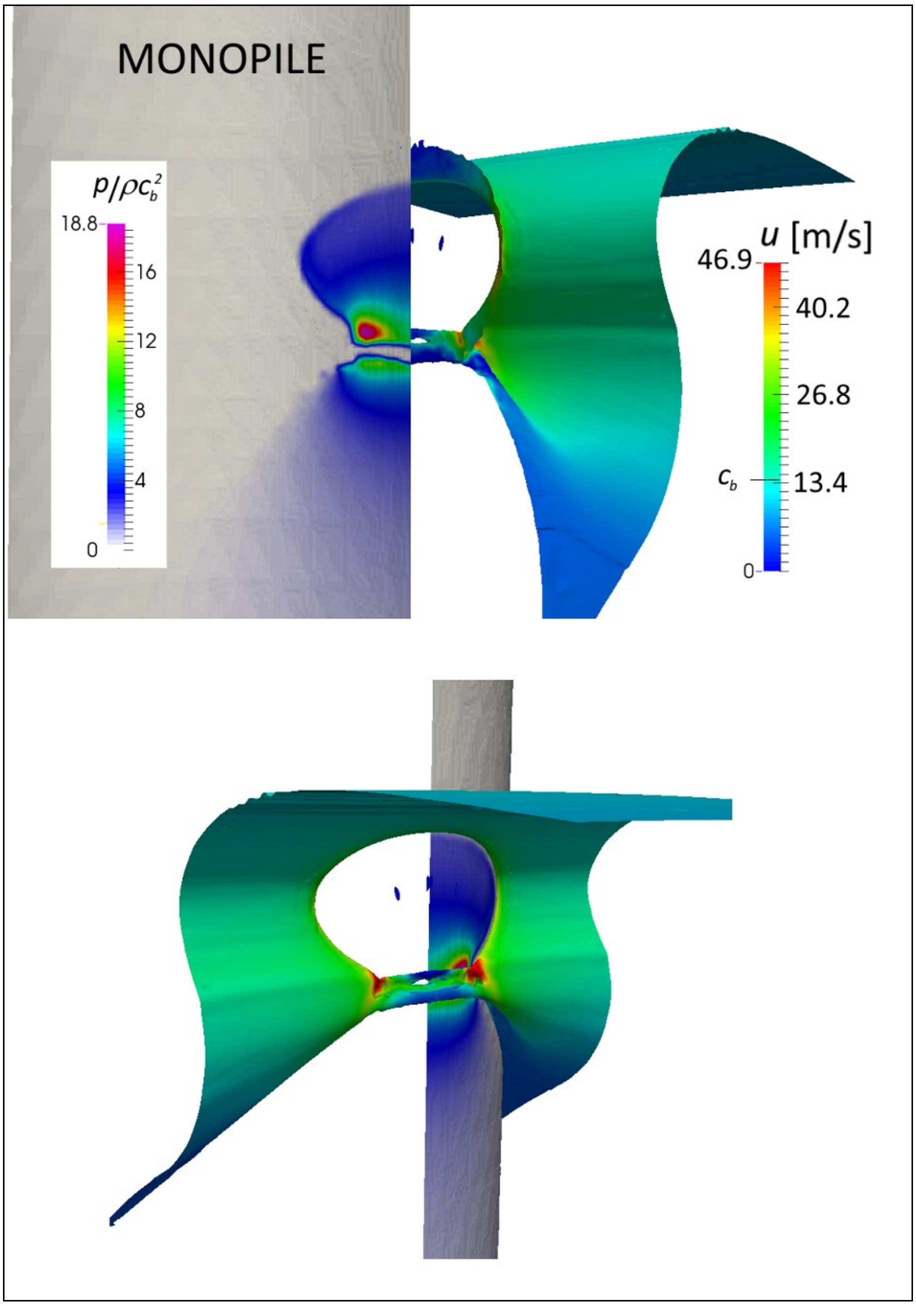

Figure 2.53 Pressure and velocity distribution, t=+0.080R/c_b - case 3

Integration of the pressure in strips around the monopile structure allows analysis of the vertical impact load distribution. The results of vertical impact load distribution obtained from the numerical model of this study can then be compared with the results of the simplified approaches which are applied in engineering practice.

2.5.4 The vertical distribution of the impact load

The monopile structure is divided into small strips dz=0.09m and the strip forces are calculated. The obtained vertical impact load distribution is normalized by $\rho R c_b^2 dz$. Figure 2.54 shows the obtained slamming coefficients C_s at the moment of the maximum impact force for cases 1 and 2. The results show that the peak slamming coefficients occur in the zone of the highest pressure. The value of the peak slamming coefficient approaches 2π for all the analysed cases. Away from the peak region, the slamming coefficients decay rapidly. The area of the impact load on the structure is significantly higher than the impact area which is defined by the curling factor λ.

As it has been mentioned, the approximation of the vertical impact load distribution by the rectangular shape leads to a non-unique and confusing determination of the curling factor and the slamming coefficient. This is presented in Figure 2.54, where for a geometrically determined curling factor λ, the slamming coefficient in case 1 is C_{sr}=1.8π, while in case 2 is C_{sr}=1π.

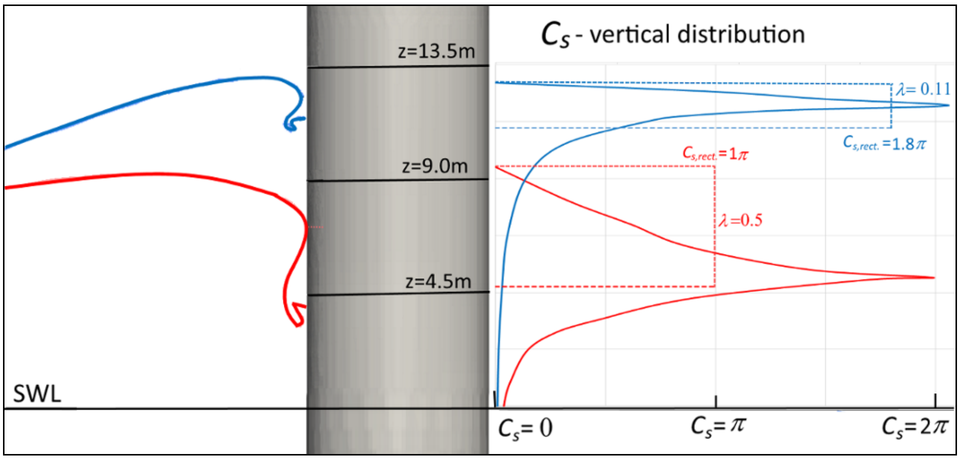

Figure 2.54 Approximation of the area under the computed vertical load distribution by the rectangular shape

Figure 2.55 shows the vertical impact load distribution for all the selected cases. The slamming coefficient is presented in terms of the normalized vertical position, $(z\text{-}z_{pmax})/\eta_b$, where z_{pmax} is the vertical location of the maximum impact pressure. For $z>z_{pmax}$ the impact load distribution is approximated by a linear function - the maximum value occurs at $z=z_{pamx}$ and zero value is located at $z=\eta_b$. For $z<z_{pmax}$ the impact load is characterized by the rapid decay from the peak value $C_s=2\pi$. Figure 2.56 presents the temporal distribution of impact force on the monopile strip located at $z=z_{pamx.}$. The rising phase of the impact force (t<0s) can be approximated by a linear function. Then, the impact force decays rapidly from the peak as clearly show the plots in Figure 2.56.

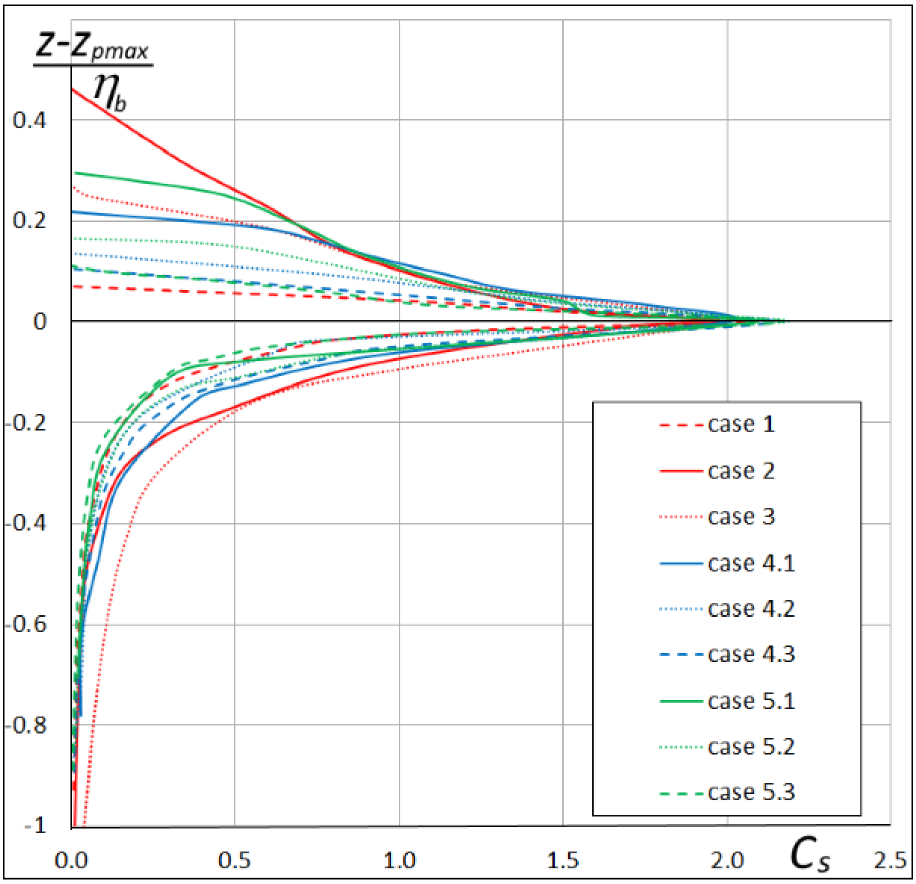

Figure 2.55 Vertical impact load distribution

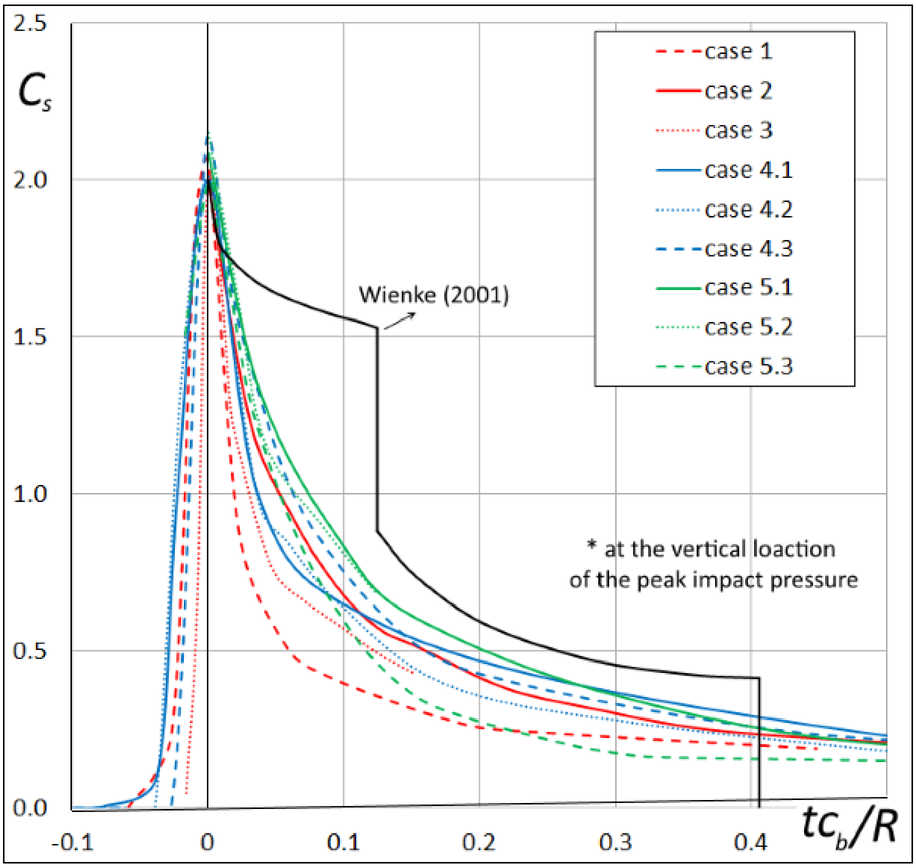

Figure 2.56 Temporal impact load distribution at z_{pmax}

The computed impact forces are compared according to the suggested impact load distribution for different moments of the impact $C_s(z,t)$, given in Figure 2.57. The vertical distribution of the impact load $C_s(z,t)$ is presented for 7 different moments in time t_0 to t_6. The diagram of the impact load distribution is divided in two parts. For the zone $z>z_{pamx}$ the beginning of the impact starts at t_0'=-0.9l/c_b while for the zone $z<z_{pamx.}$ the beginning of the impact starts at t_0=-0.06R/c_b.

For the calculation of the impact force according to the load distribution suggested in the Figure 2.57, the location of the maximum impact pressure z_{pamx} and the length of the overturning wave jet l is required. These parameters can be obtained from a 2D simulation of the breaking wave by applying NS-VOF model. In this analysis it is approximated that the impact pressure occurs approximately at z_{pamx}=1.15$z_{toe,jet}$.

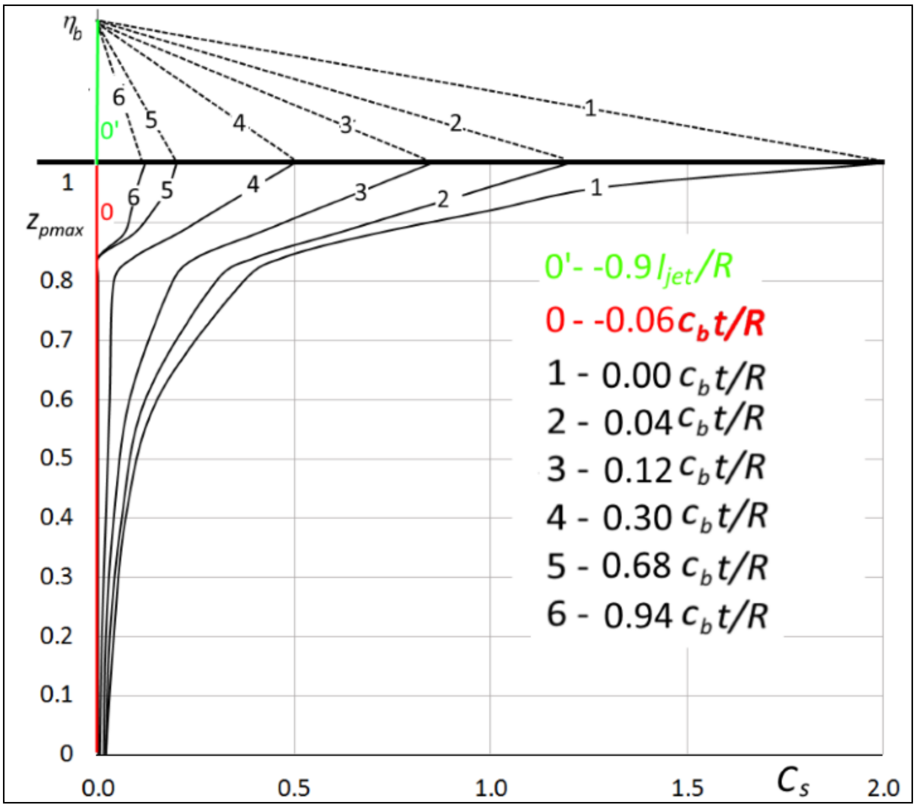

Figure 2.57 Suggested impact load distribution in time $C_s(t,z)$

Figure 2.58 shows the comparison between the computed and the estimated impact force according the aforementioned procedure. The temporal characteristic of the impact force is captured with good accuracy. Discrepancies observed in the impact force peak zone are up to 30%. However, compared to the results of Wienke's simplified approach, the results from the suggested procedure provide a much better approximation of the impact force. These results are encouraging for further development of the proposed procedure to eventually form an alternative method for preliminary estimation of the impact forces.

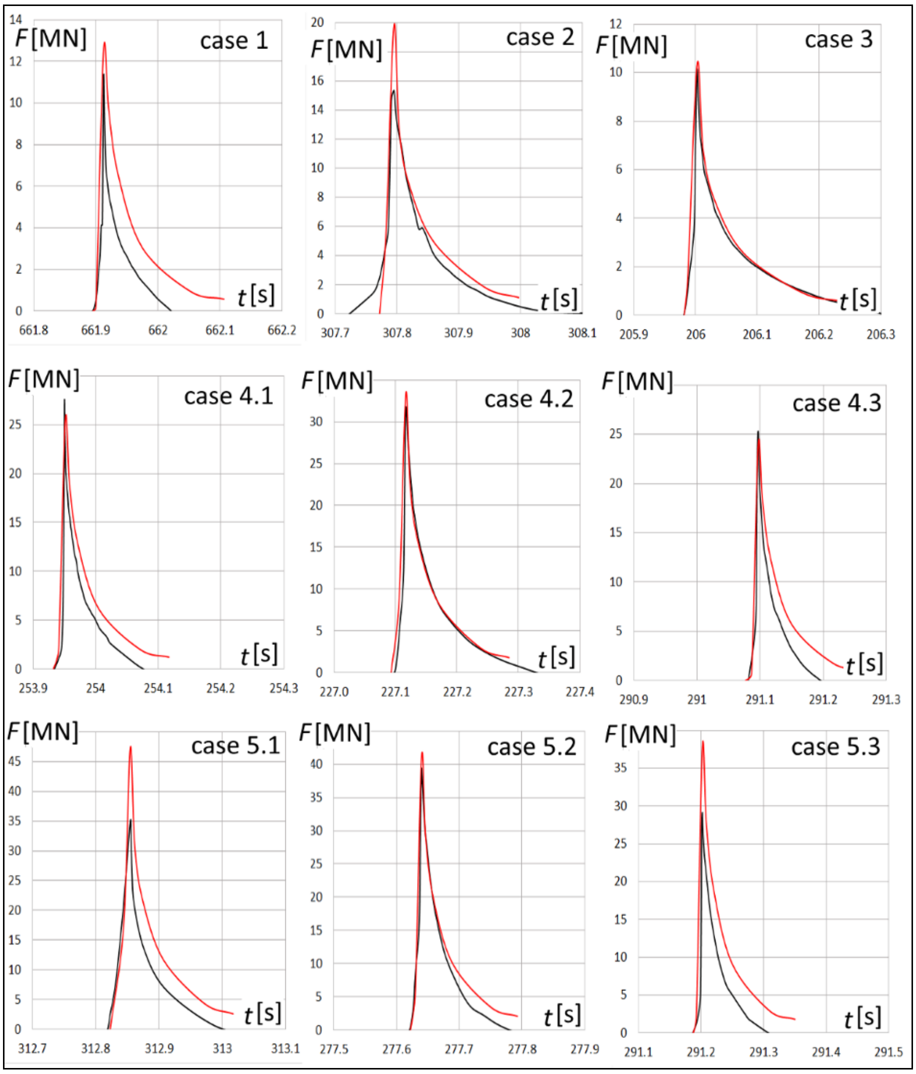

Figure 2.58 Comparison between the computed impact forces and approximate solution

Results from this section are based on the solution of the incompressible numerical model. However, the effect of air compressibility during the breaking wave impact on the monopile structure may be not negligible. This is observed from the results of existing experimental studies, which are characterized by significant oscillations of the measured impact pressure signal. These oscillations are usually associated with the effects of air compressibility. In order to investigate the effect of air compressibility during breaking wave impact on a monopile structure, a compressible numerical model is employed.

2.6 Numerical results - compressible model

The breaking wave impact on the structure is accompanied by air entrapment (white water) and air pockets which can be formed between the overturning wave crest and the structure. This study focuses on the effect of compressibility of air pockets which can be trapped between the overturning wave crest and the structure.

Figure 2.59 shows the beginning of the interaction between the overturning wave jet and the monopile structure (t=33.854s). The air pocket which exists between the overturning wave jet and the monopile structure has open lateral boundaries, which allow free flow of the air. Effect of air compressibility in this moment of the wave impact is not expected. However, results of the incompressible numerical model show that in the later stages of the overturning wave jet propagation, fully trapped air pockets of smaller volumes exist, as it is presented in Figure 2.59 (t=33.856s) and Figure 2.60 (t=33.8564s).

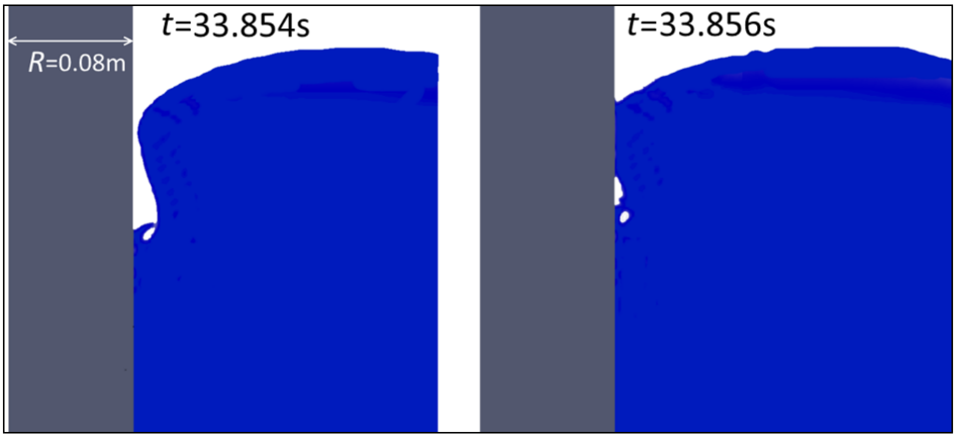

Figure 2.59 Wave profile during the impact on the structure, α=0.5

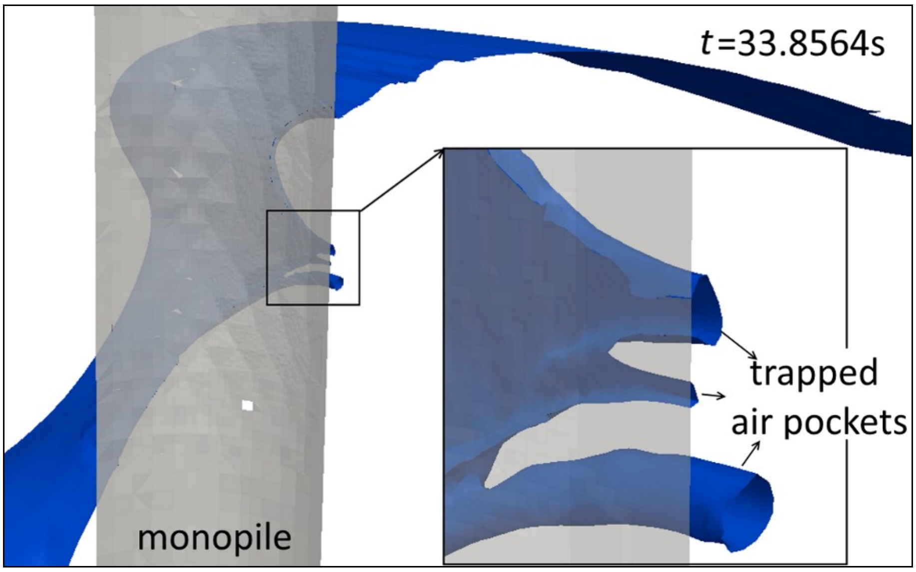

Figure 2.60 Existence of trapped air pockets during the wave impact, α=0.5

The numerical model is modified to the investigate effects of air on an air pocket trapped during the breaking wave impact on a monopile structure. The study in this thesis includes the application of the compressible multiphase flow model *compressibleInterFoam* contained in the OpenFOAM library. As this model is not commonly used and validated so far, the purpose of the study is only to address the importance of the effects of air compressibility during the impact of breaking waves on a vertical cylindrical structure. The *compressibleInterFoam* model consists of the laws of conservation mass, momentum and energy, as well as a transport equation for the water volume fraction. The mass conservation equation is given by

$$\frac{\partial \rho}{\partial t} + \nabla \cdot (\rho \mathbf{u}) = 0 \tag{2.31}$$

The moment equation relates to the equation (2.20). An energy equation expressed in terms of temperature T is given by

$$\frac{\partial \rho T}{\partial t} + \nabla \cdot (\rho \mathbf{u} T) - \nabla \cdot (\mu \nabla T) = -(\frac{\alpha}{c_{v,water}} + \frac{1-\alpha}{c_{v,air}})(\frac{\partial \rho k}{\partial t} + \nabla \cdot (\rho \mathbf{u} k) + \nabla \cdot (\mathbf{u} \rho)) \tag{2.32}$$

in which $k = |\mathbf{u}|^2 / 2$ is the specific kinetic energy, $c_{v,water}$ and $c_{v,air}$ are the specific heat capacities at constant volume for the water and air phases, respectively. The water-air interface is captured by equation (2.21), where the density of the air is correlated to the perfect gas equation of state

$$p = \rho_{air} R_{air} T \tag{2.33}$$

In which R_{air}=287 J/(kgK) is the specific gas constant. The water is treated with following equation of state

$$\rho_{water} = \rho_{0,water} + \psi(p - p_0) \tag{2.34}$$

where $\rho_{0,water}$ is the initial density of water corresponding to the initial pressure p_0. A compressibility coefficient is presented by ψ=1/(R_{water}-T), where $R_{water} = 3000\ J/kgK$.

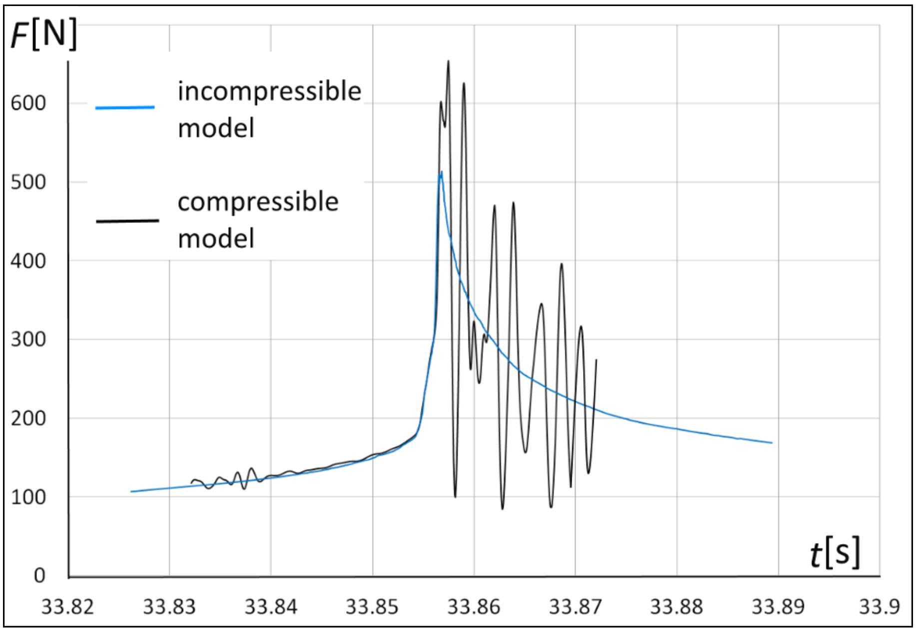

Figure 2.61 Compressible and incompressible computed impact force (model scale)

The effect of air compressibility on the wave impact loading is investigated for case 4.1, presented in section 2.5. The wave propagation before the overturning wave jet hits the structure is solved by applying the incompressible *waveFoam* model, while the wave impact on the structure is solved applying the *compressibleInterFoam* model. Figure 2.61 shows the comparison of the computed impact force between the results of the incompressible and compressible numerical model, considering the model scale analysis with scale factor 45. The results show that the rising phase of the impact force calculated with both incompressible and the compressible numerical models, has the same characteristics. The peak of the impact force obtained with the compressible numerical model is almost 40% higher than that from the incompressible numerical model. The decay phase of the impact force obtained applying the compressible model is characterized by strong oscillations which decay in time.

Figure 2.62 shows the temporal pressure distribution on the monopile structure. The breaking wave free-surface which is presented in Figure 2.62 relates to the water-air interface which contains ≥10% of the air phase in the mixture. Presented results show the fluctuation of the impact pressures in range of $\approx 0.9 p_{atm}$ to $\approx 1.5 p_{atm}$. Figure 2.63 and Figure 2.64 present the breaking wave free-surface which relates to the water-air interface which contains ≥50% of the air phase in the mixture. Figures show the pockets of the water-air mixture trapped in the body of the wave. The upper pocket is located on the vertical location of the highest impact pressure on the structure.

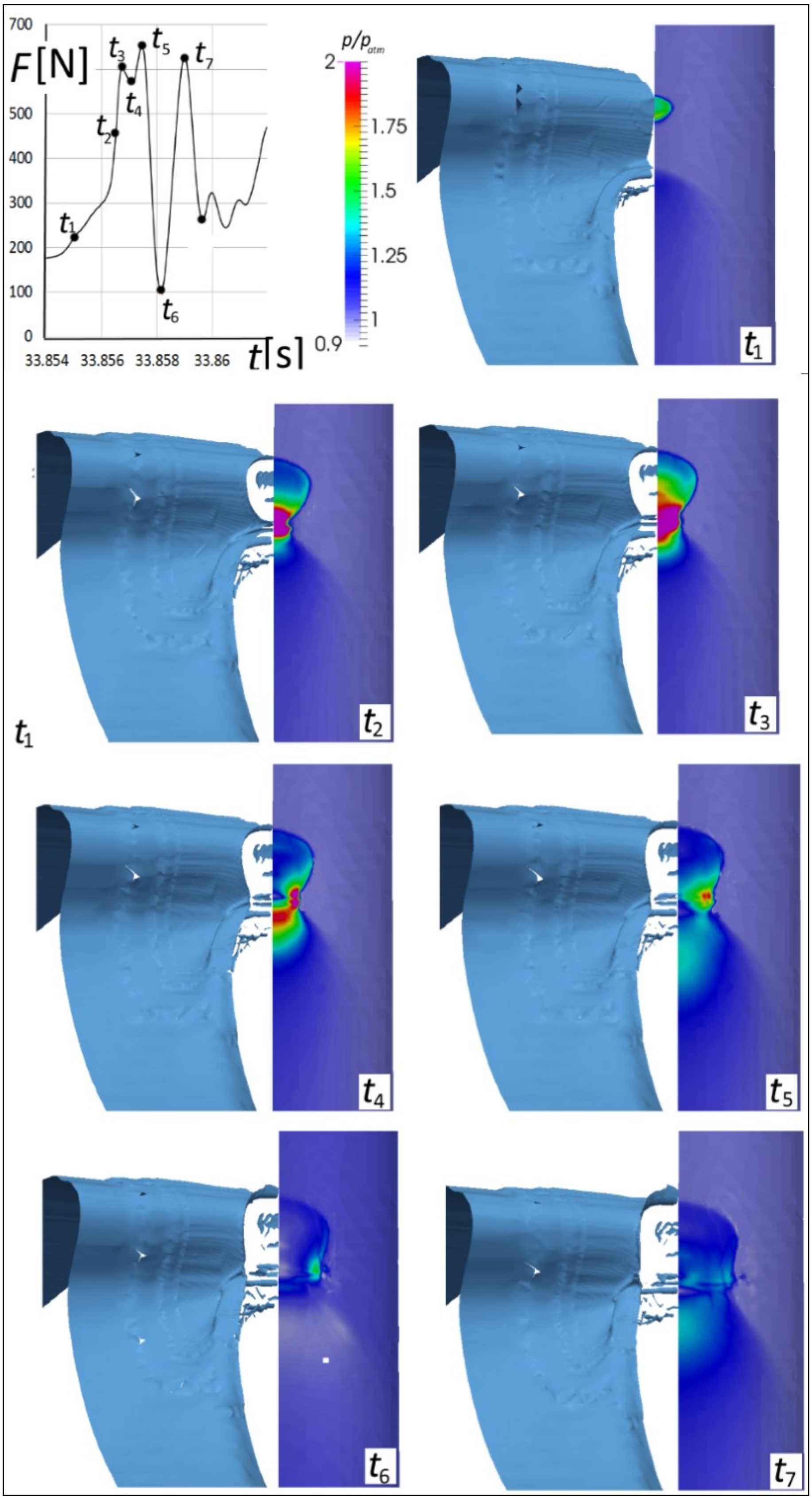

Figure 2.62 The impact pressure fluctuation (compressible, model scale)

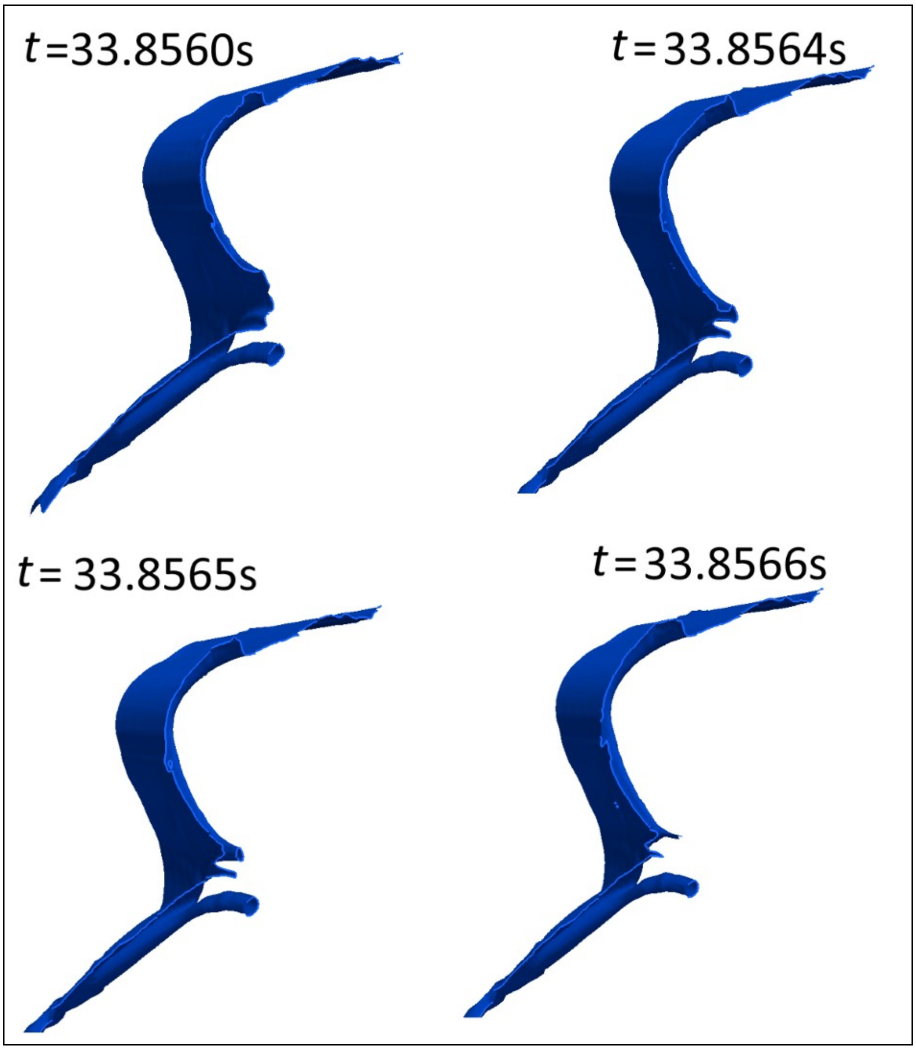

Figure 2.63 Breaking wave water-air interface α=0.5

During the wave impact on the structure, the trapped pockets pass through expansion and contraction phases. When the pockets of the water-air mixture are compressed, a portion of the wave impact energy is transferred to the air pocket. When the compressed pockets start to expand the stored energy is released. When the pressure in the expanded pockets is lower than the surrounding pressure, the trapped pockets begin to compress again. This cycle repeats until the initial impact energy is lost.

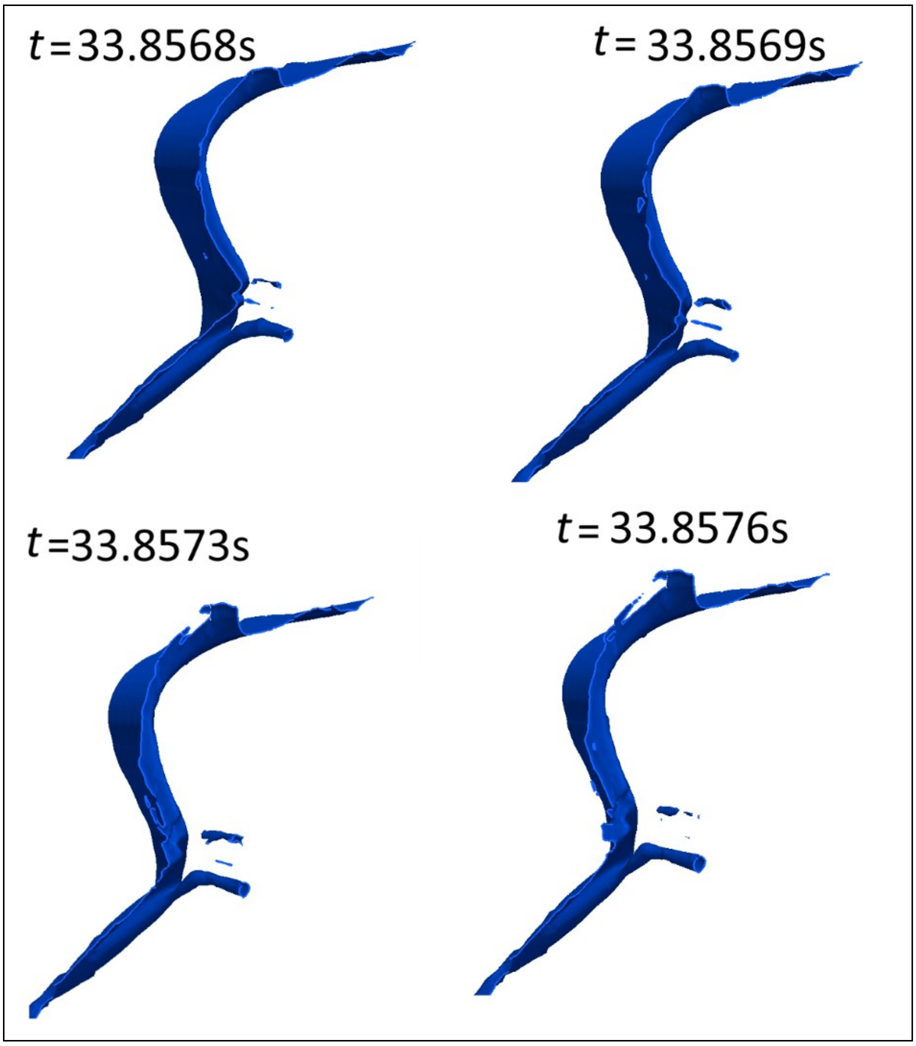

Figure 2.64 Breaking wave water-air interface α=0.5

The phases of the expansion and contraction of the trapped pockets of the water-air mixture are in synchronisation with the pulsating pressures on the structure. The moment when the compressed pocket starts to expand relates to the crest of the pulsating pressure, while the moment when the expanded pocket starts to compress relates to the trough of the pulsating pressure. Figure 2.65 shows the impact force and the impact pressure which is measured on the front line of the structure at the vertical location of the upper pocket. The oscillation of the impact pressure follows the oscillation of the impact force. The highest impact pressure obtained from the compressible numerical model is p_{max}≈$4.5p_{atm}$, while for the incompressible numerical model is p_{max}≈$2.5p_{atm}$.

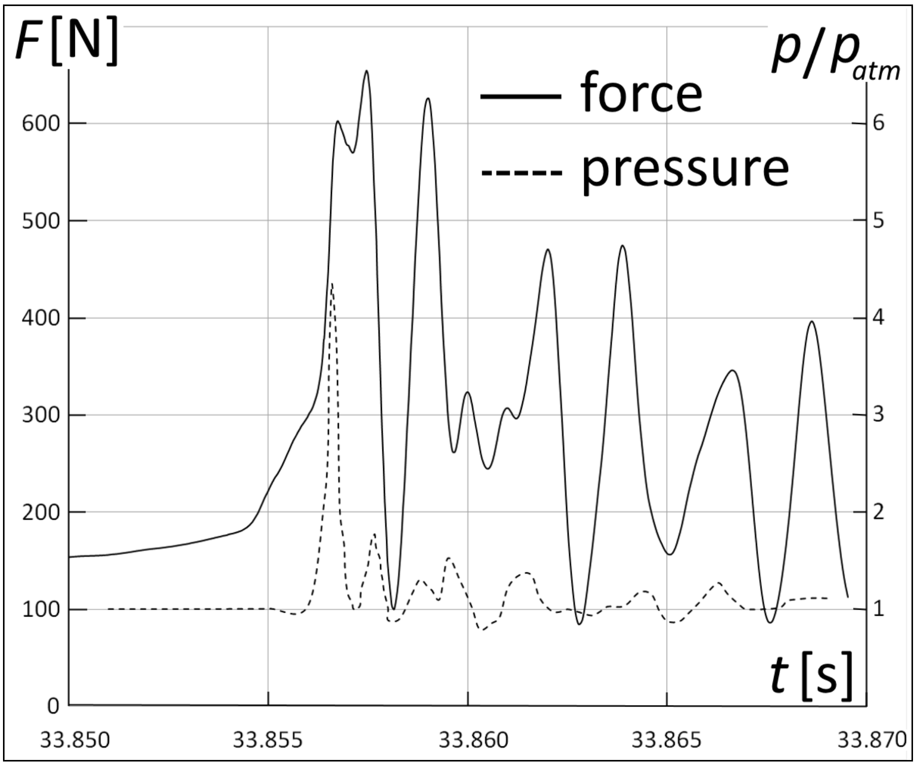

Figure 2.65 Impact pressure and impact force (compressible, model scale)

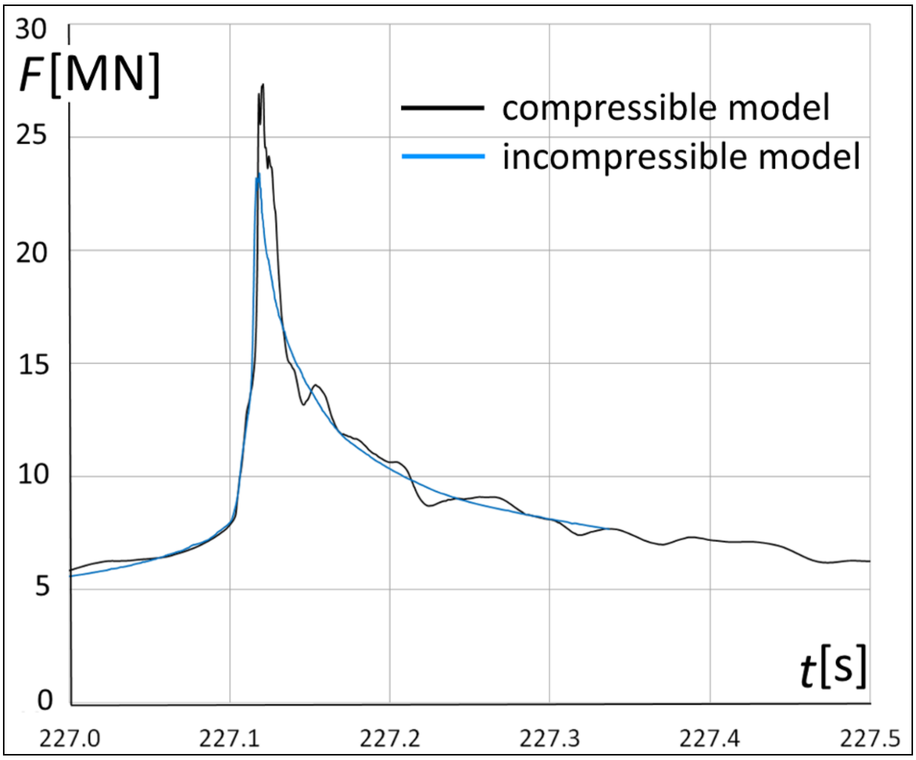

Figure 2.66 Compressible and incompressible computed impact force (prototype scale)

An additional case is analysed, which also corresponds to case 4.1 but computed at prototype scale. The results of the computed impact force obtained by applying the incompressible and compressible numerical model for the prototype scale case are presented in Figure 2.66. The rising phase of the impact force are almost identical between the incompressible and the compressible numerical model. The peak of the impact force from the compressible numerical model is almost 30% higher than from the incompressible numerical model. The decay phase of the impact force obtained from the compressible numerical model is characterized by the weak oscillations and it is very similar to the results of the incompressible numerical model.

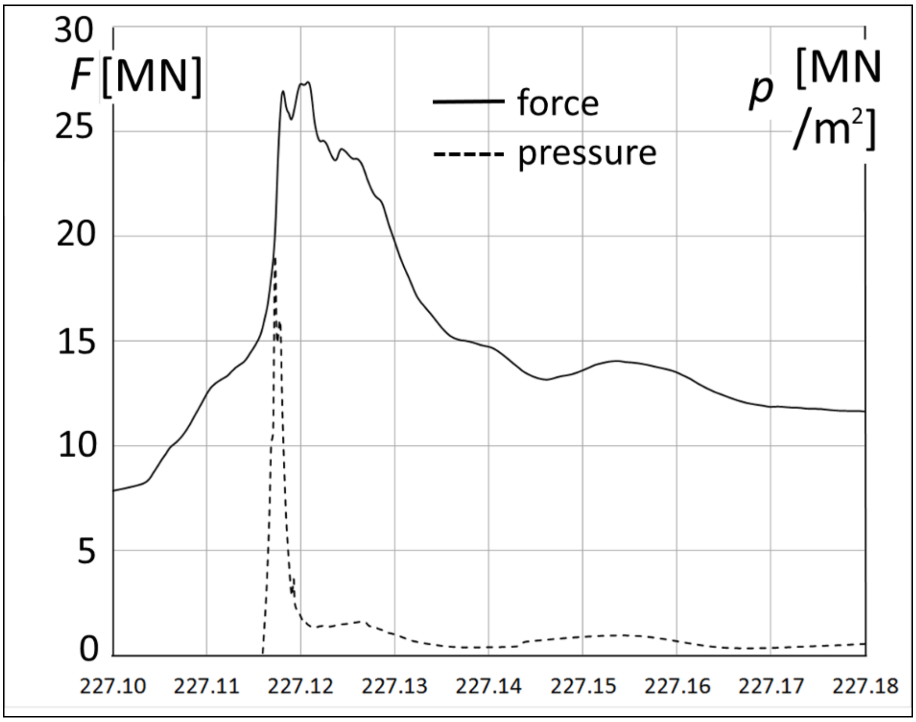

Figure 2.67 Impact pressure and impact force (compressible, model scale)

Figure 2.67 presents the impact pressure on the structure measured on the front line of the structure at the vertical location of the upper trapped pocket of the water-air mixture. The magnitude of the impact pressure oscillations in the decay stage is low, compared to the magnitude of the peak impact pressure. The peak impact pressure is p_{max}≈$190p_{atm}$. The impact pressure in decay stage oscillates in the range of $0.01p_{max}$ - $0.05p_{max}$. Considering the impact pressure for the case of the model scale analysis (Figure 2.65) the range of pressure oscillations in the decay stage is $0.23p_{max}$ - $0.38p_{max}$. Results show that the effect of the impact pressure oscillations on the magnitude of the impact force is important for the model scale analysis, while it is less significant for the analysis at prototype scale.

2.7 Summary

A numerical model is employed to investigate effects of breaking wave shape and trapped air pockets in analysis of a breaking wave impact loading on a monopile structure. Effects of braking wave shape on an impact load is analysed applying the incompressible model, while effects of trapped air pockets on an impact load is analysed applying the compressible model. Both numerical models are based on solution of the Navier-Stokes/VOF set of equations. The computational grid sensitivity analysis is conducted to show influence of the air-water interface thickness on the solution. To reduce the computational cost, the numerical domain is decomposed into an outer and an inner domain, combining a non-linear potential flow model and a Navier-Stokes/VOF model, respectively.

Results obtained applying the incompressible numerical model are compared with results obtained applying simplified approaches used in the engineering practice. The non-impact part of the breaking wave load is compared with the solution of the Morison's equation based on the stream function wave kinematics. The impact part of the breaking wave load is compared with results obtained applying Wienke (2001) and DNV (2010, 2014) simplified approaches.

In order to better understand the complex phenomenon of the breaking wave impact on the structure, the pressure and the velocity distribution are analysed for a high spatial and temporal resolution. To analyse the distribution of the impact load, computed pressures are integrated on the strips of the monopile structure. The obtained area under the impact load distribution is then represented with the equivalent rectangular area. Parameters of the equivalent rectangular distribution are compared for all analysed cases. High scatter of the results is obtained. However, similarities between the impact load distribution considering all analysed cases exist. This encourage us to propose an alternative method for the preliminary calculation of the breaking wave impact forces.

The compressibility effects of the trapped air captured between the overturning wave jet and the structure are analysed for one selected case, but for both model and prototype scale. The results show that air pockets, which are trapped between the overturning wave jet and the structure during the wave impact, are compressible and pass through expansion and contraction phases, which results in the pulsating impact pressure during the wave impact. The differences in impact force characteristics are found between the model and prototype scale.

3 Experimental analysis

Available measurements from laboratory experiments conducted on a breaking wave impact on cylindrical structures are presented in the Appendix II. The presented results refer to cases for which the overturning wave jet hits the monopile just below the wave crest level. An average magnitude of the peak impact pressure is $p \approx 15\rho c_b^2$, and an average time of pressure rising phase is $t_{pi} < 0.02R/c_b$. Discrepancies from these general observations are found only in experimental study of Hildebrandt & Schlurmann (2012). They reported lower magnitudes of average peak pressures and a longer duration of an average time of impact pressure rising phase. Numerical results of this study show that a longer duration of the impact pressure rising phase is effected by the wave run-up on the structure, which damps a wave impact. This type of damping of the wave impact loads occur for breaking waves of lower wave front steepness. This kind of breaking wave cases was considered in the experimental study of Hildebrandt & Schlurmann (2012).

This study includes experimental data obtained from laboratory measurements conducted at Deltares, Delft. Storm conditions at a wind farm location were simulated in the wave basin. More than 10000 irregular waves were generated. In the course of the laboratory experiments, numerous breaking wave impacts on a monopile structure were observed and analysed.

This section contains description of the conducted experimental procedure, post-processing procedure, and discussion. The results of experimental measurements are used to validate the applied numerical model.

3.1 Experimental procedure

Experiments were conducted in a wave basin defined by length of 75m, width of 8.7m, and maximum water depth of about 1.2m. The global force, impact pressures and wave elevations were measured during the tests and the wave-structure interaction processes were visually recorded by a high-frequency video camera.

For accurate measurements of the hydrodynamic force, an infinitely high natural frequency of the structure is desirable. In order to increase the natural frequency of the structure, the monopile was made of aluminium to provide high stiffness and low weight. To further increase the stiffness, the structure was connected to a stiff frame, as it is shown in Figure 3.1. The lowest measured natural frequency of the system in water is 80Hz. Considering this natural frequency, it is expected that high impact load components may induce structure vibrations.

The forces were measured with two 3D force transducers type K3D120, produced by MEMeßsysteme GmbH. The transducers are watertight and with the range of 1 kN each. A force transducer was attached to the top and another one to the bottom connection. In order to obtain statically determined system, which can be analysed using static equations, transducers were installed as presented in Figure 3.2. The top transducer and the structure were connected with the roller, so that a system was free of constraints in the vertical direction. The bottom transducer and the structure were connected with the pin connection installed in the impermeable pocket located in the basin floor.

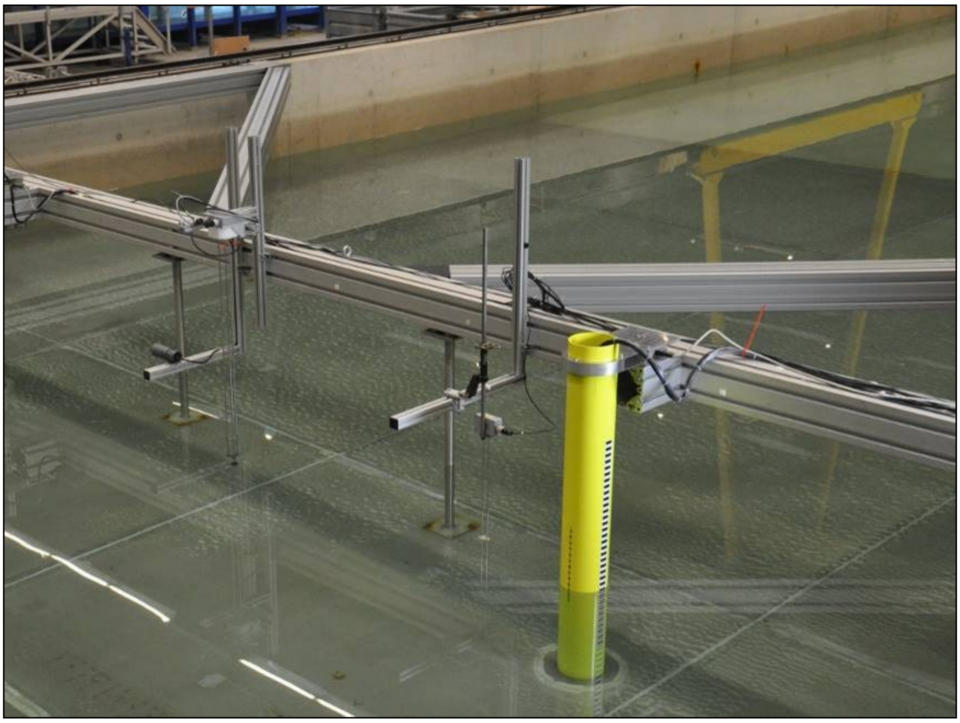

Figure 3.1 Installation of the monopile structure

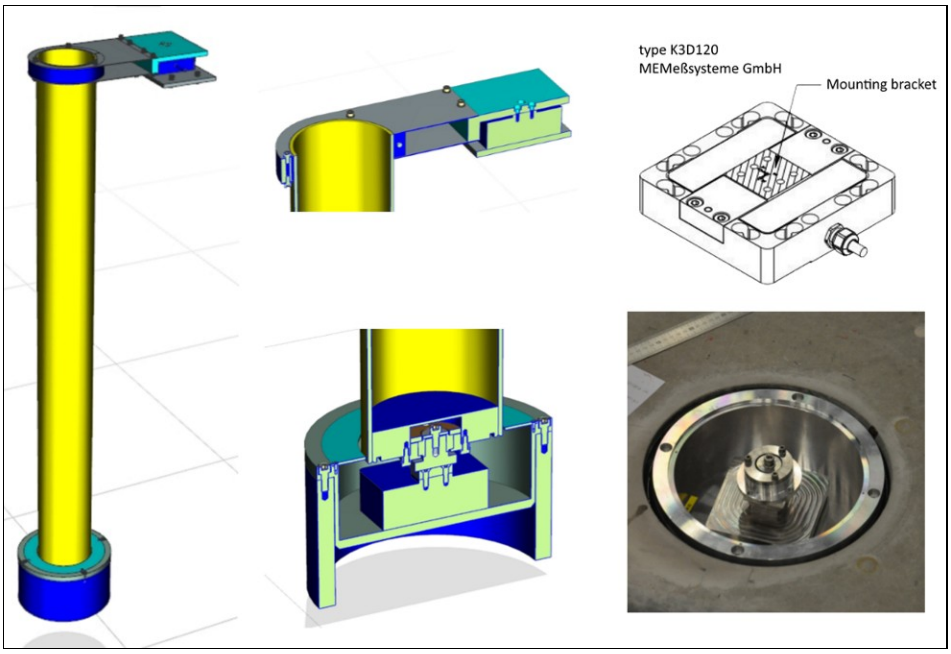

Figure 3.2 The force sensor installations

The monopile structure was equipped with 10 pressure transducers distributed evenly along the front face of the structure in the wave impact zone. The effective area of each pressure transducer was 33mm^2. A sampling frequency of 1000Hz was applied, which is too low to precisely capture a peak impact pressure. However, from the temporal distribution of impact pressure different stages of the breaking wave impact can be identified. The tests were conducted for wave breaking over a flat seabed and wave breaking over a sand bar. Both cases were analysed using an identical model of a monopile structure. Because of differences in water depth in experiments conducted for wave breaking over the flat seabed and over the sand bar, the position of pressure sensors on the structure needed to be modified for each analysed case. Altogether, 15 holes were available in the structure, as presented in Figure 3.3, the last 5 holes were closed in experiments conducted for wave breaking over a flat seabed, while in experiments conducted for wave breaking over a sand bar the first 5 holes were closed.

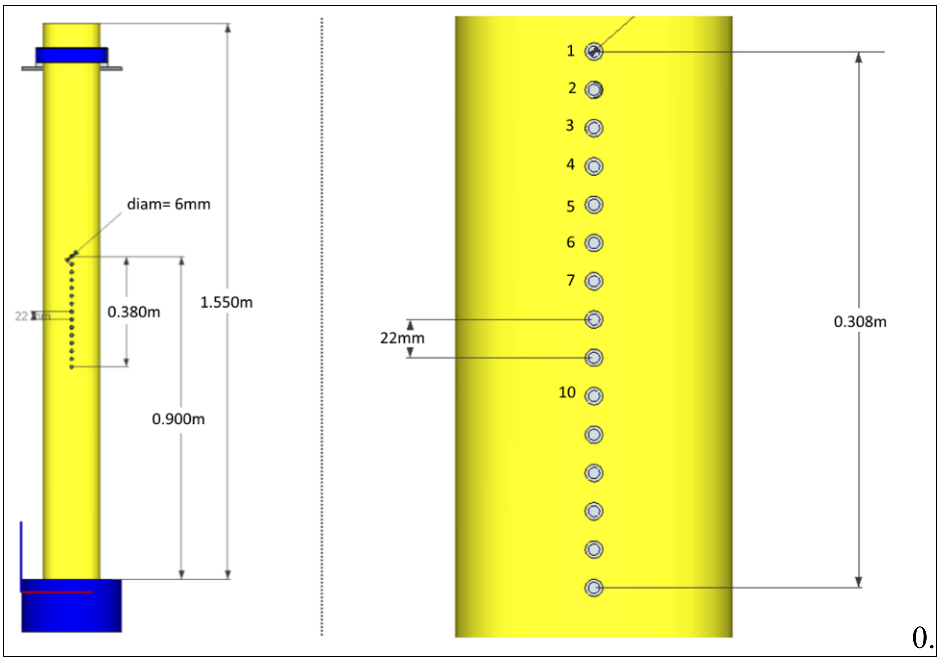

Figure 3.3 Pressure sensor installations

The generated sea state conditions represent the typical wave conditions that might occur at a wind farm location. For the reference, meteorological data refer to those found in the German Bight. The water depth in the German Bight varies between 28m and 36m. The extreme sea storm condition which occurs once in 50 years is defined with the significant wave height of 10m and the peak wave period of 13.3s.

The model scale was chosen as the largest scale possible for the selected wave conditions with respect to the limitations of a wave generator. The selected scale factor was 1:45. The diameter of the structure was D=0.16m, and the water depth d=0.667m, which corresponds to D=7.2m and d=30m in the full scale. As it was previously mentioned the laboratory experiments in the wave basin were conducted for irregular wave propagation over the flat seabed and over the sand bar (Figure 3.4). The sand bar was made of wooden ramps and a concrete section. The construction of the sand bar reduced the water depth by 11.1cm. The physical model represents a sinusoidal sand bar of the crest length of 300m and the height of 5m at the prototype scale.

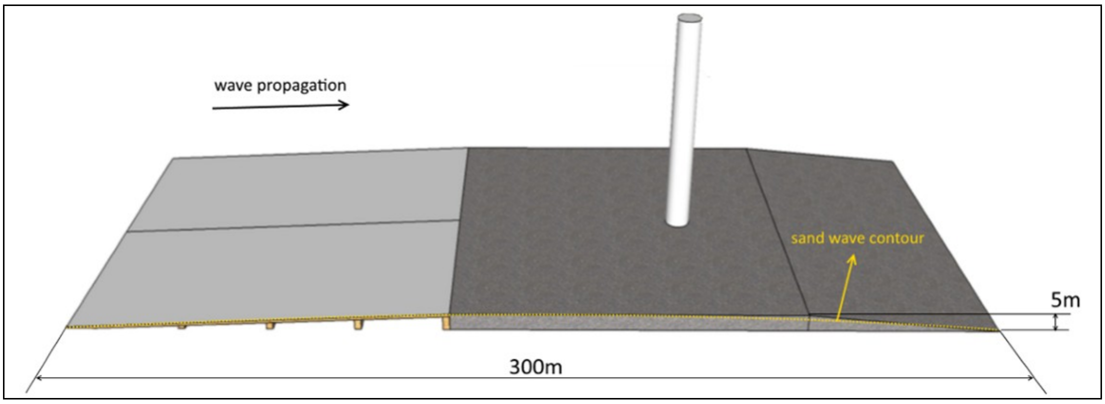

Figure 3.4 Design of the sand bar

Wave conditions were simulated according to the JONSWAP energy spectrum. The main parameters of the spectrum were H_s=0.22m, T_p=1.94s, and γ=3.3. Water waves were generated with a piston-type wavemaker. A wave absorbing beach was installed at the end of the basin to reduce wave reflections. Each irregular wave test was conducted for a minimum of 5000 waves. Each test was split into 5 separate sub-tests conducted for a different random seed of wave phases. The duration of each test was 1744s, which corresponds to approximately 1000 waves.

It is difficult to directly measure wave impact loads on a structure. As the measuring system is not perfectly rigid, what is actually measured is the structure response, and not the hydrodynamic force. The example of the measured inline force signal is presented in Figure 3.5. The oscillations of the measured force arises from the vibration of a structure and, eventually, the effects of air compressibility analysed in more details in section 2.6.

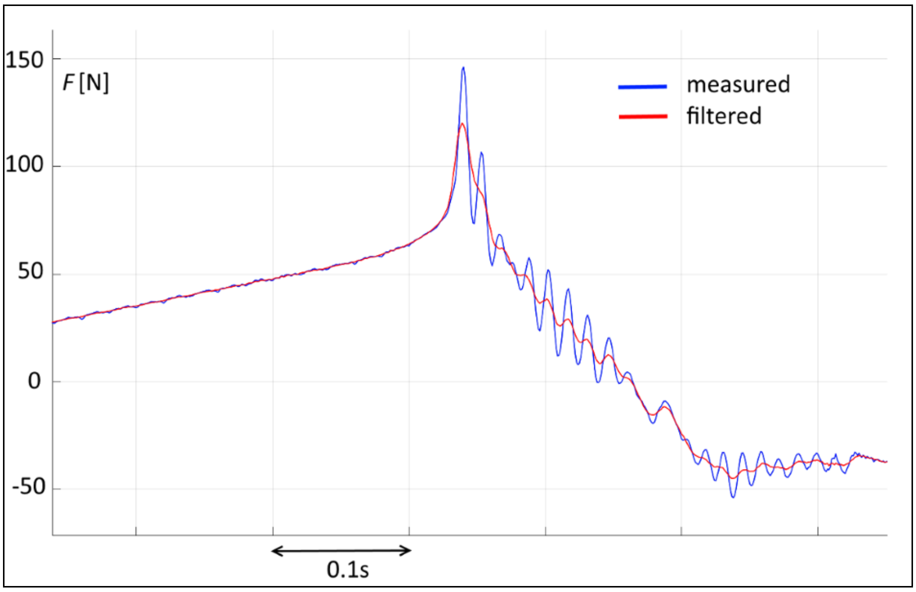

Figure 3.5 Measured and filtered inline force signal

The force measurements were filtered out using a one degree of freedom (1-DOF) transfer function. The methodology is explained as follows. The measured force can be estimated by the linear stress-strain transfer function:

$$F_{measured} = kx_{dyn} \tag{2.35}$$

where x_{dyn} is the structure response, and k is the stiffness of the force transducer. The linear stress strain relation assumes that the forcing frequencies are much slower than the natural frequency of the structure. However, if the forcing frequencies are closer to the structural vibration frequencies, the significant difference between the applied hydrodynamic force and the measured reaction force is expected. By assuming that the structure is free to move in one horizontal direction, the dynamic behaviour of the structure can be taken into account. In the time domain the displacement of the dynamic system is governed by the following equation of motion:

$$m(\ddot{\ } \quad \dot{\ } \quad {}_{dyn}) = F_{hydrodynamic} = F \tag{2.36}$$

where m is the mass, b is the damping and k is the stiffness. In order to reconstruct the hydrodynamic force, equation (2.36) may be used as a transfer function. Inserting equation (2.35) into equation (2.36), the following relation between the measured and the applied hydrodynamic force is obtained:

$$\frac{1}{\omega_n^2}\ddot{F}_{measured} + \frac{b}{k}\dot{F}_{measured} + F_{measured} = F \tag{2.37}$$

where $\omega_n = 2\pi f_n$ is a natural frequency of the system. The derivatives of $F_{measured}$ on the left-hand side can be derived from the force measurement, and natural frequency can be determined from hammer tests. If it is assumed that the system is lightly damped and relatively stiff, $b/k \to 0$, the total hydrodynamic force may be estimated by equation (2.37).

Differences between the magnitudes of measured and filtered forces are shown in Figure 3.6. For small wave loading only minor discrepancies are seen, whereas for larger wave loading the difference between the peak forces becomes significant and may exceed 20%.

The aforementioned procedure neglects the effects of air compressibility on the oscillatory behaviour of impact loading.

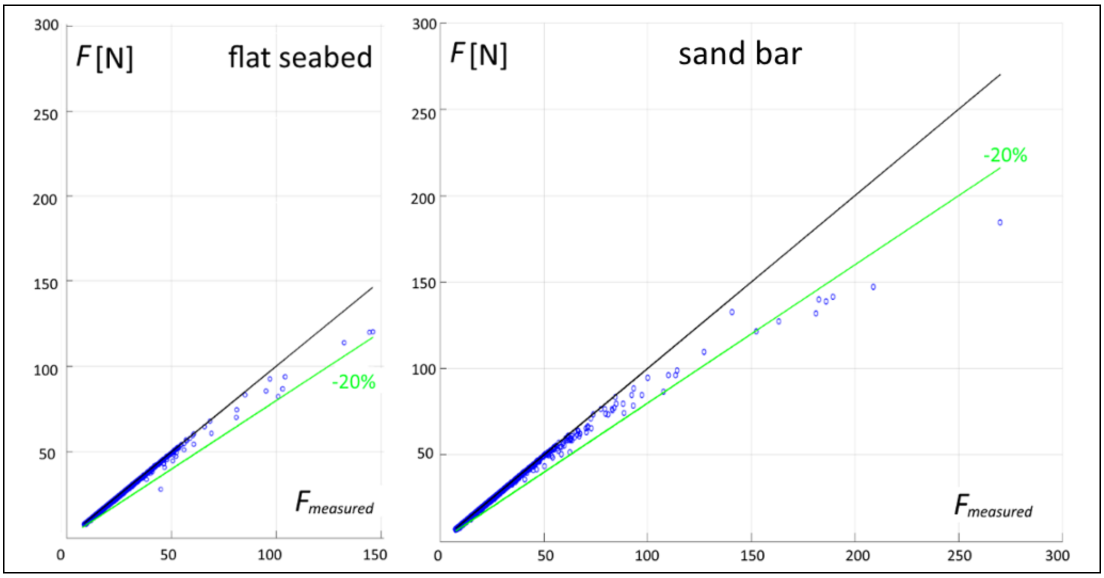

Figure 3.6 Differences between the measured and filtered hydrodynamic forces

3.2 Validation of the numerical model

The numerical model used in this study has been validated with experimental results obtained for non-breaking waves e.g. Paulsen (2013). The validation conducted for breaking waves is very limited and is available only for the incompressible numerical model in the recent study of Ghadirian et al. (2016). They showed that measured wave elevations and impact pressures at the front line of the cylinder are consistent with the results of the numerical model. However, they also presented several cases where considerably underestimated computed impact force was detected. As presented in section 2.4, magnitude of a computed impact force strongly depends on an air-water interface thickness. If an air-water interface thickness is not sufficiently sharp, the magnitude of the computed impact force is underestimated. The information of computational grid size within the wave impact zone and corresponding air-water interface thickness were not provided by Ghadirian et al. (2016).

Because of the stochastic nature of air entrapments and trapped air pockets, the exact comparisons between results from experimental and numerical model is not possible. In this study the laboratory measurements are filtered according to the procedure explained in section 0, and the results are compared with the results of the incompressible numerical model.

The validation of the applied numerical model focuses on measurements for which the maximum hydrodynamic force is recorded. The validation case 1 refers to wave breaking over the flat seabed, while validation case 2 refers to the wave breaking over the sand bar.

Figure 3.7 shows the dependency between the measured hydrodynamic force, wave height and down-crossing wave period. The red dots in Figure 3.7 denote the slamming events, which are estimated by assuming that the force signal is shorter than 1/8 of the peak wave period and the magnitude is larger than $>3rms(F)+mean(F)$, where *rms* is the root mean square operator and *mean* is the mean operator. The numbers of detected slamming events in the presented experiments are shown in Table 3.1. In the case of the experiments with the sand bar, the breaking wave events occur more frequently, as expected. Taking into account the total number of waves for each case, the probability of occurrence of the slamming event in experiments conducted with a flat seabed is 0.3%, while in experiments conducted with a sand bar is 1.2%.

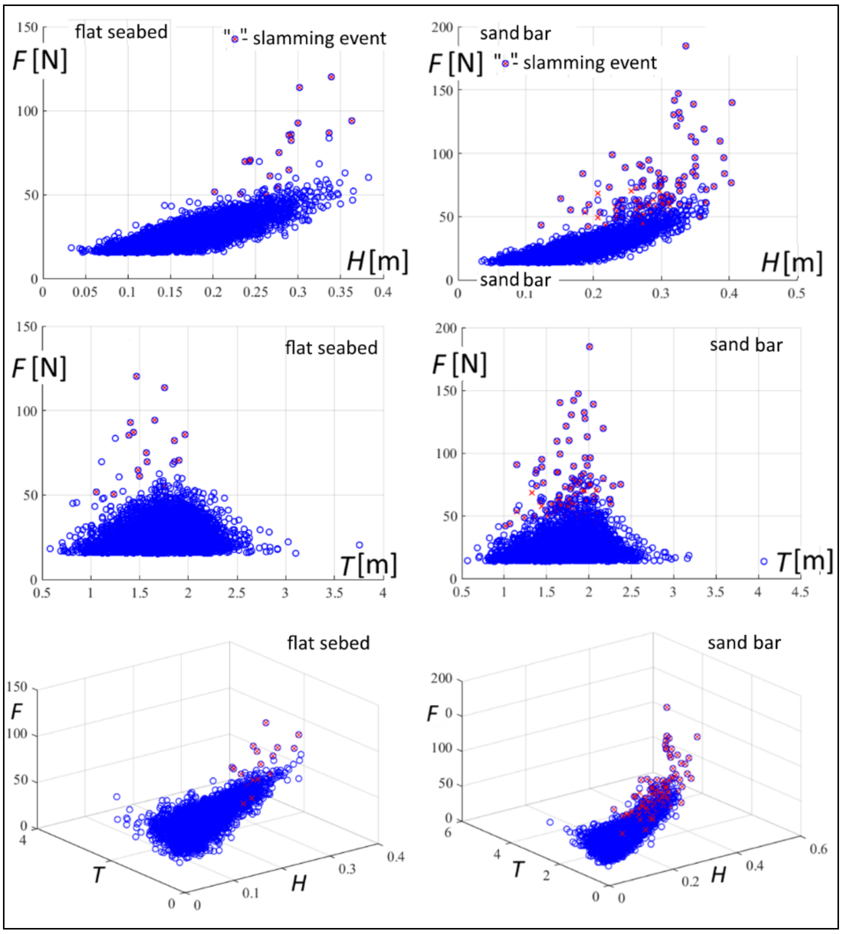

Figure 3.7 Scatter diagram, inline force vs wave height and wave period

Table 3.1 Number of generated waves and corresponding slamming events

Nr	Name	A	B	C	D	E	SUM
1	FLAT BOTTOM numb. of waves numb. of slamming events	 1008 3	 1004 3	 1019 1	 993 4	 1015 4	 5039 15
2	SAND WAVE numb. of waves numb. of slamming events	 1038 13	 1001 13	 1018 11	 1004 10	 1006 13	 5067 60

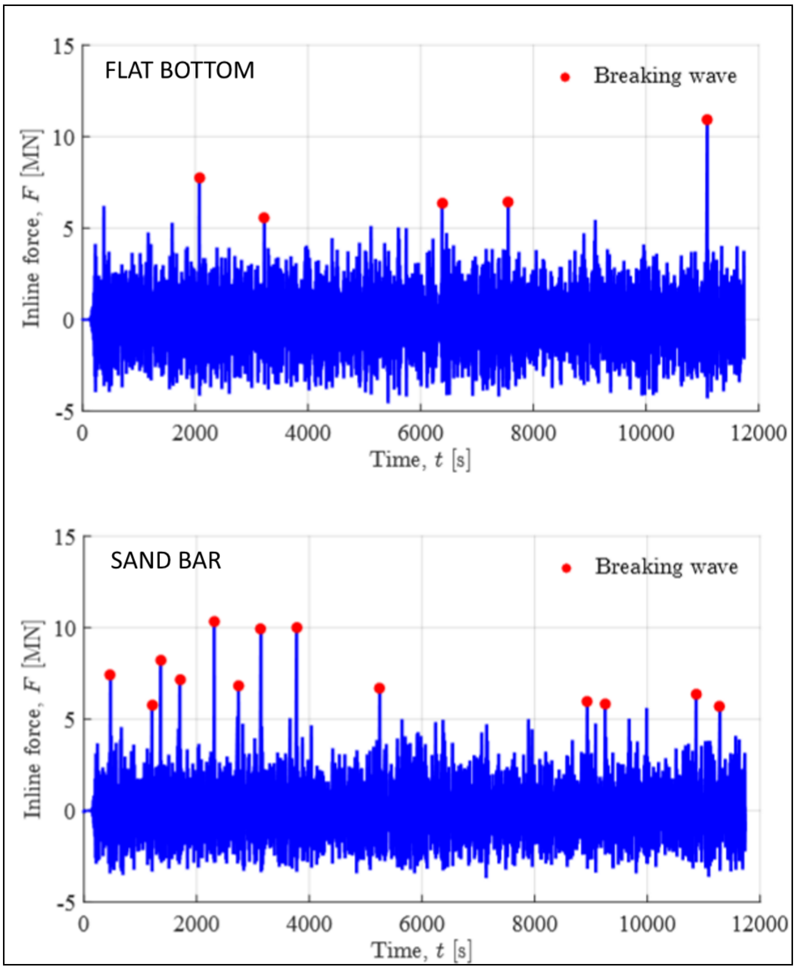

Figure 3.8 The inline-force measurements (full-scale)

The examples of measured inline force signal and detected slamming events are presented in Figure 3.8. The maximum inline force measured for the case of the sand bar is 50% higher than for the case of the flat seabed (Table 3.2). The maximum observed inline force for both cases corresponds to the wave height H_b≈$1.5H_s$, which is slightly higher than Veritas (2010) recommendation H_b≈$1.4H_s$.

Table 3.2 The maximum measured force

CASE	F_{max}	T/T_p	H/H_s
	[N]	[/]	[/]
FLAT BOTTOM	119.3	0.75	1.54
SAND WAVE	184.6	0.97	1.53

The experimental results are reproduced applying the kinematic wavemaker boundary condition at the inlet boundary of the numerical model. The obtained numerical results are compared with experimental measurements of the wave elevation, the hydrodynamic force, and the pressures along the front line of the monopile. The numerical results are also compared with the HF-video camera images which are available for the case of the wave breaking over the flat seabed (Figure 3.9). The comparison between the numerical and experimental wave elevation is presented in Figure 3.10.

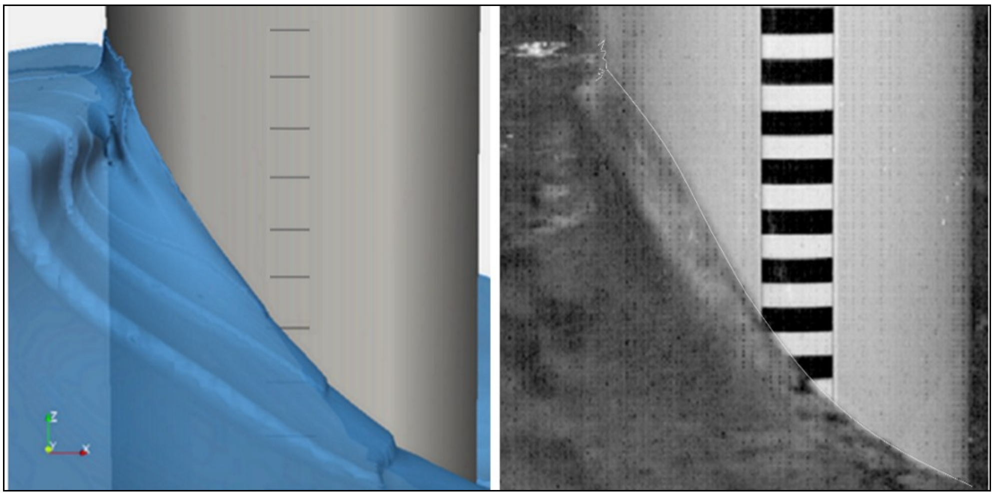

Figure 3.9 Snapshot of the breaking wave impact

Figure 3.11 shows that the computed forces are in reasonable agreement with experimental data. Small discrepancies are observed only for the peak value of the impact force in the case 2.

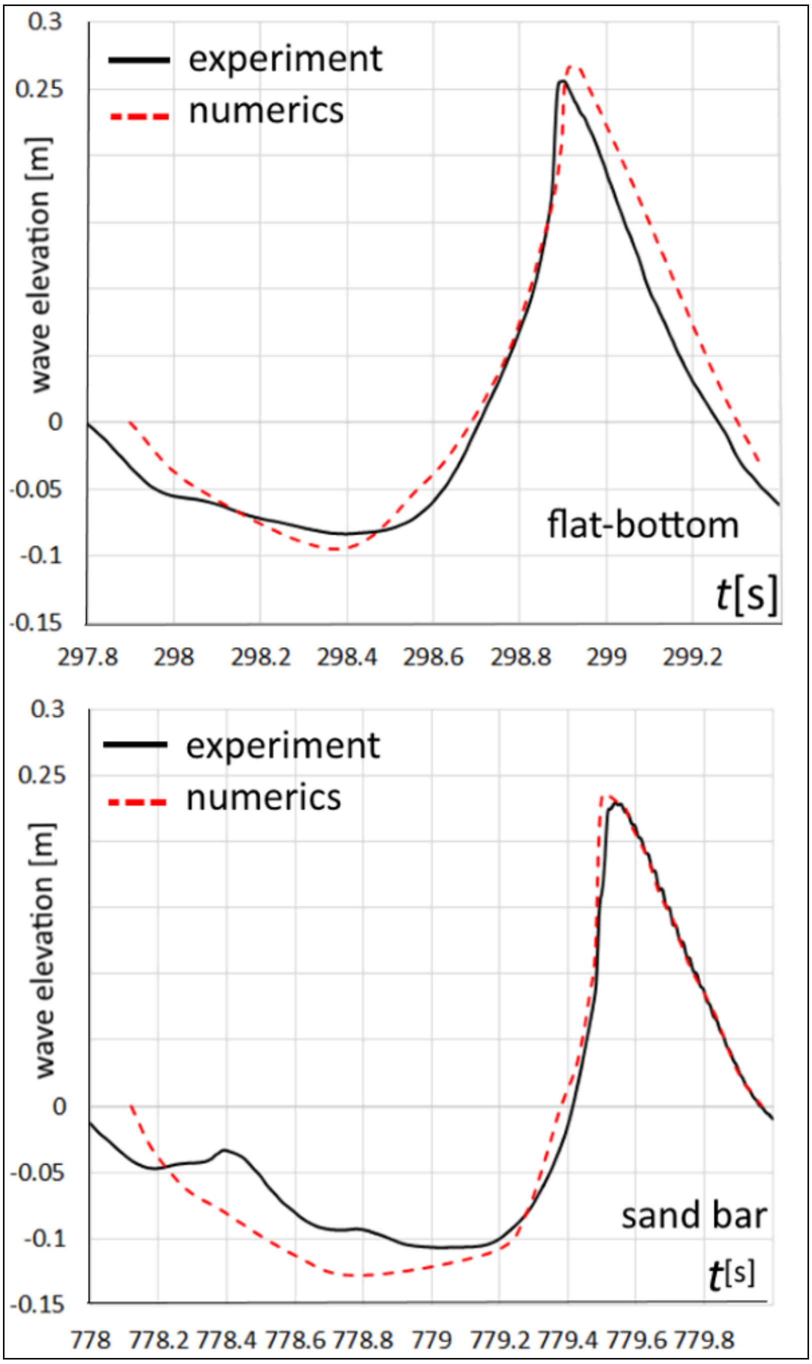

Figure 3.10 The comparison between wave elevations taken 3*D* aside the monopile CL

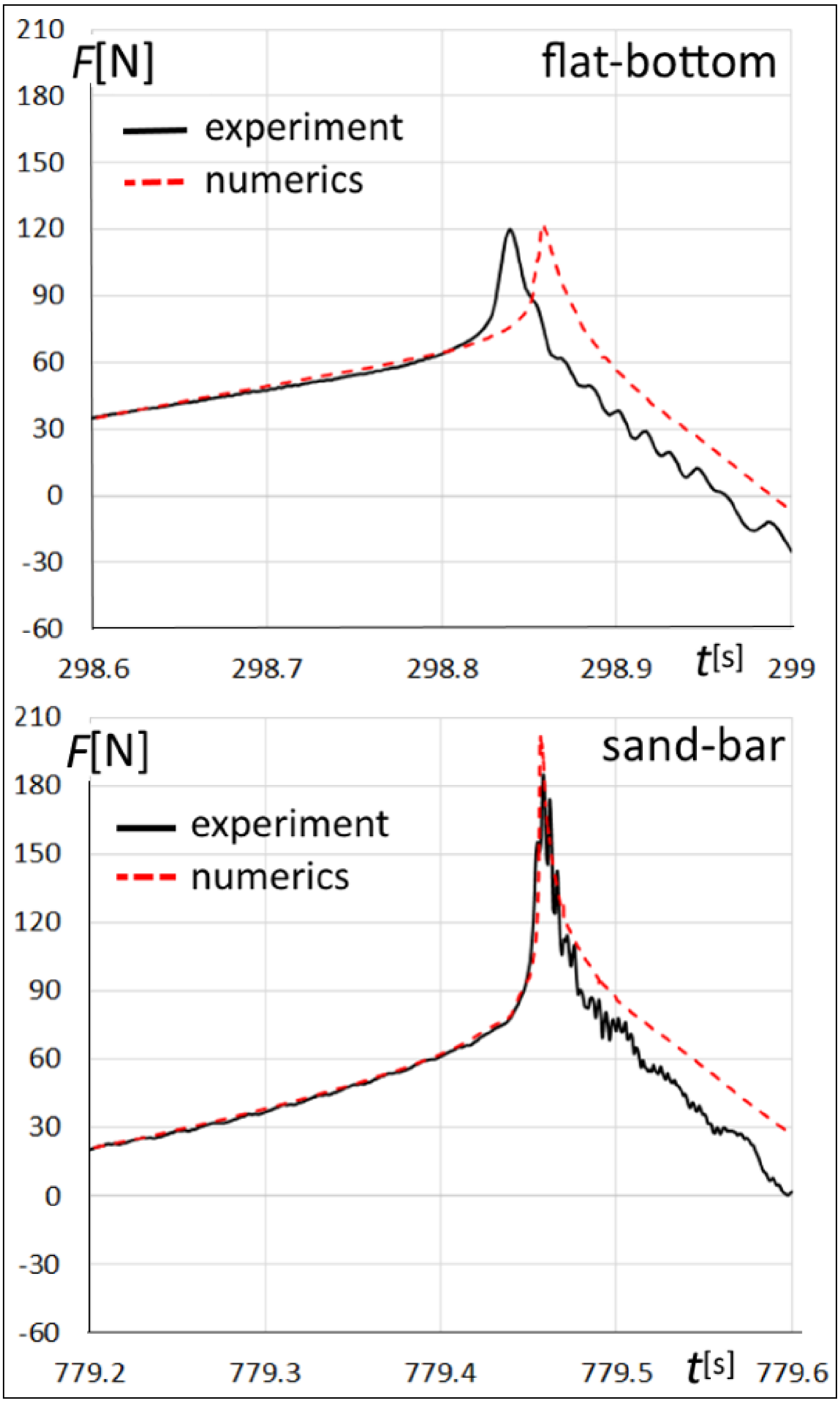

Figure 3.11 The comparison between hydrodynamic forces

The snapshot from the HF-video camera for the case 1 is very similar to the numerical visualization (Figure 3.9). The numerical simulation reveals that wave breaks just in the front of the structure and wave run-up damps the magnitude of impact force. Figure 3.12 presents the magnitude of the computed impact force on the structure shifted 1.25R upstream. The computed impact force in this case is 4 times higher. This shows that the results based on the simulation of the realistic sea state conditions may lead to significantly lower magnitude of the impact force. The prediction of the probability of occurrence of the most violent breaking wave stage may be important in optimizing structure geometry.

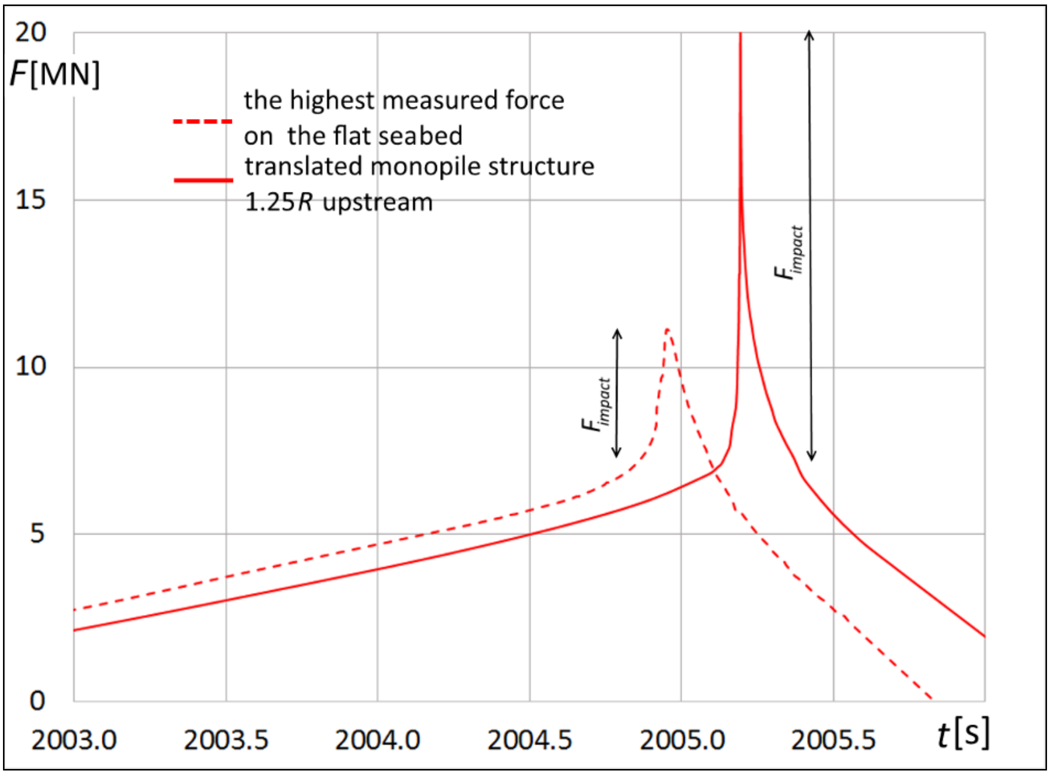

Figure 3.12 Computed impact force for the translated monopile structure (flat seabed)

Figure 3.13 and Figure 3.14 show the comparison between the computed and measured impact pressures at the front line of the monopile structure. In the case 1, the numerical results are in a good agreement with the laboratory measurements. In the case 2, the numerical results are also in a good agreement with the laboratory measurements. The discrepancies between the numerical and experimental results for case 2 occur basically only in the peak pressure zone. The observed discrepancies arise mainly from relatively low sampling rate of pressure measurements (1kHz) which is not sufficient to accurately record the pressure evolution in a rising phase.

Nevertheless, at the moment of the maximum impact force, which occurs after the moment of the peak pressure at the front line of the monopile, the values of computed and measured pressures are similar. The results from this section show that the presented numerical model can reproduce experimental results with sufficient accuracy.

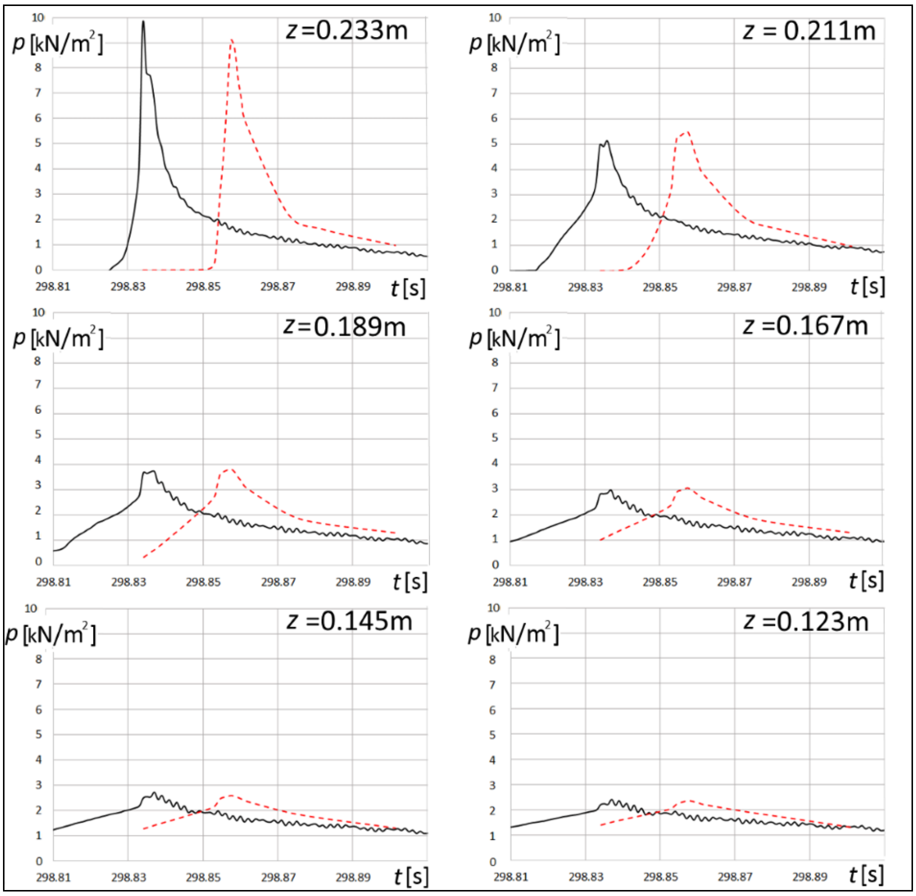

Figure 3.13 Comparison of the impact pressures at the front line of the monopile, case 1

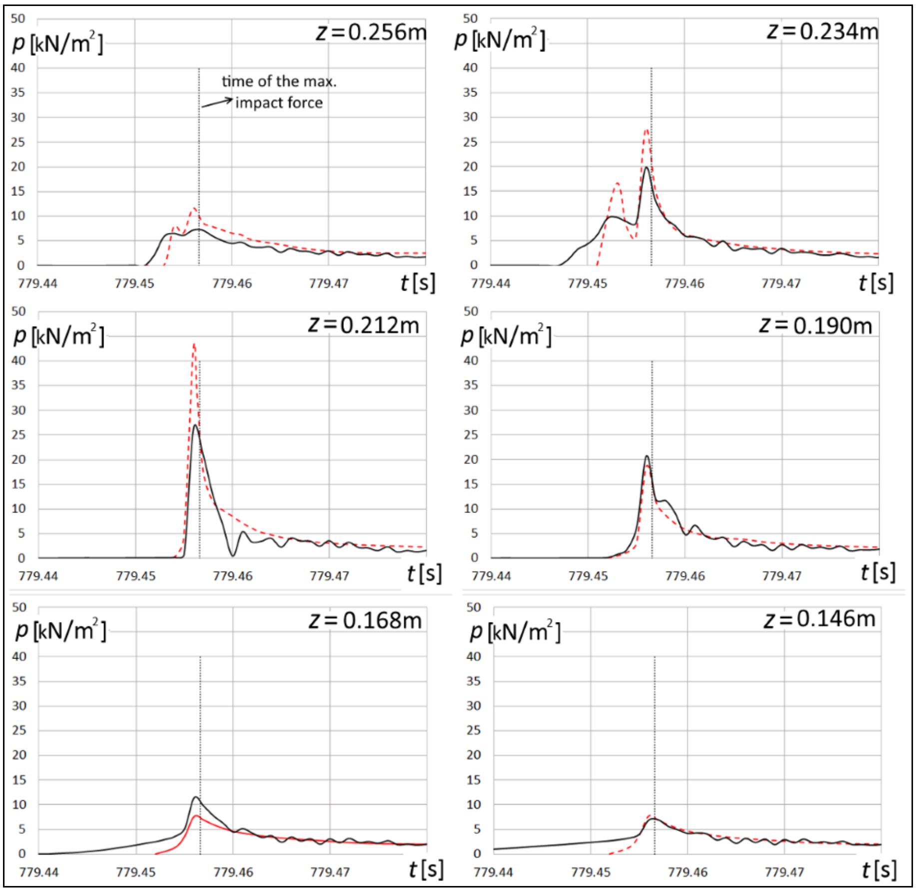

Figure 3.14 Comparison of the impact pressures at the front line of the monopile, case 2

3.3 Experimental observations

The breaking wave loads exerted on a monopile structure depend on the wave celerity, the position of wave breaking with respect to the structure location and, as presented in section 2.5, the shape of the breaking wave profile. Different stages of the wave breaking with respect to the structure position can be evaluated by the analyses of pressure measurements at the front line of the structure. Figure 3.15 shows an example of the pressure measurements at different vertical locations on the structure. The beginning of the breaking wave interaction with the structure is defined by $t_{p(initial)}$. It corresponds to the moment when the pressure exceeds $p>0.5\rho c_b^2$. The moment of the maximum measured impact pressure is defined by

$t_{p(max)}$. This moment is characterized by a sudden increase of pressure at all pressure sensors.

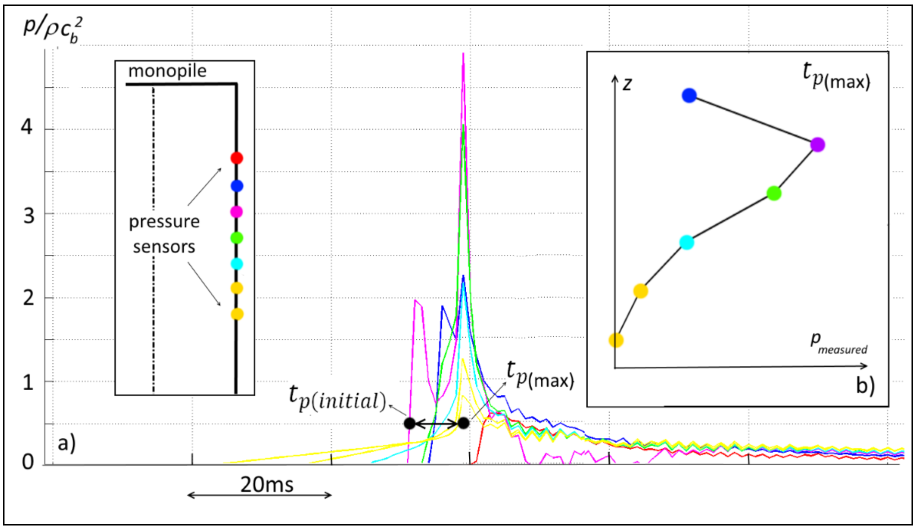

Figure 3.15 Measured impact pressure at the different vertical locations

Figure 3.16 shows two scenarios of the breaking wave impact on the structure. Considering the breaking wave scenario a), the beginning of the breaking wave interaction with the structure occurs at the vertical location of the blue pressure transducer, while the peak impact pressure occurs at the vertical location of the red pressure sensor. These results indicate that wave breaks just prior to the structure, and that impact of the overturning wave jet is significantly influenced by the presence of the wave run-up, as it is sketched in Figure 3.16a.

Considering the breaking wave scenario b), the beginning of the breaking wave interaction with the structure starts at the vertical location of the magenta pressure transducer, while the peak impact pressure occurs at the vertical location between magenta and the green pressure transducers. These results indicate that wave breaks before the structure, and the overturning wave jet hits the structure and this process is not blocked by the wave run-up, as it is sketched in Figure 3.16b. The time lag $dt = t_{p(max)} - t_{p(initial)}$ is longer in the scenario b.

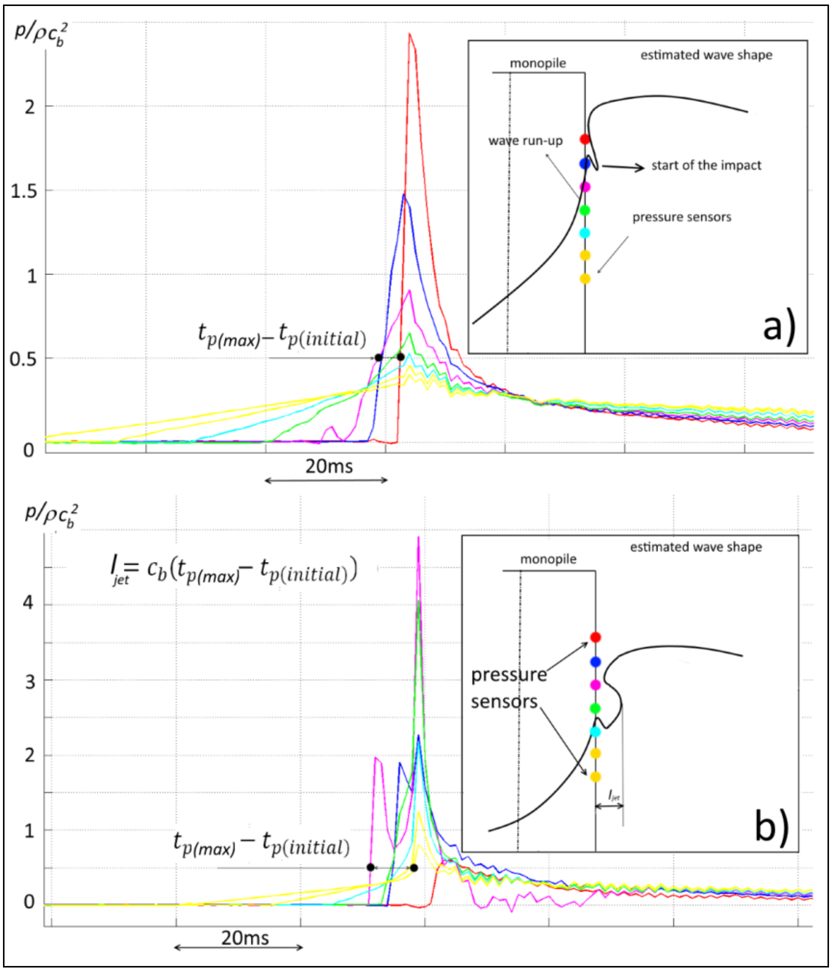

Figure 3.16 Estimation of the wave shape considering the pressure signal characteristic

The horizontal length of the overturning wave jet can be approximated as

$$l_{jet} = c_b (t_{p(\max)} - t_{p(initial)}) \tag{2.38}$$

Considering the differences in the approximated length of the overturning wave jet, wave impact scenarios may be grouped in different classes. The results of presented measurements are grouped in 4 classes: l_{jet}.<0.2R, 0.2R < l_{jet}.<0.5R, 0.5R <l_{jet}<1R and l_{jet} >1R. An example of the measured force corresponding to each of the aforementioned classes is presented in Figure 3.17 to Figure 3.20. Each figure presents the approximation of the wave shape profile prior to the impact on the structure. The measured wave elevations are compared to a theoretical profile arising from the application of a stream function model. The measured inline forces are compared to the results obtained by applying the Morison's equation and the stream function wave theory. The wave phase speed applied in this section is c_b=1.2$c_{b,stream}$ (DNV, 2010). By increasing the steepness of the wave crest front, the accuracy of the Morison's equation decreases. A similar conclusion is derived from numerical results in section 2.5.1.

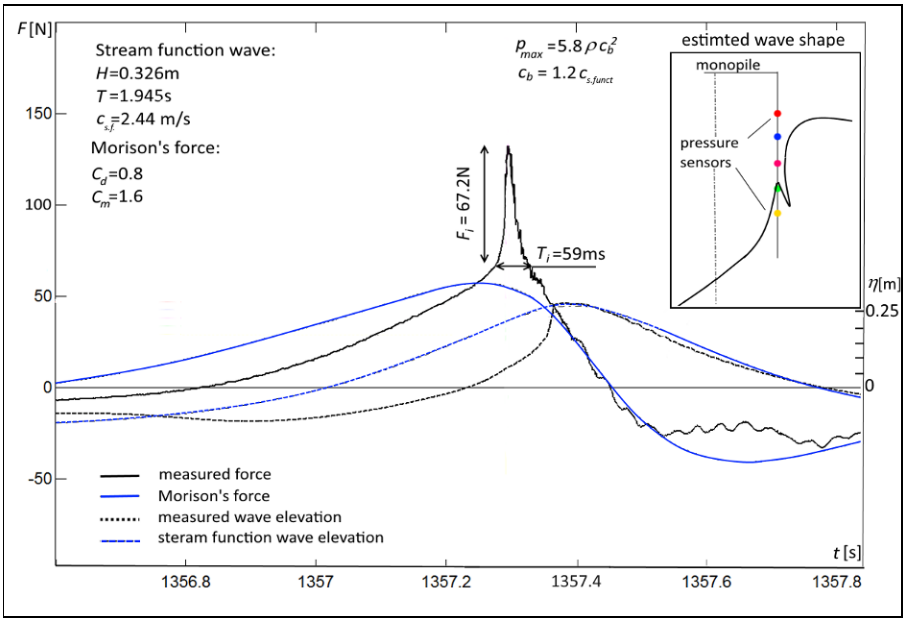

Figure 3.17 Experimental measurements, $l_{jet.}$<0.2R

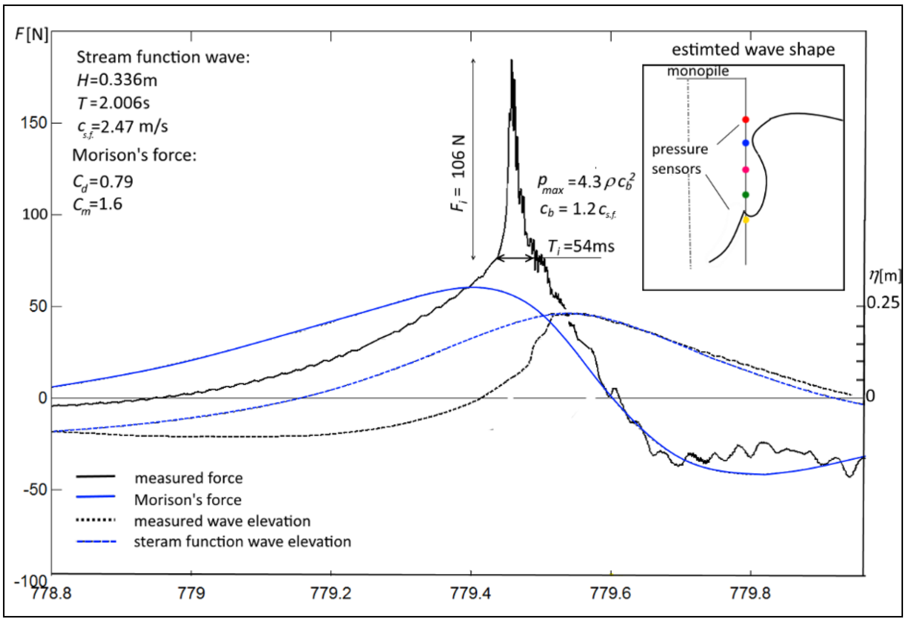

Figure 3.18 Experimental measurements, $0.2R < l_{jet}<0.5R$

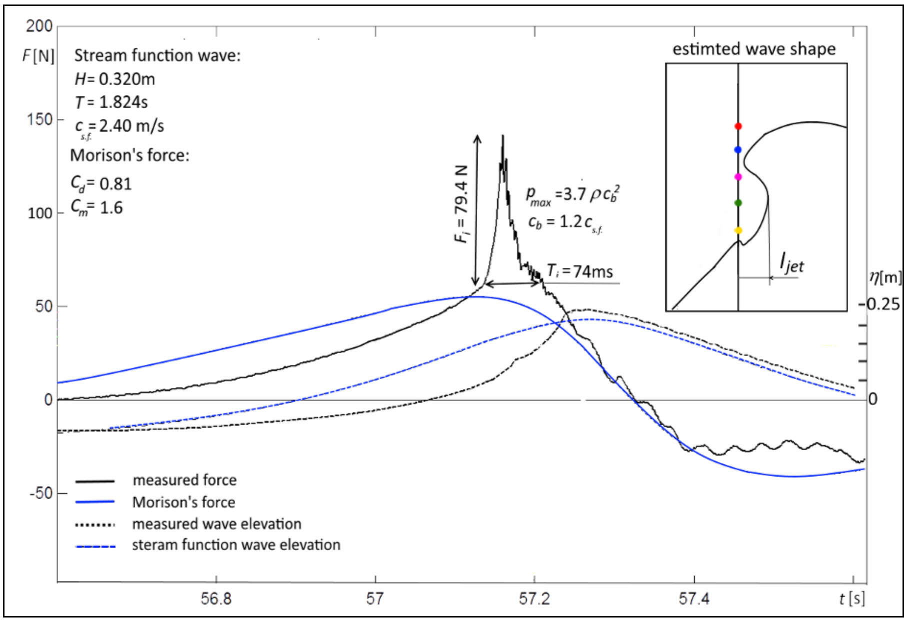

Figure 3.19 Experimental measurements, $0.5R <l_{jet}<1R$

The measured hydrodynamic forces higher than $F_{measured}$ >100N are selected for the discussion of results. Figure 3.21 presents a normalized impact force $F_{in}=F_i/\rho R c_b^2\eta_b$ as a function of the normalized length of the overturning wave jet l_{jet}/R. The highest loading is observed for $0.2R<l_{jet}<0.5R$. In such cases waves break slightly before the structure. Such situations are usually recognized as the most violent breaking wave scenario. These results justify cases selected in numerical analysis.

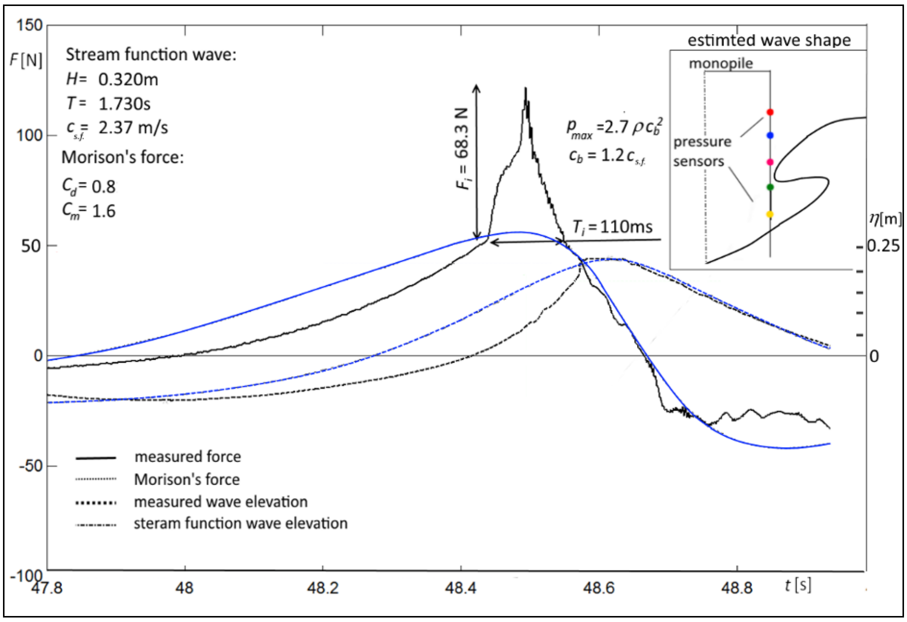

Figure 3.20 Experimental measurements, $l_{jet} > 1R$

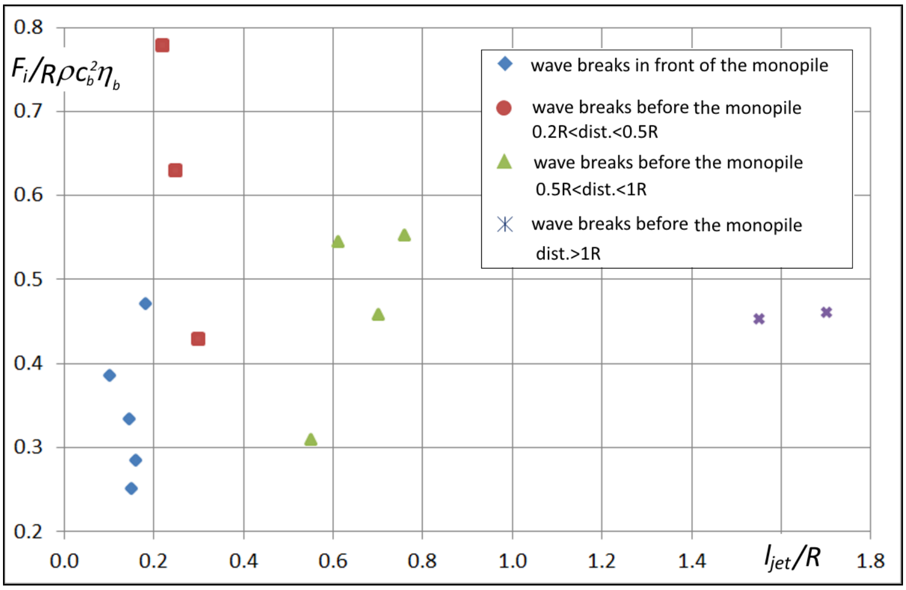

Figure 3.21 The impact force as a function of the breaking wave stage

Differences between the profiles of the irregular breaking waves can be analysed considering the approximation of the wave crest front steepness parameter

$$s_f = \frac{\eta_b}{c_b(t_{(\eta=\eta_b)} - t_{(\eta=0)})} \tag{2.39}$$

The range of the crest front steepness parameter obtained from experimental analysis is s_f = 0.35-0.55. According to the classification of Bonmarin (1989), in the laboratory experiments conducted for irregular waves, wave breaking ranges from spilling up to weakly plunging. Figure 3.22 shows the measured impact forces as a function of the wave crest front steepness parameter. Considering the different classes of the breaking wave scenarios, the general tendency is that breaking waves with the higher steepness induce higher impact loading.

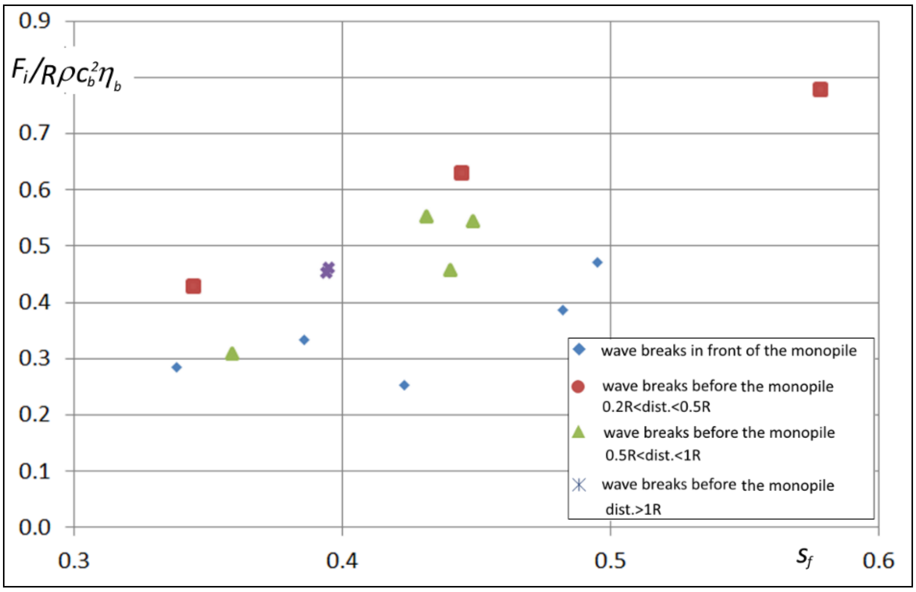

Figure 3.22 The impact force as a function of the wave crest front steepness

3.4 Summary

Conducted experiments simulate hydrodynamic loads exerted on the monopile support structure during the storm conditions. The laboratory experiments were conducted for a structure installed on a flat seabed and on a sand bar bottom. Approximately 75 cases of wave slamming events on the structure are detected, among which 60 slamming events corresponds to the wave propagation over the sand bar.

The laboratory measurements revealed that the highest measured impact force due to wave breaking over the flat seabed is approximately 35% lower than the highest measured impact force due to wave breaking over the sand-bar. The main reason is that the former breaking wave case is considerably influenced by the wave run-up damping effects.

The temporal and spatial characteristics of impact pressures measured at the front line of the structure are used to evaluate different stages of wave breaking impact process. The highest induced impact forces arise from wave breaking slightly before the structure. The impact loads on the structure arise from wave breaking with location of breaking further from the structure and are lower in magnitude and longer in duration. Breaking waves characterized with higher steepness of the wave front have tendency to induce higher normalized impact force on the structure, $F_{in}=F_i/\rho R c_b^2 \eta_b$.

Calculation of the breaking wave impact force on cylindrical structures in engineering practice is based on approximation of the rectangular impact load distribution, usually defined by parameters $\lambda\approx 0.4$ and $C_{sr,max}=2\pi$. The parameters of the rectangular load distribution, that define the maximum measured impact force from conducted experiments, are significantly lower, $\lambda\approx 0.2$ and $C_{sr}=1.2\pi$.

Measurements conducted in laboratory experiments are applied for the verification of the numerical model in chapter 2.

4 Conclusion

Estimation of the breaking wave loading on cylindrical structures in engineering practice is based on evaluation of the non-impact and impact part of the total force. The non-impact force is generally calculated by applying the Morison's equation based on the stream function wave kinematics. The impact force is generally estimated assuming the rectangular load distribution along the area of the impact. The parameters of the rectangular load distribution are usually defined with the curling factor $\lambda \approx 0.4$ and the slamming coefficient C_{sr}=3-2π. The value of the slamming coefficient C_s=2π is based on the solution of the theoretical model which solves the impact of infinitely long cylinder on the calm water with a constant speed. The curling factor estimations are obtained semi-empirically as a function of the measured impact force and the theoretical value of the slamming coefficient.

The magnitude of the impact force in experimental measurements is not easy to determine, as measurements are affected by the vibration of a structure. Application of a filtering procedure removes the effect of the structural vibrations, however, the filtering procedure also affects the oscillatory behaviour of the impact force which could be correlated with the compressibility effects of air pockets. The effect of air compressibility is usually neglected in the analysis of the breaking wave loads on cylindrical structures. The general explanation is that air pocket generated between the overturning wave jet and the cylindrical structure has open lateral boundaries, which allows a free air flow.

This study includes experimental and numerical analysis of a breaking wave interaction with a monopile structure. Conducted experiments include simulation of a 50-year storm condition where more than 10000 irregular waves are generated. The maximum measured force obtained in an analysis conducted for a flat sea-bed condition does not correspond to the most violent breaking wave stage. The results of the numerical model for the identical breaking wave event, but with the monopile translated 1.25R upstream, provide 4 times higher magnitude of the impact force. This shows a need to develop a statistical procedure to include the probability of occurrence of the most violent breaking wave stage in a breaking wave load analysis.

The maximum measured force obtained for sand-bar cases corresponds to the most violent breaking wave stage. The impact part of a total force for these cases calculated on the bases of a simplified approach with a rectangular load distribution and $\lambda\approx0.4$, $C_{sr}=2\pi$, is more than 3 times higher than the measured impact force.

The goal of the study is to investigate the effects of the breaking wave shape on the impact loads on a monopile structure. The results of the study are obtained by employing the numerical model which is based on the solution of the Navier-Stokes equations and VOF technique. The computational grid sensitivity analysis shows that characteristics of the impact force strongly depend on the thickness of the air-water interface. In order to reach a converged solution, the computational grid resolution in the zone of the wave impact must be very fine. The results of the applied incompressible numerical model agree very well with the results of the conducted experimental measurements.

The non-impact part of the computed breaking wave force is compared with the solution of the Morison's equation that is based on the stream function wave kinematics. For cases when steepness of the breaking wave front is low, the application of the Morison's equation results in a relatively good approximation of the non-impact force. As the steepness of the breaking wave front increases, the Morison's equations is not adequate for the calculation of wave loads.

The numerical results show that the highest impact pressure occurs in the region below the overturning wave crest, where the overturning wave crest meets the wave run-up on the structure. The analysis shows that at this location the breaking wave impact is maximum and the slamming coefficient is about $Cs=2\pi$. Away from the peak region, wave impact loads decay rapidly. The area of the impact load on the structure is significantly higher than the impact area defined and applied in engineering practice. The area under the computed impact load distribution can be represented by an equivalent rectangular area. Considering the geometrically defined curling factor, corresponding values of the slamming coefficients are scattered in the range $C_{sr} = \pi$ - 2π. The results show that the value of the slamming coefficient is inversely proportional to the steepness of the breaking wave front. Therefore, the approximation of the vertical load distribution by a rectangular is a simplification which cannot uniquely approximate real load distribution arising from breaking wave attack on a monopile structure.

The derived numerical results encourage us to propose an alternative method for the calculation of impact forces which can be further developed and eventually used for a preliminary analysis. The investigations show that the non-impact wave loads may be derived from the Morison equation based on the kinematics obtained directly from the NS/VOF solution, while the breaking wave impact forces may be assessed by applying the proposed diagram of the temporal vertical load distribution, Cs(t,z).

The effect of the air compressibility is investigated for the model and prototype conditions. The impact loads for model conditions are characterized by strong oscillations in a decay stage, while for prototype conditions, the oscillations of the impact forces in a decay stage are of secondary importance. The impact loads in rising phase are almost identical for the model and prototype conditions. This applies to both, the incompressible and compressible case. The peak impact force obtained by applying the compressible model is higher than the peak impact force obtained by applying the incompressible model for both the model and prototype conditions.

5 Appendix

5.1 Appendix I

- **Additional code lines in the top level solver WaveFOAM**

  - In createFields.H add additional code lines:

```
volVectorField acceleration
 (
     IOobject
       (
         "acceleration",
          runTime.timeName(),
           mesh,
          IOobject::NO_READ,
          IOobject::AUTO_WRITE
         ),
      fvc::DDt(phi, U)
   );

   dimensionedVector k("one", dimless, vector(0, 0, 1);
   volScalarField gradUz

 (
     IOobject
         (
           "gradUz",
           runTime.timeName(),
           mesh,
           IOobject::NO_READ,
           IOobject::AUTO_WRITE
          ),
     fvc::grad(U & k) & k
 );
```

  - In interFoam.C before the end of the time loop add:

```
acceleration = fvc::DDt(phi, U)
gradUz = (fvc::grad(U & k) & k)
```

5.2 Appendix II

- **Results from experimental measurements found in the literature**

Table 1 Comparison of experimental procedures found in the literature

Author	basin dimension	bottom	generated wave	meaasured	post-process	D	d	η_b	c_b
	length/width/depth	/	/	/	/	[m]	[m]	[m]	[m/s]
Zhou et al. (1991)	30 x 0.76 x 0.9	flat	wave packet	pressure points	/	0.17	0.6	0.175	1.7
Chan et al. (1995)	30 x 3 x 2	flat	wave packet	pressure points	/	0.2	0.8	0.185	1.932
Wienke et al. (2001)	309 x 5 x 7	flat	wave packet	global force, pressure points	convolution	0.7	4.25	1.9	6
Hildebrandt & Schlurmann et al. (2001)	330 x 5 x 7	slope (1/20)	wave packet	pressure points	/	0.5	2.5	0.97	4.8
Goda et al. (1966)	/	slope (1/10)	regular	strip force	/	0.0736	0.15	0.155	1.81
Arnsten et al. (2011)	33 x 1 x 1	slope (1/3.7)	regular	strip forces	Duhamel integral	0.06	0.35	0.25	2.3
Tanimoto et al. (1986)	105 x 3 x 2.05	slope (1/30)	regular* / irregualar	strip forces	low pas filter	0.14	0.7	0.49*	3.2*

Table 2 Comparison of experimental results found in the literature

Author	meaasured	$p_{max}/\rho c_b^2$	press. sampling rate [kHz]	$t_{pi}*C_b/R$	$C_{s,max}$	C_s - vertical distribution	λ
Zhou et al. (1991)	pressure points	3-21	20	<0.02	/	/	/
Chan et al. (1995)	pressure points	16-48	20	<0.02	/	/	/
Wienke et al. (2001)	pressure points	40	12	<0.02	/	/	/
Hildebrandt & Schlurmann et al. (2011)	pressure points	1-4	10	<0.10	/	/	/
Goda et al. (1966)	global force	/	/	/	π (theoreticall)	rectangular (theoreticall)	0.4 (calculated)
Wienke et al. (2001)	global force	/	/	/	2π (theoreticall)	rectangular (theoreticall)	0.4-0.6 (calculated)
Arnsten et al. (2011)	strip forces	/	/	/	1.37 (measured)	≈ traingular (measured)	0.35 (calculated)
Tanimoto et al. (1986)	strip forces	/	/	/	1.1 (measured)	≈ traingular (measured)	0.7 (calculated)

References

Abrahamsen, B. C., & Faltinsen, O. M. (2011). The effect of air leakage and heat exchange on the decay of entrapped air pocket slamming oscillations. *Physics of Fluids*, *23*(10). https://doi.org/10.1063/1.3638612

Alagan Chella, M., Bihs, H., Myrhaug, D., & Muskulus, M. (2015). Breaking characteristics and geometric properties of spilling breakers over slopes. *Coastal Engineering*, *95*, 4–19. https://doi.org/10.1016/j.coastaleng.2014.09.003

Arntsen, Ø. A., X. Ros Collados, and A. T. (2011). Impact forces on a vertical pile from plunging breaking waves, 1–59.

Banner, M. L., & Phillips, O. M. (1974). On the incipient breaking of small scale waves. *Journal of Fluid Mechanics*, *65*(4), 647. https://doi.org /10.1017/S0022112074001583

Battjes, J. a. (1974). *Surf Similarity*. *Coastal Engineering*. https://doi.org/10.1016/0378-3839(79)90016-4

Battjes, J. A. (1988). Surf-zone dynamics. *Nnual Review of Fluid Mechanics*, *20.1*, 257–291.

Berberović, E., Van Hinsberg, N. P., Jakirlić, S., Roisman, I. V., & Tropea, C. (2009). Drop impact onto a liquid layer of finite thickness: Dynamics of the cavity evolution. *Physical Review E - Statistical, Nonlinear, and Soft Matter Physics*, *79*(3). https://doi.org/10.1103/PhysRevE.79.036306

Bonmarin, P. (1989). Geometric properties of deep-water breaking waves. *Journal of Fluid Mechanics*, *209*(1), 405. https://doi.org/10.1017/S0022112089003162

Bredmose, H., Bullock, G. N., & Hogg, A. J. (2015). Violent breaking wave impacts. Part3. Effects of scale and aeration. *Journal of Fluid Mechanics*, *765*, 82–113. https://doi.org/DOI 10.1017/jfm.2014.692

Bredmose, H., Bullock, G. N., & Hogg, A. J. (2015). Violent breaking wave impacts. Part 3. Effects of scale and aeration. *Journal of Fluid Mechanics*, *765*, 82–113. https://doi.org/10.1017/jfm.2014.692

Bredmose, H., & Jacobsen, N. G. (2010). Breaking Wave Impacts on Offshore Wind Turbine Foundations: Focused Wave Groups and CFD. *29th International*

Conference on Ocean, Offshore and Arctic Engineering: Volume 3, 397–404. https://doi.org/10.1115/OMAE2010-20368

Bredmose, H., & Jacobsen, N. G. (2011). Vertical wave impacts on offshore wind turbine inspection platforms. In *Proceedings of the ASME 2011 30th International Conference on Ocean, Offshore and Arctic Engineering OMAE2011 June 19–24, 2011, Rotterdam, The Netherlands* (Vol. 436, pp. 13–32). https://doi.org/10.1098/rspa.1995.0091

Bredmose, H., Peregrine, D. H., & Bullock, G. N. (2009). Violent breaking wave impacts. Part 2: Modelling the effect of air. *Journal of Fluid Mechanics*, *641*, 389–430. https://doi.org/10.1017/S0022112009991571

Bullock, G. N., Crawford, A. R., Hewson, P. J., Walkden, M. J. A., & Bird, P. A. D. (2001). The influence of air and scale on wave impact pressures. *Coastal Engineering*, *42*(4), 291–312. https://doi.org/10.1016/S0378-3839(00)00065-X

Bullock, G. N., Obhrai, C., Peregrine, D. H., & Bredmose, H. (2007). Violent breaking wave impacts. Part 1: Results from large-scale regular wave tests on vertical and sloping walls. *Coastal Engineering*, *54*(8), 602–617. https://doi.org/10.1016/j.coastaleng.2006.12.002

Chan, E. S., Cheong, H. F., & Tan, B. C. (1995). Laboratory study of plunging wave impacts on vertical cylinders. *Coastal Engineering*, *25*(1–2), 87–107. https://doi.org/10.1016/0378-3839(94)00042-V

Chan, E. S., & Melville, W. K. (1988). Erratum: Deep-Water Plunging Wave Pressures on a Vertical Plane Wall. *Proceedings of the Royal Society A: Mathematical, Physical and Engineering Sciences*, *419*(1857), 380–380. https://doi.org/10.1098/rspa.1988.0114

Choi, S. J., Lee, K. H., & Gudmestad, O. T. (2015). The effect of dynamic amplification due to a structure's vibration on breaking wave impact. *Ocean Engineering*, *96*, 8–20. https://doi.org/10.1016/j.oceaneng.2014.11.012

DNV. (2010). Environmental conditions and environmental loads. *Dnv*, (October), 9–123. https://doi.org/10.1109/INTLEC.1993.388591

DNV. (2014). DNV-OS-J101 Design of Offshore Wind Turbine Structures. *May*, (May), 212–214.

Engsig-Karup, A. P., Bingham, H. B., & Lindberg, O. (2009). An efficient flexibleorder model for 3D nonlinear water waves. *Journal of Computational Physics*, *228*(6), 2100–2118. https://doi.org/10.1016/j.jcp.2008.11.028

Faltinsen, O. M., Newman, J. N., & Vinje, T. (1995). Nonlinear wave loads on a slender vertical cylinder. *Journal of Fluid Mechanics*, *289*(1), 179. https://doi.org/10.1017/S0022112095001297

Ghadirian, A., Bredmose, H., & Dixen, M. (2016). Breaking phase focused wave group loads on offshore wind turbine monopiles. *Journal of Physics: Conference Series*, *753*, 92004. https://doi.org/10.1088/1742-6596/753/9/092004

Hildebrandt, A., & Schlurmann, T. (2012). Breaking wave kinematics, local pressures, and forces on a tripod support structures. *Coastal Engineering*, 1–14. https://doi.org/10.9753/icce.v33.structures.71

Hirt, C. W., & Nichols, B. D. (1981). Volume of fluid (VOF) method for the dynamics of free boundaries. *Journal of Computational Physics*, *39*(1), 201–225. https://doi.org/10.1016/0021-9991(81)90145-5

International Eletrotechnical Commision. (2005). IEC 61400-1 Wind Turbines - Part 1: Design requirements. *Wind Turbines – Part 1: Design Requirements*, *2005*, 1–92. https://doi.org/10.1055/s-2007-985912

Irschik, K. A. I. (2002). Breaking wave characteristics for the loading of a slender pile -, 1–12.

Jacobsen, N. G., Fuhrman, D. R., & Fredsøe, J. (2012). A wave generation toolbox for the open-source CFD library: OpenFoam®. *International Journal for Numerical Methods in Fluids*, *70*(9), 1073–1088. https://doi.org/10.1002/fld.2726

Kamath, A., Alagan Chella, M., Bihs, H., & Arntsen, ?ivind A. (2016). Breaking wave interaction with a vertical cylinder and the effect of breaker location. *Ocean Engineering*, *128*(September), 105–115. https://doi.org/10.1016/j.oceaneng.2016.10.025

Kjeldsen, S. P., & Myrhaug, D. (1979). Breaking Waves in Deep Water and Resulting Wave Forces. *11Th Offshore Technology Conference*, 2515–2522.

Malenica, S., Molin, B. (1995). Third-Harmonic Wave Diffraction by a Vertical Cylinder. *Journal of Fluid Mechanics*, *302*, 203–229.

https://doi.org/10.1017/S0022112095004071

Mo, W., Jensen, A., & Liu, P. L. F. (2013). Plunging solitary wave and its interaction with a slender cylinder on a sloping beach. *Ocean Engineering*, *74*, 48–60. https://doi.org/10.1016/j.oceaneng.2013.09.011

Morison, J. R., Johnson, J. W., & Schaaf, S. a. (1950). The Force Exerted by Surface Waves on Piles. *Journal of Petroleum Technology*, *2*(5), 149–154. https://doi.org/10.2118/950149-G

Newman, J. N., & Landweber, L. (1978). Marine Hydrodynamics. *Journal of Applied Mechanics*. https://doi.org/10.1115/1.3424341

Paulsen, B. T. (2013a). Forcing of a Bottom-Mounted Circular Cylinder by Steep Regular Water Waves at Finite Depth, *Journal of Fluid Mechanics, vol 755, pp 1-34*

Paulsen, B. T. (2013b). *PhD Thesis - Efficient computations of wave loads on offshore structures*.

Paulsen, B. T., Bredmose, H., & Bingham, H. B. (2014). An efficient domain decomposition strategy for wave loads on surface piercing circular cylinders. *Coastal Engineering*, *86*, 57–76. https://doi.org/10.1016/j.coastaleng.2014.01.006

Peregrine, D. H. (2003). Water-Wave Impact On Walls. *Annual Review of Fluid Mechanics*, *35*(1), 23–43. https://doi.org/10.1146/annurev.fluid.35.101101.161153

Peregrine, D. H., Bredmose, H., Bullock, G., Obrhai, C., M?ller, G., & Wolters, G. (2005). Water wave impact on walls and the role of air. In *Proceedings of the Coastal Engineering Conference* (Vol. 2005–Janua). https://doi.org/10.1142/9789812701916-0323

Peregrine, H., Bredmose, H., Bullock, G., Obhrai, C., Müller, G., & Wolters, G. (2008). Violent water wave impact on a wall. *Rogue Waves*, 155–159.

Perlin, M., Choi, W., & Tian, Z. (2013). Breaking Waves in Deep and Intermediate Waters. *Annual Review of Fluid Mechanics*, *45*(1), 115–145. https://doi.org/10.1146/annurev-fluid-011212-140721

Rainey, R. C. T. (1989). A new equation for calculating wave loads on offshore structures. *Journal of Fluid Mechanics*, *204*(WW3), 295–324.

https://doi.org/10.1017/S002211208900176X

Scott, J. C. (1975). The role of salt in whitecap persistence. *Deep-Sea Research and Oceanographic Abstracts*, *22*(10). https://doi.org/10.1016/0011-7471(75)90002-9

Sulisz, W. (1998). Diffraction of nonlinear waves by founded horizontal rectangular cylinder. *Journal of Waterway, Port, Coastal, and Ocean Engineering,* ASCE, 124, 5, 257-263

Sulisz, W., Wilde, P., and Wiśniewski, M. (2005). Wave impact on elastically supported horizontal deck. *Journal of Fluids and Structures*, 21,3, 305-319.

Sulisz W., Paszake L. (2007). Extreme wave impact on a horizontal deck. *Proc of International Conference on Violent Flows.*

Sulisz, W., Paprota, M. (2008). Vibration of a horizontal deck due to extreme wave impact. *Proc of Chinese-German Joint Symposium on Coastal and Ocean Engineering.*

Sulisz W., Paprota, M. (2009). Vibrations of a horizontal deck due to freak wave attack. *Proc of 4th International Short Conference on Applied Coastal Research. Nuova.*

Sulisz, W. (2013). Reflection and transmission of nonlinear water waves at a semi-submerged dock. Archives of Mechanics, 65, 3, 237–260.

Sumer, M. B., & Fredsøe, J. (2006). *Hydrodynamics around cylindrical structures*.

Tanimoto, K., Takahashi, S., Kaneko, T., & Shiota, K. (1986). Impulsive Breaking Wave Forces on an Inclined Pile Exerted by Random Waves. *20th Conference of Coastal Engineering, Taipei, Taiwan*, *20*, 2288–2302. https://doi.org/10.9753/icce.v20.

Ting, F. C. K., & Kirby, J. T. (1996). Dynamics of surf-zone turbulence in a spilling breaker. *Coastal Engineering*, *27*(3–4), 131–160. https://doi.org/10.1016/0378-3839(95)00037-2

van Nuffel, D., Vepa, K. S., Baere, I., Degrieck, J., Derouck, J., & Paepegem, W. (2011). Parameters affecting the pressure measurement on the surface of a rigid cylindrical body during water slamming impact. *30th International Conference on Ocean, Offshore and Arctic Engineering*, (c), 1–10.

Veic, D., Sulisz, W. (2018). Impact Pressure Distribution on a Monopile Structure Excited by Irregular Breaking Wave. *Polish Maritime Research*, *25*, 29-35

Veic, D., Sulisz, W., Soman, R. (2019). Effect Of Breaking Wave Shape On Impact Load On A Monopile Structure. *Brodogradnja Journal (in press)*

von Karman, T. (1929). The impact on seaplane floats during landing. *National Advisory Committee for Aeronautics Technical Notes*. https://doi.org/19930081174

Vukcevic, V. (2016). Numerical Modelling of Coupled Potential and Viscous Flow for Marine Applications. PhD Thesis. University of Zagreb, Faculty of Mechanical Engineering and Naval Architecture

Wagner, H. (1932). Über Stoß-und Gleitvorgänge an der Oberfläche von Flüssigkeiten. *Journal of Applied Mathematics and Mechanics*, *4*(12), 193–215.

Wienke. (2001). DRUCKSCHLAGBELASTUNG AUF SCHLANKE ZYLINDRISCHE BAUWERKE DURCH BRECHENDE WELLEN theoretische und großmaßstäbliche Laboruntersuchungen.

Wienke, J., & Oumeraci, H. (2005). Breaking wave impact force on a vertical and inclined slender pile - Theoretical and large-scale model investigations. *Coastal Engineering*, *52*(5), 435–462. https://doi.org/10.1016/j.coastaleng.2004.12.008

Wienke J., S. U. and O. H. (2001). Breaking Wave Impact on a Slender Cylinder Jan. *Coastal Engineering Journal*, 1787–1798.

Wood, D. J., Peregrine, D. H., & Bruce, T. (2000). Study of wave impact against a wall with pressure-impulse theory. *Journal of Waterway, Port, Coastal, and Ocean Engineering*, *126*(4), 182–190.

Xiao, H., & Huang, W. (2015). Three-Dimensional Numerical Modeling of Solitary Wave Breaking and Force on a Cylinder Pile in a Coastal Surf Zone. *Journal of Engineering Mechanics*, *141*(8), A4014001. https://doi.org/10.1061/(ASCE)EM.1943-7889.0000834

Zhou, D., Chan, E. S., & Melville, W. K. (1991). Wave impact pressures on vertical cylinders. *Applied Ocean Research*, *13*(5), 220–234. https://doi.org/10.1016/S0141-1187(05)80046-X